2009-01-23

Nanotechnology for Molecular Recognition of Biological Analytes

Robert C. Triulzi
University of Miami, robtriulzi@gmail.com

UNIVERSITY OF MIAMI

NANOTECHNOLOGY FOR MOLECULAR RECOGNITION OF BIOLOGICAL ANALYTES

By

Robert C. Triulzi

A DISSERTATION

Submitted to the Faculty
of the University of Miami
in partial fulfillment of the requirements for
the degree of Doctor of Philosophy

Coral Gables, Florida

June 2008

UNIVERSITY OF MIAMI

A dissertation submitted in partial fulfillment of
the requirements for the degree of
Doctor of Philosophy

NANOTECHNOLOGY FOR MOLECULAR RECOGNITION OF BIOLOGICAL ANALYTES

Robert C. Triulzi

Approved:

_____
Dr. Terri A. Scandura
Dean of the Graduate School

_____
Dr. R.M. Leblanc
Professor of Chemistry

_____
Dr. T.K. Harris
Professor of Chemistry

_____
Dr. F.M. Raymo
Professor of Chemistry

_____
Dr. J. Berry
Assistant Professor of Chemistry
Florida International University

TRIULZI, ROBERT, C. (Ph.D., Chemistry)

Nanotechnology for Molecular Recognition of Biological Analytes (June 2008)

Abstract of a dissertation at the University of Miami.

Dissertation supervised by Professor Roger M. Leblanc.
No. of pages in text. (118)

Nanotechnology is a term used to describe nanometer scaled systems. This thesis presents various nanomaterials and systems for the investigation of biologically relevant analytes in general, and in particular for their detection, decontamination, or destruction. The validation of short peptide fragments as models for protein aggregation is initially discussed through applying spectroscopic and microscopic techniques to Langmuir monolayer surface chemistry. Following this validation, the use of nanogold as a photoablative material for the destruction of aggregated protein is investigated. Subsequently, the versatility of nanotechnology is shown by investigating a different form of nanogold; namely, gold quantum dots and the interesting phenomenon that arise when dealing with materials on a nanoscale. Experiments involving a complex between these gold quantum dots and an antibody are performed for the detection of an immunoglobulin in solution. The power of this analytical technique is highlighted by the capability of detecting the analyte at nanomolar concentrations. Finally, a limitation—the multiple synthetic steps necessary for imparting biological activity-- of quantum dots is addressed: a single step reaction is studied that allows for direct stabilization and conjugation of quantum dots with proteins and enzymes. As a representative application of the above mentioned procedure, the detection and decontamination of an

organophosphorus compound is explored. In general, methods for overcoming limitations of nanoparticles and nanocrystals are discussed.

To my parents: Robert C. and Peggy S. Triulzi

ACKNOWLEDGEMENTS

I would like to acknowledge Dr. R. M. Leblanc for allowing me the privilege of working in his laboratory at the University of Miami. I wish to thank him for his guidance in research, teachings about the daily direction of a research laboratory, and his patience.

I would also like to express my appreciation to the members of my doctoral committee: Dr. T.K. Harris, Dr. F.M. Raymo, and Dr. G. Sui for their valuable insight. Additionally, I would like to thank all the professors in the department of chemistry at the University of Miami who were responsible for my chemical education.

I extend my sincere thanks and gratitude to Mr. Jhony Orbulescu for his teaching of the finer intricacies of research, his assistance in measurements, and his overall support.

I would like to thank my fellow graduate students and friends at the University of Miami who have made these past years a memorable experience.

Finally, I would like to thank my family who have been supportive of my efforts and who are responsible for encouraging my education, both academic and in life.

TABLE OF CONTENTS

LIST OF FIGURES

LIST OF TABLES

LIST OF ABBREVIATIONS

2D	Two dimensional
AD	Alzheimer's disease
AFM	Atomic force microscopy
ATR	Attenuated total reflectance
AuNP	Gold nanoparticle
AuQD	Gold quantum dot
Aβ	Beta-amyloid
Boc	tert-butoxycarbonyl
BSA	Bovine serum albumin
CCD	Charge coupled device
CD	Circular dichroism
DCC	Dicyclohexylcarbodiimide
DCM	Dichloromethane
DFP	Diisopropylfluorophosphate
DIC	Diisopropylcarbodiimide
DMF	Dimethylformamide
EG3	Triethyleneglycol
Fmoc	Fluorenylmethoxycarbonyl
FTIR	Fourier transform infrared
G2-OH	Second generation hydroxy terminated
HBTU	Benzotriazole tetramethyluronium hexafluorophosphate
H-NMR	Hydrogen nuclear magnetic resonance spectroscopy
HoBt	Hydroxybenzotriazole
HPLC	High performance liquid chromatography
HR-TEM	High resolution transmission electron microscopy
IETS	Inelastic electron tunneling spectroscopy
IgG	Immunoglobulin G
IVD	In vitro diagnostics
LB	Langmuir Blodgett
LC	Liquid condensed
LE	Liquid expanded
MeOH	Methanol
MS	Mass spectrometry
MW	Molecular weight
NIR	Near infrared
ODFL	5-octadecanoylamino fluorescein
OPAA	Organophosphorus acid anhydrolase
OPH	Organophosphorus hydrolase

PAMAM	Poly(amidoamine)
PBS	Phosphate buffered saline
PL	Photoluminescence
PM-IRRAS	Pulse modulated infrared reflection absorption spectroscopy
QD	Quantum dot
RP-HPLC	Reverse phase high performance liquid chromatography
SEM	Scanning electron microscopy
SPPS	Solid-phase peptide synthesis
SPR	Surface plasmon resonance
TEM	Transmission electron microscopy
TFA	Trifluoroacetic acid
UV-Vis	Ultraviolet visible
XPS	X-ray photoelectron spectroscopy

INTRODUCTION

Nanotechnology refers broadly to a field of applied science and technology whose unifying theme is the control of matter on the atomic and molecular scale. Strictly speaking, nanomaterials must have nanometer dimensions. This field encompasses a wide variety of research in all physical sciences including physics, biology, material science, and chemistry, and the application of such technologies typically draws on these four fields. While in previous decades the vast majority of research science being conducted dealt with micron scaled systems, it could be said that nanotechnology refers to the current state of scientific research; matter is capable of being controlled on the atomic and molecular level.

The applications of nanotechnology will lead to such advances as molecular and atomic computing, targeted and selected drug delivery, nanorobotics, and manipulation of biological systems at an astounding level, to name a few. Two main approaches exist when dealing with nanotechnology; the "bottom-up" and "top-down" approaches. Bottom-up approaches typically rely on self-assembling atomic or molecular systems that inherently form ordered structures under specific conditions. In the current state of research, the self-assembly process is currently under great scrutiny with a vast number of systems being discovered. It is the proper application and utilization of these systems and their interactions with others that will lead to new discoveries in the field and practical applications being formed. In the top-down approach, organization on a molecular or atomic level is created from a bulk component; that is, through the use of instrumentation, molecular organization or manipulation can be created with a particular

aim in mind. In this approach, the state of the field relies heavily on instrumentation and techniques being developed and their applications to novel systems.

One of the most intriguing findings in the field of nanotechnology are the unique physical phenomena that arise when dealing with materials on a nanolevel that are absent in the corresponding bulk materials. As a materials size decreases to the nanoscale, various limits are approached such that classical physics no longer provides a sufficient explanation of the observed phenomena; quantum mechanical explanations are needed to provide an accurate theoretical explanation of the empirical observations.

Two of the most studied materials, which have lead to an entire field of chemistry, are nanoparticles and nanocrystals. A nanoparticle may be defined as an amorphous or semicrystaline solid having at least one dimension less than 100 nm, while, a nanocrystal may be defined as a crystalline solid having at least one dimension less than 100 nm. Experiments involving these two materials are discussed in detail in the chapters to follow; however, background information about them will be discussed on the following pages.

Nanoparticles of the type discussed in this thesis are composed of a metallic core. The metallic cores are most commonly formed by the elements Au, Ag, Pt, or a combination of these, however, other metals have also been used to synthesize nanoparticles. In addition, these particles may be functionalized with various surfactants on the surface to either provide appropriate solubility or for their use in a particular application. Various routes for their synthesis have been determined, including reduction of a gold salt in the presence of growth stabilizing surfactants, electrochemical methods,

or seed-mediated synthesis. Of the above mentioned methods, the reduction of a gold salt to produce gold nanoparticles and their photoablative application will be discussed in chapter three.

Physical characteristics of these nanoparticles include a large density as a result of their metallic cores, the phenomenon of surface plasmon resonance arising from large absorption cross sections, and light scattering which may be utilized for applications such as contrast agents in microscopy, photoablation, and size distribution measurements, respectively.

Nanocrystals, on the other hand, possess single crystalline order and exhibit entirely different physical characteristics as compared to nanoparticles. The particular nanocrystals discussed in this text are semiconductor and Au nanocrystals, also known as quantum dots (QDs). While nanoparticles are typically used as contrast or light scattering reagents, quantum dots posses size dependant luminescent characteristics. Analagous to organic fluorophores, quantum dots may be used as luminescent probes, however, their photophysical characteristics prove advantageous over their classical counterparts. Semiconductor QDs exhibit broad excitation spectra, and size dependant narrow emission. As a result, QDs of various sizes, and thus differing emission spectra, may all be excited with a single wavelength. In addition, QDs prove resistant to photobleaching, which is of particular importance in biological applications. Long irradiation times and intensities may be used without a decrease in the emission signal from the QDs. Au QDs also possess all the above mentioned physical characteristics with a major difference arising in their excitation spectra; where semiconductor QDs exhibit broad excitation spectra, AuQDs exhibit narrow excitation spectra. In addition

QDs possess a large two-photon cross section. This results in excellent bioapplicability in that they may be used for thick specimen investigation and multiphoton excitation.

Various well studied routes for the synthesis of semiconductor QDs have been reported. The most common synthetic procedure involves a high temperature synthesis using toxic inorganic precursors which are injected into a hot coordinating organic solvent. These coordinating ligands act to limit the growth of the particles, while the concentration of the inorganic precursors and the growth time results in QDs of varying sizes. The direct synthesis results in particles with relatively low quantum yields of around 10%, however, a second capping step providing an outer shell of ZnS can enhance this quantum yield to approximately 80%. Following this synthetic procedure produces particles that are stabilized by organic ligands yielding poor water solubility. As a result, yet another step is typically required to impart water solubility and resistance against aggregation in aqueous solution; a common problem when dealing with QDs. Finally, in order for these particles to be of any practical use, other than to simply emit light upon excitation, a recognition element or compound to impart specific activity must be incorporated into the system; most typically through the use of covalent, electrostatic, or adaptor protein interactions. In the case of biological applications, the activity of the biomolecule of interest must not be disturbed upon conjugation. Other routes to the synthesis of these particles are available, for example the inverted micelle method, however, the same synthetic limitations as mentioned above hold true.

The methods for producing gold QDs do not rely on the above mentioned synthetic procedures. Only recently have these particles been reported in the literature, and they involve the reduction of a gold salt once it has been embedded within, or

between, a stabilizing and growth limiting dendrimer. Altering the concentration of precursors, or generation of the dendrimer, results in particles of varying sizes. While this synthetic scheme circumvents many of the limitations of semiconductor QD syntheses, very few applications involving these particles have been reported in the literature.

The thesis herein aims to present various relevant biological applications of nanoparticles and nanocrystals while highlighting methods for overcoming accepted limitations of the technologies. Chapter 1 concerns the main methodologies used throughout the text. Theoretical and practical aspects of the methods performed will be discussed. The aim of the second chapter is to validate the use of small peptides based upon the β-amyloid peptide, implicated in Alzheimer's disease, for use as a model system for the investigation of aggregated protein structures. Chapter 3 presents an application of gold nanoparticles and the short peptide fragments of chapter 2; photoablation of aggregated peptides by gold nanoparticles is investigated. An example application of gold QDs is the topic of the fourth chapter. A fluorescence quenching immunoassay based upon gold QDs for the detection of human IgG in solution with nanomolar detection limits is presented. Chapter 5 presents a novel single step synthetic strategy for the preparation of protein and enzyme stabilized CdS QDs that results in water soluble nanocrystals with biological activity. These particles, as synthesized, may be directly used for biological applications. Finally, chapter 6 summarizes the conclusion of the work presented and discusses limitations and considerations for future areas of research in nanotechnology.

Chapter 1. Methodology

The results presented in this thesis involved the use of various methods and techniques. It is not practical to describe in detail every technique and method used, however, in this chapter the most important and widely used will be discussed. Theory, experimental and equipment setup, and practical aspects will be discussed below while experimental details may be found in Chapter 7.

1.1. Langmuir films

The Langmuir monolayer and Langmuir-Blodgett film are two-dimensional technologies which require special methodologies for their preparation and retrieval of useful information. These methods are not widely discussed in the literature, although, there are several books and reviews dealing with the details of these techniques[1-3]. The general sample preparation and characteristic techniques along with equipment design involved in subsequent chapters are presented below.

1.1.1 Surface pressure-area isotherm

A Langmuir monolayer can be defined as an insoluble one-molecule thick layer of an organic material spread onto an aqueous subphase. The fundamental interfacial property of a Langmuir monolayer is the surface pressure-area isotherm (π–A isotherm). It is obtained by recording the surface pressure (or interfacial pressure), which is corrected for the surface pressure of the bare subphase, versus the molecular area of the

Langmuir monolayer; the π–A isotherm measures free-energy changes and reflects the packing status and phase behavior of the monolayer. Two main methods for measuring surface pressure are typically used: the Wilhelmy plate method and the Langmuir float method. Detailed description of these methods can be found in the literature[1]. The Wilhelmy plate method is the mostly used method in modern Langmuir trough systems. This method is used for all of the measurements detailed in the subsequent chapters. A rectangular filter-paper plate is dipped into the air-water interface with zero contact angle in regards to the subphase. Changes in the surface pressure (surface tension) are measured by the vertical pull on the plate and recorded by the force measurement detector connected to the plate. The force measurement detector may be calibrated by standard weights or surface pressure-area isotherm of a standard compound. The surface pressure is most commonly measured in units of mN/m. Below, in Figure 1.1, a schematic illustration of a minitrough with an attached spectrophotometer may be seen along with a photograph.

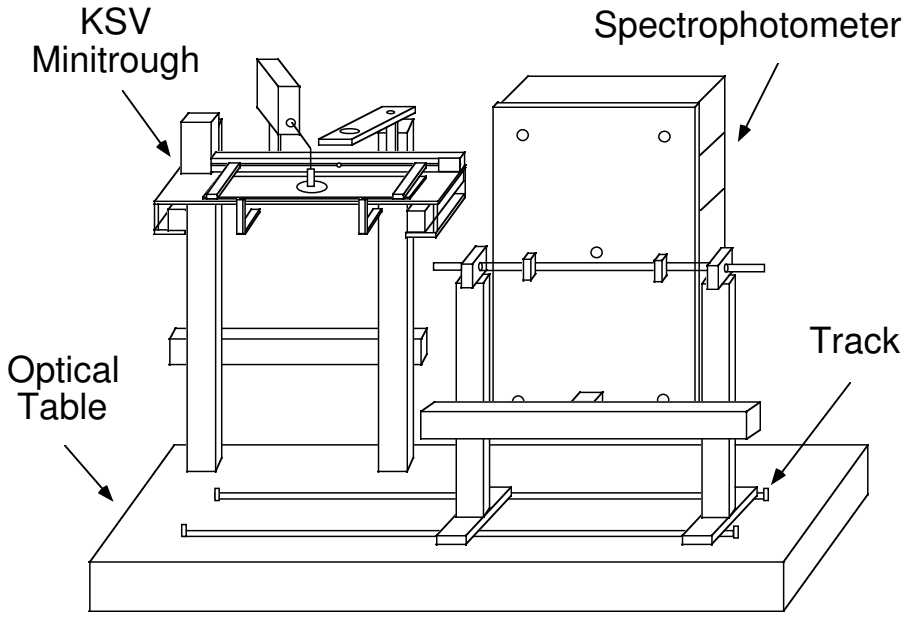

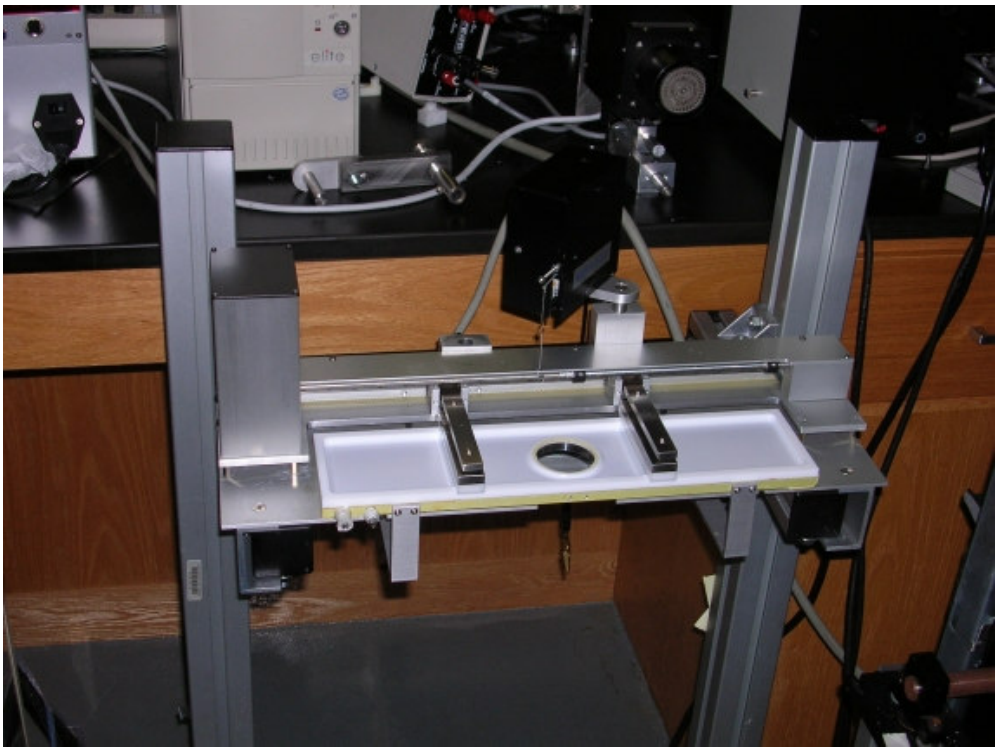

Figure 1.1. Above a schematic and below a photograph of A KSV Langmuir trough system with custom designed surface UV-Vis and fluorescence spectrometer.

Surface pressure-area isotherms presented in this thesis were recorded on a KSV mini-trough (KSV Instruments, Helsinki, Finland). The trough is made of Teflon and has an area of 30 × 7.5 cm^2. Two computer controlled opposable barriers from opposite sides of the trough can be compressed both simultaneously and symmetrically to avoid tilt of the Wilhelmy plate (Figure 1.1). The surface pressure sensor has a resolution of 0.02 mN/m. This sensor can be calibrated by a standard weight or surface pressure-area isotherm of a model compound such as arachidic or stearic acid on a pure water subphase (surface pressure of liquid to solid phase transition: 25 mN/m at 20 °C). For each isotherm experiment, 30 - 60 µl of the sample solution is spread on the water surface. After 20

minutes for solvent evaporation, the barriers are compressed at a typical speed of 4 mm min^{-1} (2.5 - 10 $Å^2$ $molecule^{-1}$ min^{-1}), although, this may vary depending on the sample amount and molecular mass.

1.1.2 Surface potential-area isotherm

The change in phase boundary potential produced by an interfacial film is defined as the interfacial potential or surface potential, ΔV. By recording the surface potential versus molecular area, the surface potential-area isotherm (ΔV–A isotherm) can be obtained. There are two main methods used to record the surface potential: the ionizing electrode method and the vibrating plate method. [1] Both methods measure the potential difference between two electrodes, one in the subphase and the other in the air. The ionizing electrode method uses a radioactive air electrode to ionize the gap between the air electrode and the surface to make it conducting. The vibrating plate method is a capacitor based method, using alternating current generated by the air electrode to detect the potential change on the surface.

From the surface potential-area isotherm, information about the molecular orientation and heterogeneity of the film can be obtained. Surface potential depends on three factors: the concentration of film molecules, the contributions from the dipoles in the film, and, in the case of a charged monolayer, the electrical potential Ψ_0, in the plane of the charged groups. The surface potential, therefore, is measure of the average of the three above mentioned contributions and can be interpreted by the following equation:

$$\Delta V = 4\pi n\mu/D + \Psi_0 \qquad (2.1)$$

where n is the number of dipoles (usually number of molecules) per unit area, μ is the effective interfacial dipole moment in the perpendicular direction, and D is the dielectric constant, which is normally assumed to be unity. μ can be interpreted by

$$\mu = \overline{\mu} \cos\theta \tag{2.2}$$

where $\overline{\mu}$ is an intrinsic moment making an angle θ with the vertical. For non-charged monolayers, $A\Delta V$ is proportional to μ, thus the molecular orientation angle θ can be obtained. For charged monolayers, the effect of the term Ψ_0 can be studied by fixing the area of the monolayer in order to fix the term $4\pi n\mu/D$ in Equation (2.1). Then changing the subphase pH or ionic strength to change the charge status of the monolayer, and recording the change of ΔV.

The surface potential is also a valuable method for detecting heterogeneity in the monolayer. When moving the air electrode over the surface, the presence of heterogeneity is made evident by wild fluctuations of the surface potential. This can be used to investigate the completeness of spreading or phase changes in monolayers.

Surface potential-area isotherms described in this thesis were measured on a KSV trough. Two computer controlled symmetrically movable barriers were used to regulate the surface area. The area of this trough is 100 × 12 cm^2. The surface potential was measured by using a Kelvin probe.

1.1.3 Spectroscopy at the air-water interface

Various spectroscopic methods may be extended to the investigation of thin films at the air-water interface including fluorescence, UV-Vis absorption, and infrared

spectroscopies. Of these techniques, infrared spectroscopy provides a powerful method of investigation which may provide a wealth of information about a given system. Infrared spectroscopy allows for the detection of functional groups in molecules, molecular orientation, and determination of the secondary structure of proteins, all at the air-water interface. Specific equipment and setup are requisite for the application of spectroscopy to the air-water interface. In the case of IR spectroscopy, an FTIR spectrometer is needed that allows for the radiation to leave the spectrometer followed by a series of focusing mirrors for sample interaction. Additionally, a highly sensitive detector must be employed that is capable of a high signal-to-noise ratio, rapid scanning rates, and excellent resolution. A photograph of the above mentioned components is presented below in Figure 1.2.

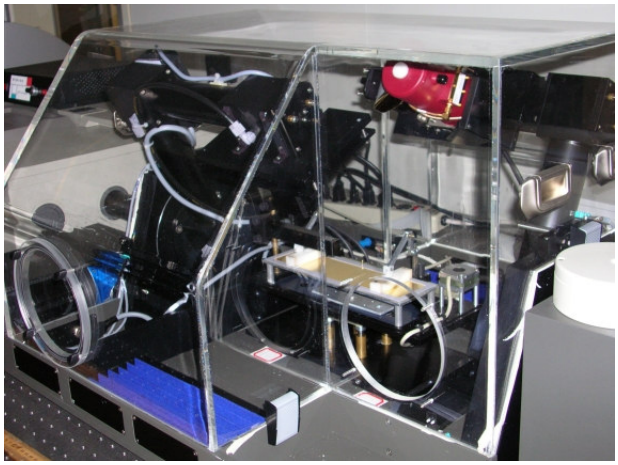

Figure 1.2. Bruker Optics XA-511 main accessory for air-water interface measurements attached to an Equinox 55 FTIR spectrometer for IRRAS and ATR measurements.

1.1.4 Epifluorescence microscopy

Epifluorescence microscopy is a method of investigation that may be used to image monolayers or various solid samples with the aid of a fluorophore; whether intrinsic or extrinsic. In general a microscope with an excitation source is placed above the sample stage, in the case of surface chemistry measurements, above the Langmuir trough. This source of excitation is most commonly a xenon or mercury lamp with multiple filters in place between the source and specimen in order to provide a method for changing the excitation wavelength and to block the excitation for observation of the emitted light. In the case of the measurements taken in this text, a CCD camera is used to record the microscopic image produced by the emission of the fluorophore. Distinguishing epifluorescence microscopy from regular microscopy, in addition to the use of fluorophores and the capability to select an excitation wavelength, is that the observed light is emitted from the sample and collected above the specimen. A schematic representation of a typical epifluorescence microscope is presented below in Figure 1.3 while a photograph of the actual microscope used can be seen in Figure 1.4.

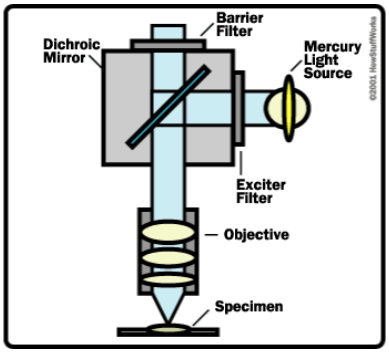

http://static.howstuffworks.com/gif/light-microscope-diagram-1.gif

Figure 1.3. Schematic representation of an epifluorescence microscope setup.

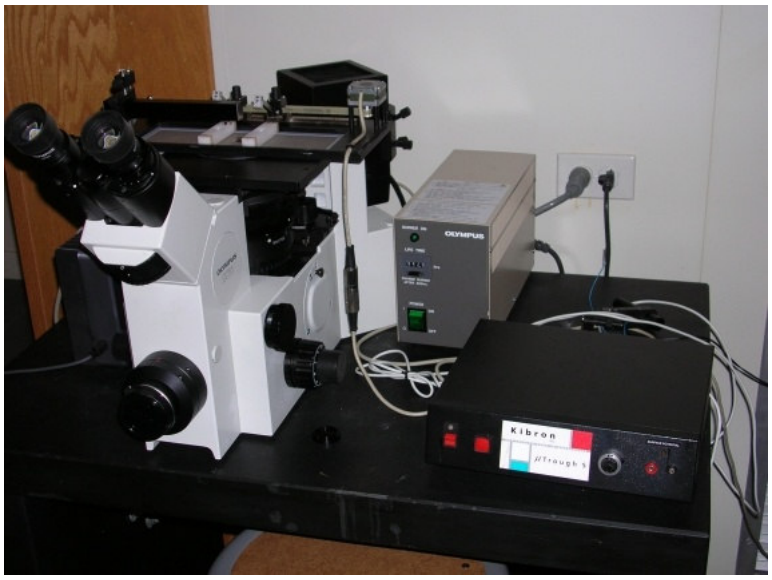

Figure 1.4. Olympus IX-70 inverted microscope with Kibron trough for the acquisition of epifluorescence microscopic images.

1.2 Langmuir-Blodgett films

A Langmuir monolayer at the air-water interface can be transferred to a solid support by two main methods: Langmuir-Blodgett deposition and Langmuir-Schaefer transfer. Langmuir-Blodgett deposition is shown in Figure 1.5. Monolayers or multilayers can be obtained by dipping a hydrophobic slide into and out of a monolayer-covered liquid interface. This has become known as the Langmuir-Blodgett (LB) technique after the two scientists who pioneered the method.[5,6] It is usually necessary to have a close-packed monolayer for successful deposition. The surface pressure is preferably maintained constant by barrier movement. This allows the transfer ratio to be easily established – that is, the ratio of the area decrease of liquid interface to the immersed area of slide. This ratio should be close to unity for satisfactory transfer,

however in practice this is not always the case. Various materials can be used as the solid support as needed, including glass, quartz, graphite and mica. The success of the monolayer transfer depends on many factors including the nature of the monolayer and its purity, the composition of the subphase, uniformity in the surface properties of the solid support, and the need to have a coherent monolayer at a finite interfacial pressure.

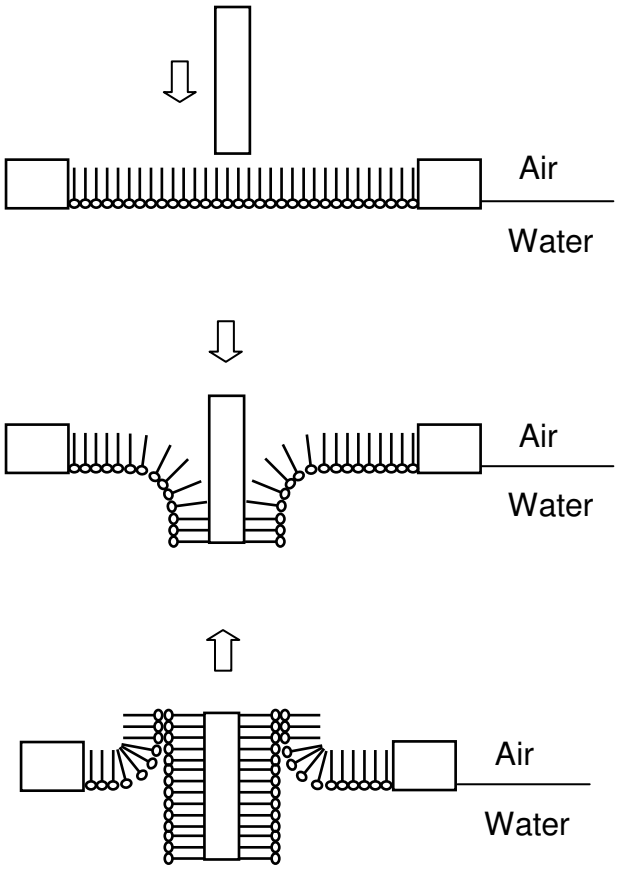

Figure 1.5. Schematic representation of Langmuir-Blodgett deposition of an amphiphilic molecule onto a hydrophobic substrate.

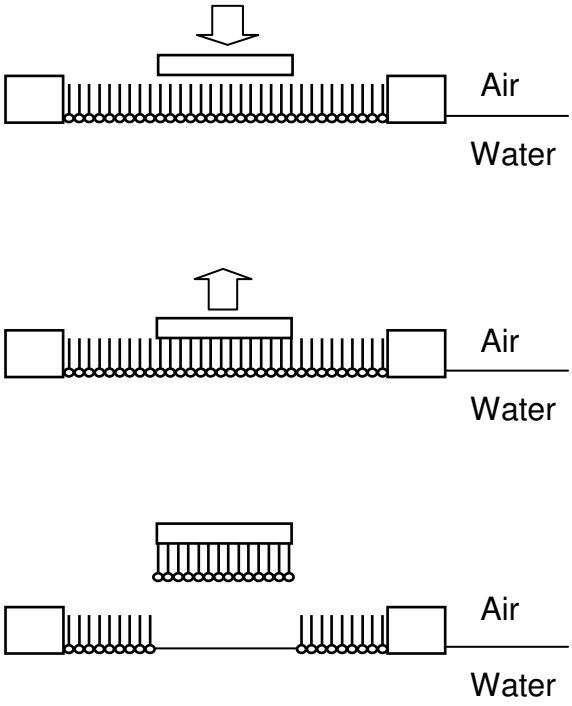

Figure 1.6. Schematic representation of Langmuir-Schaefer transfer of an amphiphilic molecule onto a hydrophobic substrate.

The Langmuir-Schaefer transfer method is shown in Figure 1.6. A hydrophobic substrate horizontally touches the Langmuir monolayer at the air-water interface and then it is

removed with the monolayer attached to the substrate. The advantage of Langmuir-Schaefer transfer is that it can transfer monolayers with relatively low surface pressure, which is not always possible using the Langmuir-Blodgett film method. This method also negates the need for a dipping chamber in the subphase, thus dramatically reducing the subphase volume, which is a critical factor for quantity limited subphase solutions composed of such compounds as proteins or toxins. A limitation arises in that the monolayer to be deposited on the substrate can only have the hydrophilic group exposed to the air on the substrate and normally only one layer can be obtained.

Three types of multilayer structures (X, Y and Z type) are possible depending on how transfer is effected during the dipping process, as depicted in Figure 1.7. The Langmuir-Blodgett method was used in the results presented. In X-type deposition, the tail of the amphiphilic molecule is first deposited directly on the substrate surface. Subsequent molecules are deposited in a head to tail fashion. For Y-type deposision, the molecules of the first monolayer are deposited tail first, followed by a head to head arrangement for the following layers. In the case of Z-type deposition, the first monolayer is deposited so that the head groups are in contact with the substrate surface. The remaining layers are deposited so that there is a tail to head interaction.

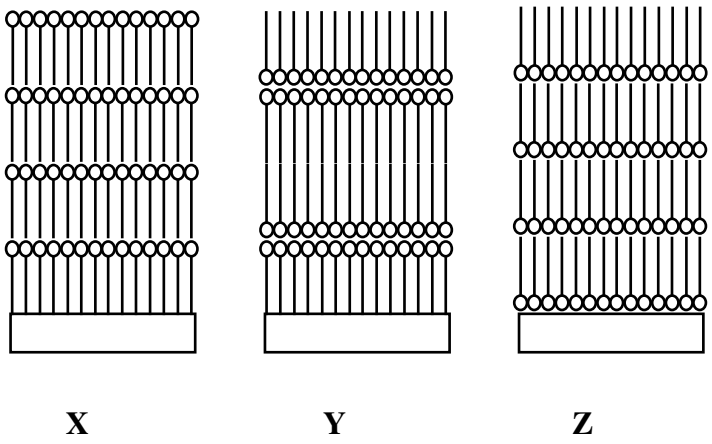

Figure 1.7. Schematic representation of the three types of L-B deposition of amphiphilic molecules onto a solid support. Circles represent hydrophilic head groups while lines represent hydrophobic tail groups.

Characterization of LB films

A large number of experimental techniques can be used to characterize transferred monolayers and LB films: simple techniques such as contact angle measurement; spectroscopy techniques including ellipsometry, electron-spin resonance, infrared dichroism, circular dichroism, polarized resonance Raman spectroscopy and IETS; diffraction techniques as transmission electron, X-Ray and neutron diffraction; and microscopic techniques such as surface plasmon, Brewster angle, epifluorescence, surface probe, transmission electron and environmental scanning electron microscopy, etc.[1] The main method used to characterize the LB films produced in the work on the following pages was circular dichroism spectroscopy for the purpose of identifying the secondary structure of peptide based samples. A photograph of the Jasco J-810 circular

dichroism spectrometer used for the acquisition of CD spectra can be found in the photograph below.

Figure 1.8. Jasco J-810 circular dichroism spectrometer.

To minimize the possible contamination, all surface chemistry experiments are performed in a state-of-the-art class 1000 clean room (Chemistry annex room 141). This room has temperature (20.0 ± 0.5 °C) and humidity (40 ± 5 %) control, and the number of dust particles in this room are less than 1000 per cubic feet.

1.3 Solid-phase peptide synthesis (SPPS)

While various strategies for synthesizing peptides and proteins exist, the most proven and reliable for producing short peptides of a known sequence involves solid phase peptide synthesis (SPPS), first developed by R.B. Merrifield[7]. Two main strategies

are most commonly employed; the Merrifield developed tert-Butoxycarbonyl (Boc) based synthesis or fluorenylmethoxycarbonyl (Fmoc)[8-10] based synthesis. These two synthetic procedures are named for the protecting groups used. The main difference in practice is that Boc synthesis involves an acid labile protecting group while Fmoc synthesis involves a base labile protecting group. All the peptides synthesized in the following pages were performed using Fmoc based synthetic procedures, and therefore, this is the method that will be discussed. The general procedure and concepts are illustrated in Figure 1.9 below. An insoluble solid support most typically a polymer resin—the choice of which will result in the completed peptide in either acid or amide form-- is attached to an N-α-Fmoc-derivatized amino acid through the use of a linker. This Fmoc protecting group is then removed, followed by multiple washing cycles. The subsequent amino acid to be attached (also N-α-Fmoc-protected) is then coupled to the first amino acid which is

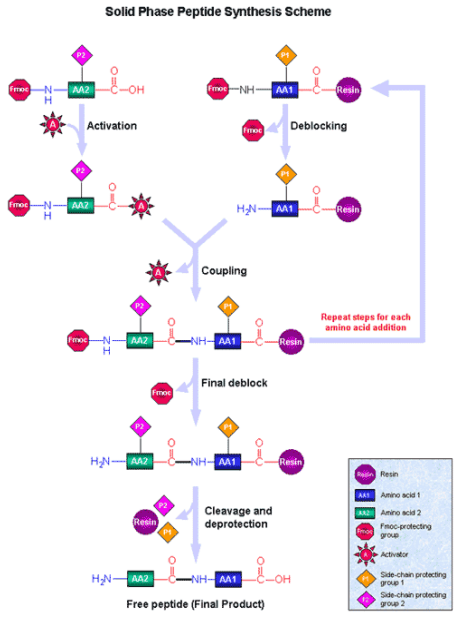

http://www.sigmaaldrich.com/img/assets/22080/Solid_phase_syn_schem_SMALL.gif

Figure 1.9. General scheme outlining the principle of solid phase peptide synthesis.

attached to the solid support. The coupling of the amino acids can be accomplished in one of two ways; either as an active ester or in the presence of an activator. The latter of the two has been used for the synthesis of peptides mentioned in the text through the use of carbodiimide activating agents. Following coupling, numerous washing cycles are performed in order to remove any unreacted amino acids, coupling, and activating reagents. A ninhydrin test may be performed after each coupling reaction to ensure efficient coupling has indeed occurred. The above mentioned deprotection and coupling procedures are repeated in order to elongate the peptide chain until the desired peptide has been synthesized. Once the elongation phase has been completed, cleavage of the peptide from the solid resin support takes place. Under ideal conditions the cleavage reaction will also remove amino acid side chain protecting groups which are stable under the conditions used in the deprotection step.

In theory the above mentioned steps appear to be straightforward and the synthesis of peptides of relative ease, however, due to side reactions involving side chain protecting groups, in practice the correct solid support, linker, amino acid derivatives, coupling, activating, and cleavage reagents must be determined for each individual peptide being synthesized.

The synthetic reactions themselves may be carried out either manually in SPPS specific glassware or through the use of an automated peptide synthesizer in which all reagents are pre-loaded into the system and the protocol programmed into software designed for such a purpose. Both methods have been used for the synthesis of peptides

mentioned in the text. A photograph of the AAPTEC APEX 396 fully automated peptide synthesizer used can be found below in Figure 1.10. For the purposes of synthesizing short peptides, it has been found that the manual synthesis results in peptides of greater yield and purity. However, if large quantities or peptides of longer sequences are needed, the automated method is preferable, although the yield and purity may be low.

Figure 1.10. AAPTEC Apex 396 fully automated peptide synthesizer.

1.4 Solution spectroscopy

Three types of solution spectroscopy are employed in the research contained within this thesis; they are absorption, fluorescence, and infrared spectroscopies. In the text on the following pages absorption and fluorescence spectroscopies are primarily used as a tool to characterize the optical properties and by extension physical parameters of quantum dots, while infrared spectroscopy is used in order to investigate the secondary structural characteristics of peptide and protein based systems.

Luminescence may be defined as the emission of light from a substance that occurs from electronically excited states. Luminescence may be further subdivided into two distinct categories. Fluorescence which arises from an excited singlet state occurs when an electron in an excited orbital returns to a ground state orbital. This phenomenon occurs rapidly as the electrons in the two orbitals are spin paired and thus relaxation is spin-allowed which is accompanied by the emission of a photon. Phosphorescence is emission of light from excited triplet states. In this case the electron in the excited orbital possesses the same spin as the electron in the ground state. Relaxation to the ground state is forbidden resulting in slow emission rates.

As these techniques are applied to quantum dots, which are most commonly composed of semiconductor materials, a different theoretical explanation is required. Quantum dots are semiconductor nanoparticles: the size of the particles range from a few up to about 10 nanometers and exhibit discrete size dependant energy levels. These energy levels are a result of quantum confinement effects due to their small size; the Fermi wavelength is on the same order of magnitude as the size of the particles themselves resulting in electronic properties distinct from the bulk solids. As the size of the particle increases so does the energy gap. The semiconductor material may be excited resulting in a localization of electrons towards the surface leaving positively charged holes behind. When the electron reaches a surface defect or comes into contact with a hole, emission of light occurs; luminescence is observed.

Various compounds are capable of absorbing light, and from this absorption of light useful information-- both structural and quantitative-- about the system may be

gained. The Beer-Lambert provides for a description of the absorbance of light by a given material.

$$A = \varepsilon c l \tag{2.3}$$

Where A is the observed absorbance (in practice this is related to the amount of light transmitted through the sample), ε is the molar extinction coefficient, c is the concentration of the sample, and l is the pathlength through the sample.

Infrared spectroscopy is used primarily in this work as a tool for secondary structure determination in proteins. In general, infrared spectroscopy is used to determine the specific vibrational frequencies present in a sample which can be attributed to the presence of particular bond types and by extension functional groups and secondary structures in peptides and proteins. Two bands of interest in IR spectra for the determination of secondary structure are the amide A and amide B bands, both of which arise from a Fermi resonance between the first overtone of the amide II and N-H stretching vibrations. Additionally, the amide I band is mainly due to carbonyl stretching vibrations and this is directly related to the peptide backbone conformation. The amide II band results from N-H bending and C-N stretching and these are also conformationally sensitive.

1.5 Photoablation

When a material absorbs light and is consequently excited, this energy may be dissipated in various ways. Radiatively the energy may be dissipated through

fluorescence or phosphorescence as detailed above; however, non-radiative pathways also exist. Photoablation utilizes non-radiative pathways of relaxation. In the text to follow photoablation of peptide aggregates by gold nanoparticles is discussed. Gold nanoparticles on the order of a few to tens of nanometers exhibit a strong surface plasmon resonance band around 520 nm. When a gold nanoparticle is subjected to excitation at the wavelength of the surface plasmon resonance band, the nanoparticle becomes excited. The non-radiative relaxation that occurs follows a photothermal mechanism in which the energy of the hot electron gas may thermally equilibrate with the nanoparticle lattice which is followed by a release of heat to the surroundings. This heat released may be utilized for work. Most commonly this heat is used to ablate the surface of materials, i.e. photoablation.

Chapter 2. Amyloid peptide fragments as model for aggregated protein: A two dimensional approach

2.1 Background

While the work presented in this chapter is not a direct application of nanotechnology for the detection of biological analytes, the peptides involved will later be used for these purposes. Most of this work is aimed at determining the feasibility of using short peptides as model a model system for protein aggregation. In the process of answering this question of feasibility, a novel two dimensional approach incorporating surface chemistry, spectroscopy, and microscopy was formulated. The techniques and experiments in this chapter show both the flexibility and analytical capabilities of spectroscopy and microscopy applied directly to surface chemistry.

Alzheimer's disease (AD)[11] is the most common cause of senile dementia affecting the brain. Two specific forms of protein and peptide deposits have been identified in brain nerve cells of AD patients: intracellular neurofibrillary tangles and extracellular neuritic plaques (fibrils) or senile plaques.[12-14] Neurofibrillary tangles consist of insoluble twisted fibers that are found within neurons, they are primarily composed of a protein referred to as *tau*. In contrast, senile plaques are formed by deposits of amyloid β peptide (Aβ).[15] The 39-43-amino acid peptide fragment of Aβ forms neuritic deposits in the brain of AD patients that are used as the hallmark indicator of AD.[16-18] Recently solid state NMR studies have presented evidence that the conformation of Aβ is characterized by a parallel β-sheet structure,[19] moreover, aggregation arises due to the hydrogen bonding between β-strands, and the resulting

fibrils have axes perpendicular to the β-strand and parallel to the cross-linking hydrogen bonds.

Among all the Aβ derivatives that have been well investigated, Aβ sequence 25–35 (GSNKGAIIGLM) is the most frequently studied fragment that exhibits large β-sheet fibril formation and at the same time maintains the toxicity of the full length Aβ peptide.[20,21] Aβ(25–35) has been proposed to represent the biologically active region of Aβ. It has also indicated that this fragment, in a manner similar to that of Aβ(1-42), undergoes a conformational transition from a soluble, random-coil form to aggregated fibrillary β-sheet structures. When solubilized and unfolded in 0.1% trifluoroacetic acid in water: acetonitrile (65:35; v/v) mixture solvent,[22] the toxicity of Aβ(25-35) is dependent on the aggregation state of the peptide.

In the present work a two dimensional (2D) approach is applied to the study of Aβ aggregation. The feasibility of investigating Aβ fragment (31-35) at the air-water interface by surface chemistry, microscopic, and spectroscopic techniques has been previously reported by the Leblanc group.[23] Compared with the conventional methodologies, the 2D approach has the advantage of simulating the aggregation process that occurs in vivo in aqueous solution, a process that is accomplished using the compression of the monolayer as means to bring the peptides in close contact for assembly. Furthermore, real time microscopy may be employed to observe the topography of the Langmuir monolayer and spectroscopic techniques to study the organization and conformation of the peptide moiety. While the Leblanc group has previously used the 2D approach to study smaller fragments of the Aβ peptide[23], herein, the approach is extended to include stability measurements (compression-decompression

cycles), PM-IRRAS of the Langmuir monolayer, and CD measurements of Langmuir-Blodgett films of Aβ in order to gain insight into the nature of the secondary structure of the fibrils. Herein, the 2D approach in solution is extended to a longer, well studied, fragment of Aβ, namely Aβ(25-35), and compared to the shorter peptide fragments Aβ(31-35) previously studied by the Leblanc group[23] as Langmuir monolayer.

2.2 Synthesis of peptidolipid amyloid peptide fragments

To assure the stability and self-assembly of the peptide moiety at the air-water interface, a fatty acid (C_{18}) is covalently linked to the N-terminal of the Aβ(25-35) peptide (see Figure 2.1).

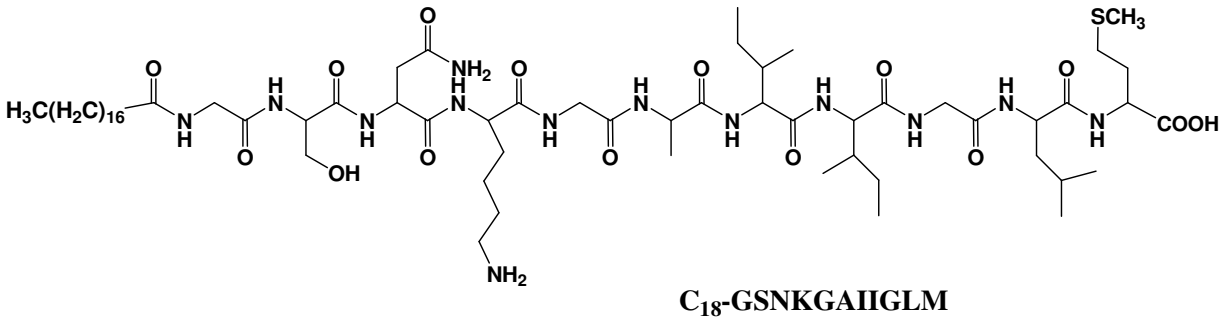

C_{18}-GSNKGAIIGLM

Figure 2.1. Chemical structure of peptidolipid C_{18}-Aβ(25-35): C_{18}-GSNKGAIIGLM-OH.

The aliphatic chain does not affect the aggregation behavior of the functional peptide moiety at the air-water interface because the hydrophobic tail is pointed upwards to the air phase upon compression of the Langmuir monolayer; it does not lie in the same phase as the peptide portion of the molecule. Peptidolipid Aβ(25-35) was prepared by the solid-

phase methodology on Wang resin (1.3 mmol/g). Briefly, coupling reactions were carried out with a 3-fold excess of Fmoc-amino acids with diisopropylcarbodiimide(DIC) / 1-hydroxybenzotriazole (HOBT) as activating agent in dimethylformamide (DMF). Intermediate deprotection was achieved with 20% (v/v) piperidine in DMF for 30 min. After an average coupling period of 1 h, the extent of acylation was monitored via the standard ninhydrin test. In the event of incomplete coupling, the coupling procedure was repeated. After final deprotection, stearoyl chloride was coupled to the peptide-resin using the same coupling protocol as mentioned above to yield the peptidolipid product. The cleavage of the peptidolipid from the resin was performed with trifluoroacetic acid in the presence of 8% anisole, 2% dimethyl sulfide, 2% p-cresol, and 2% thiocresol at 0 °C for 2 h. After removal of the trifluoroacetic acid under a stream of nitrogen followed by vacuum, the crude peptidolipid was precipitated with diethyl ether, filtered off, washed with water and diethyl ether, extracted with 50% (v/v) aqueous acetic acid, and lyophilized. The synthesized peptidolipid was purified by semipreparative reversed-phase high-performance liquid chromatography (RP-HPLC) on a Waters 2690 separation module. Eluants used were 0.1% trifluoroacetic acid in water (v/v; A) and 0.1% trifluoroacetic acid in n-propanol : acetonitrile (50:50, v/v; B). Column conditions: Vydac 219TP1010 (diphenyl, 10 μm, 10 mm i.d.×250 mm).

The purity of the synthesized peptidolipid was verified by analytical RP-HPLC, ^{1}H-NMR and MS. Analytical RP-HPLC was conducted on a small-scale column (Vydac 219TP54, diphenyl, 5 μm, 4.6 mm i.d.×150 mm). The same eluants were used as described above and elution gradient was 100-85% B in 50 min; the flow rate was 0.6 ml/min. The purity was greater than 95%.

2.3 . Langmuir films of amyloid peptide fragments

All the isotherm measurements were conducted in a clean room [class 1000] where constant conditions of temperature (20.0 ± 0.5°C) and humidity (50 ± 1%) were maintained. The spreading solvent was 0.1% TFA in chloroform : methanol (5:1; v/v), and the solvents [HPLC grade] were purchased from Fisher Scientific Co. (Pittsburgh, PA). The water utilized as subphase (pH 5.8) for the monolayer study was purified by a Modulab 2020 water purification system (Continental Water System Corp., San Antonio, TX) with a specific resistivity of 18 MΩ·cm and a surface tension of 72.6 $mN \cdot m^{-1}$ at 20.0 ± 0.5 °C. The spreading volume of the peptidolipid solutions (4×10^{-4} mmol ml^{-1}) was 30-60 μL. After the solution was spread, a 15 min period was allowed for complete evaporation of the spreading solvent prior to compression. The compression rate for the Langmuir trough was set up at 8 mm min^{-1}. A KSV mini-trough (KSV Instrument Ltd., Helsinki, Finland) was utilized for surface pressure-area isotherm measurements. Computer-controlled symmetrically movable barriers were used to regulate the surface area. The area available for spreading solution was 7.5×30.0 cm^2. The surface pressure was measured by the Wilhelmy method with a sensitivity of ± 0.01 $mN \cdot m^{-1}$. Surface potential measurements were obtained on the KSV trough using a Kelvin probe. This probe consisted of a capacitor-like system. The vibrating plate was set at approximately 1 mm above the surface of the Langmuir monolayer and a counter electrode was dipped into the clean subphase which was taken as the zero reference. All the surface pressure and surface potential-area isotherms were measured at 20.0 ± 0.5 °C.

2.4 Surface pressure- and surface potential-area isotherms

The surface pressure (π) and the surface potential (ΔV) isotherms as a function of the surface area (A) per molecule of the amphiphilic peptidolipid are presented below in Figure 2.2.

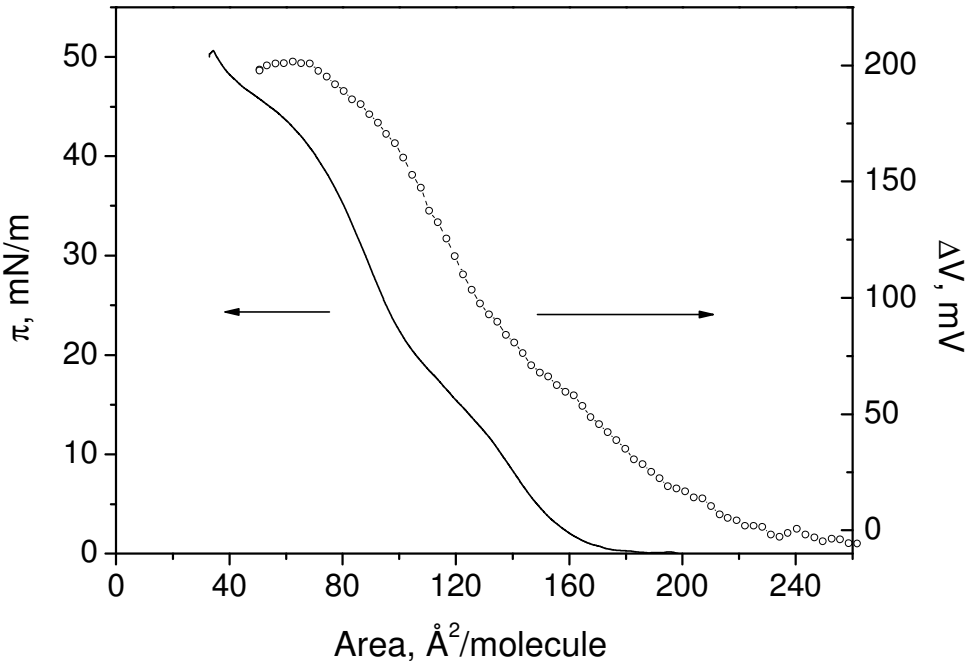

Figure 2.2 Surface pressure and surface potential-area isotherms of the peptidolipid C_{18}-Aβ(25-35) Langmuir monolayer.

The π-A isotherm is the average of three measurements with an error within ±0.5%. As shown in Figure 2.2, the surface pressure is nil beyond 180 $Å^2 \cdot molecule^{-1}$ followed by a lift-off at a molecular area of 180 $Å^2 \cdot molecule^{-1}$ and more than one kink point appears on the isotherm at different compression stages indicating the presence of various

component phases. From nil surface pressure to the first kink point (molecular area 130 $Å^2$·molecule^{-1}), the Langmuir monolayer is in the liquid expanded (LE) phase. From the second (molecular area 101 $Å^2$·molecule^{-1}) to the third kink point (molecular area 70 $Å^2$·molecule^{-1}), the Langmuir monolayer appears in the liquid condensed (LC) phase and above the third kink point, the monolayer collapses. Extrapolation of the linear portion of the isotherm between 25 and 35 mN·m^{-1} to nil surface pressure gives a limiting molecular area of 133 $Å^2$·molecule^{-1} for the peptidolipid C_{18}-Aβ(25-35), which is the area for a single peptidolipid molecule in a close-packed arrangement calculated from the CPK model.

As expected, the surface potential-area isotherm shows an early lift-off at 230 $Å^2$·molecule^{-1} due to the dipole-dipole interactions that appear at larger distance between the polar moieties (coulombic interactions have a r^{-2} dependence) as compared to surface pressure measurements (van der Waals forces have a r^{-6} dependence, where r is the intermolecular distance). From a surface area of 230 to 130 $Å^2$·molecule^{-1}, the surface potential increases gradually from 0 to 82 mV. This gradual increase corresponds to a change of the surface pressure from nil to 23 mN·m^{-1}. It can be interpreted that the hydrocarbon chain of the peptidolipid begins to lift-up into the air, which indicates a phase transition from a liquid expanded to a liquid condensed phase. The kink point at 101 $Å^2$·molecule^{-1} confirms this phase transition. Further compression below 101 $Å^2$·molecule^{-1} resulted in an increase of the surface potential up to 200 mV, with a shallower increase that is due to the high packing of the monolayer where the polar moieties are in close proximity. Below 80 $Å^2$·molecule^{-1} the surface potential flattens out, which indicates that the peptide moieties are in very close proximity which cause the

dipole to be constant, and starts decreasing indicating the collapse of the Langmuir monolayer.

The stability of the peptidolipid C_{18}-Aβ(25-35) Langmuir monolayer at the air-water interface was examined by compression-decompression cycle measurements. The results are shown in Figure 2.3, below.

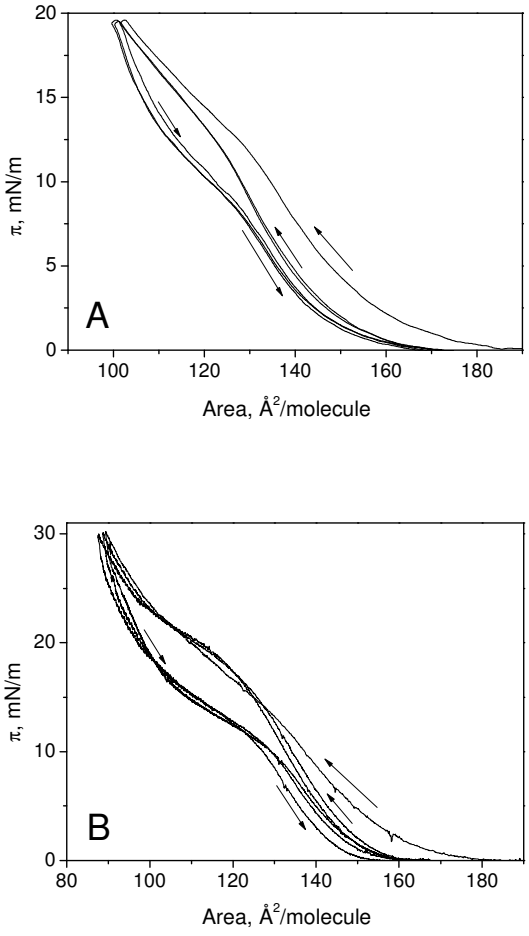

Figure 2.3. The compression-decompression cycles of peptidolipid C_{18}-Aβ(25-35) Langmuir monolayer at(A) 20 and (B) 30 $mN \cdot m^{-1}$.

Three cycles of compression-decompression were performed at surface pressures of 20 and 30 $mN \cdot m^{-1}$, note that at both surface pressures the isotherms present a hysteresis, indicating that domains are formed in 2D. Upon decompression these domains will remain intact; as the barriers are relaxed, the Langmuir monolayer relaxes, however, the interaction between polar moieties are stronger than the interaction between the polar moieties and the subphase. Due to this characteristic of the Langmuir monolayer, once formed, even after decompression, the domains will remain intact and hysteresis is observed.

2.5 Microscopic and spectroscopic studies at the air-water interface

The epifluorescence micrographs of peptidolipid Aβ(25-35) are presented in Figure 2.4. The micrographs are presented at four different surface pressures that allow visualization of domain formation during the compression.

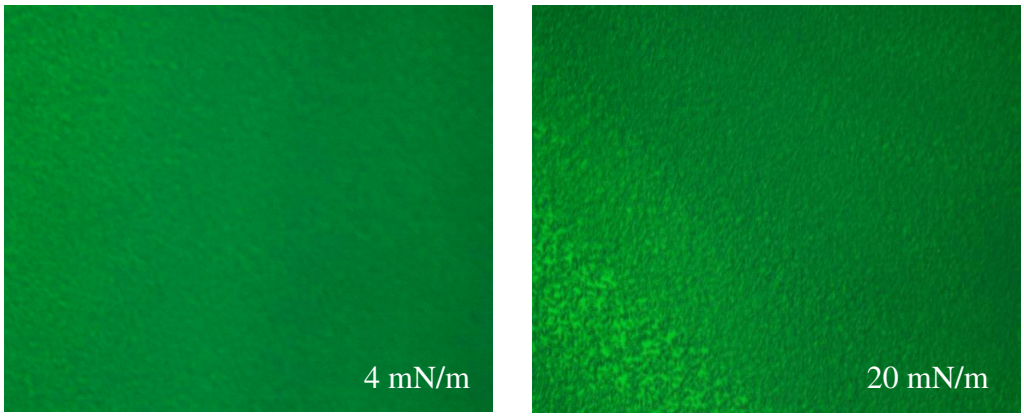

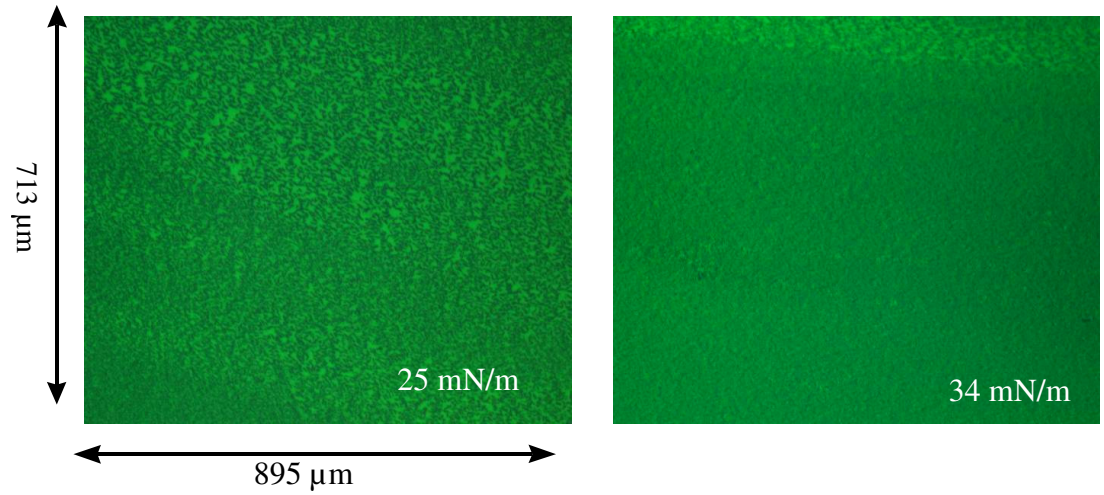

Figure 2.4. Epifluorescence micrographs (713 µm x 895 µm) of peptidolipid C_{18}-Aβ(25-35) Langmuir monolayer in the presence of FITC taken at surface pressure 4, 20, 25 and 34 $mN \cdot m^{-1}$.

At low surface pressure (4 $mN \cdot m^{-1}$), the Langmuir monolayer is quite homogeneous, and no domains can be observed. Compression of the film to higher surface pressure (20 and 25 $mN \cdot m^{-1}$), i.e. in the liquid condensed phase, gives rise to the aggregation process in the Langmuir monolayer. The shape of these domains is acicular and they are of uniform size. Further compression (34 $mN \cdot m^{-1}$ and higher) led to the formation of a greater number of domains which self-assembled to present a more homogeneous Langmuir monolayer. Some aggregates are still visible, however, due to the resolution of the epifluorescence microscope the micrographs became unclear. The domains formed upon compression remain during decompression. A direct comparison of the domains during compression and decompression may be found below in Figure 2.5.

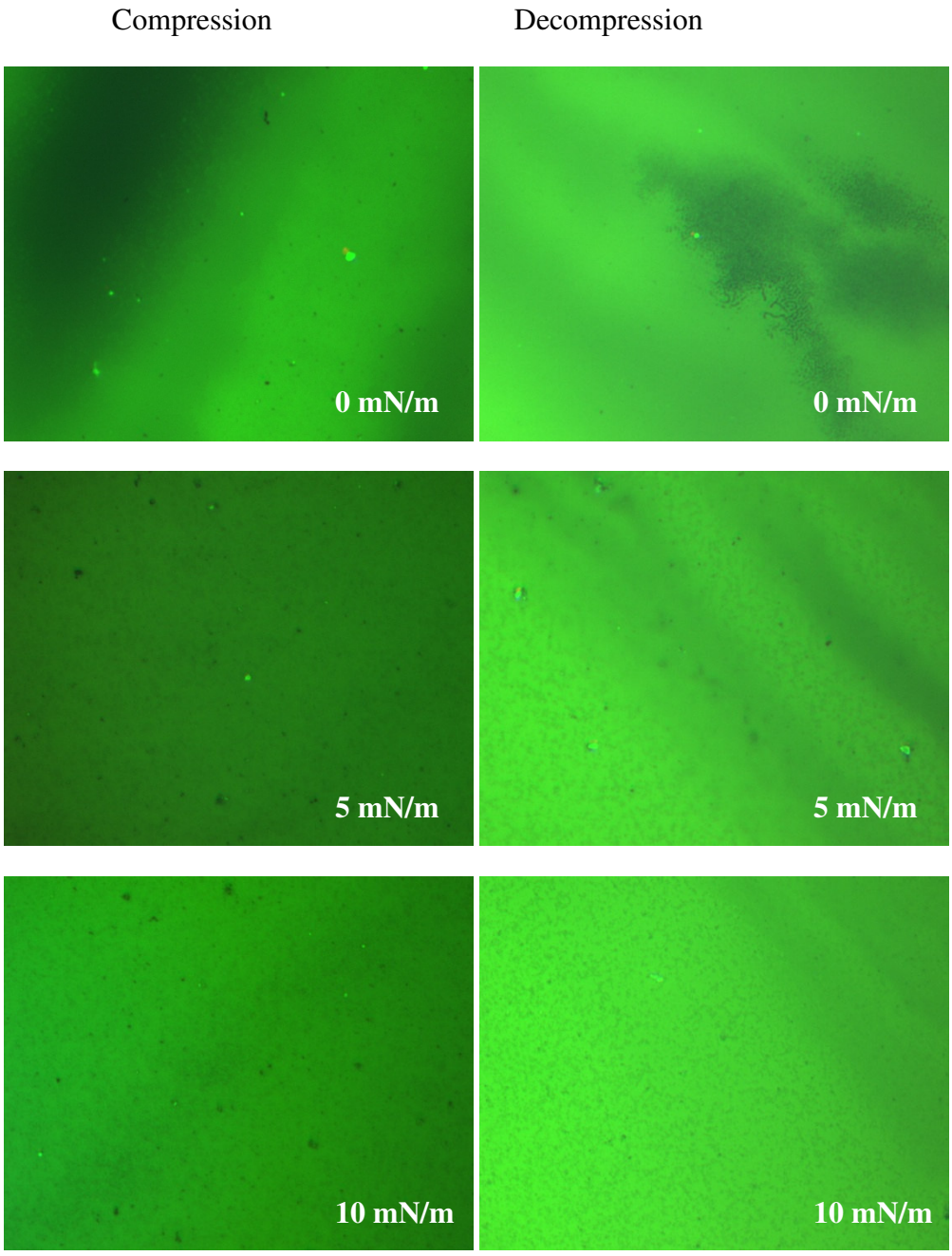
Compression
Decompression
0 mN/m
0 mN/m
5 mN/m
5 mN/m
10 mN/m
10 mN/m

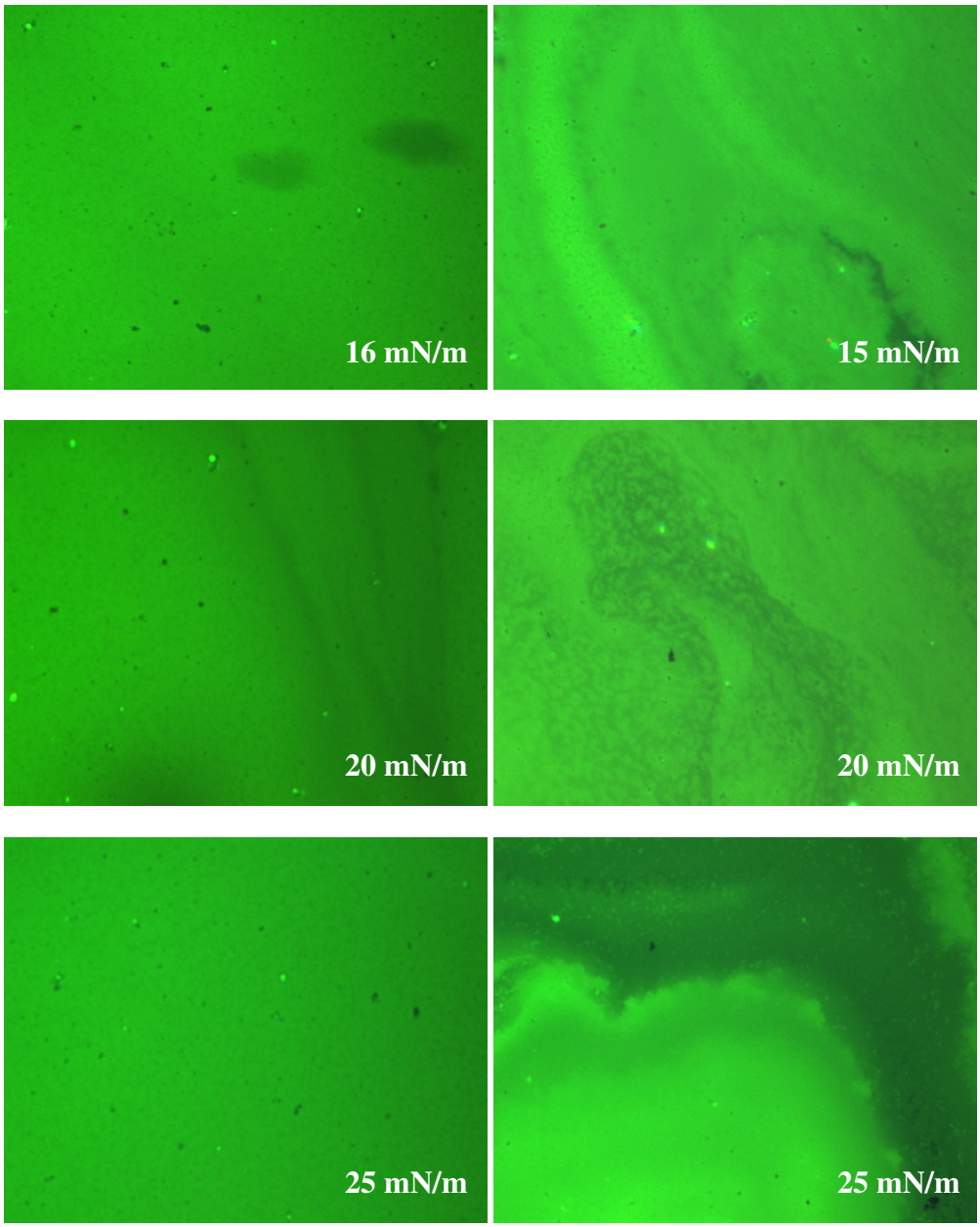
16 mN/m
15 mN/m
20 mN/m
20 mN/m
25 mN/m
25 mN/m

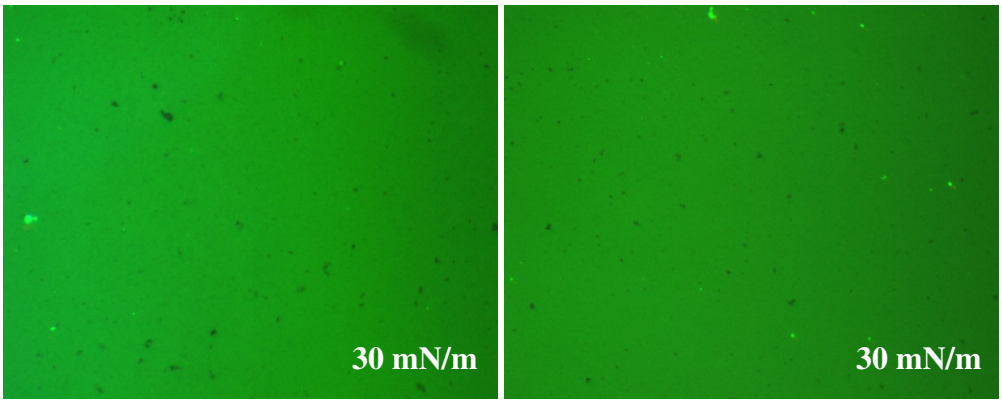

Figure 2.5. Epifluorescence micrographs for C_{18}-Aβ(25-35) during compression (left column) and decompression (right column).

PM-IRRAS is a useful spectroscopic technique to obtain insight into the molecular structures and to provide an analysis of the conformation of the peptide at the air-water interface.[24,25] For peptides two major bands providing useful structural data, namely the amide I and the amide II bands, are observed in the 1700-1600 and 1600-1500 cm^{-1} region, respectively. β-sheet structures are assigned in the amide I region at 1623-1643 cm^{-1}, furthermore, small absorbance bands in the 1685-1695 cm^{-1} range are also observed from high frequency β-sheet components. While the broad band at about 1535 cm^{-1} and the weaker bands near 1563 and 1650 cm^{-1} can be assigned to α-helix, admittedly they are not separable from the irregular random coil state. Band positions along with the proposed assignments are shown in Table 2.1.

Wave number (cm^{-1})	Assignment
1615-1643	Extended chain/β-sheet
1647-1654	Disordered
1650-1660	α- Helix
1663-1695	Turns
1692-1697	β-sheet

Table 2.1. Characteristic frequencies for protein/peptide secondary structure assignment to amide I region.

Figure 2.6 shows the PM-IRRAS spectra of peptidolipid C_{18}-Aβ(25-35) Langmuir monolayer at the air-water interface at different surface pressures between 0 and 35 mN m^{-1} at an incident angle of 59°. A comparison of the PM-IRRAS for the compression and decompression can be found below in Figure 2.7.

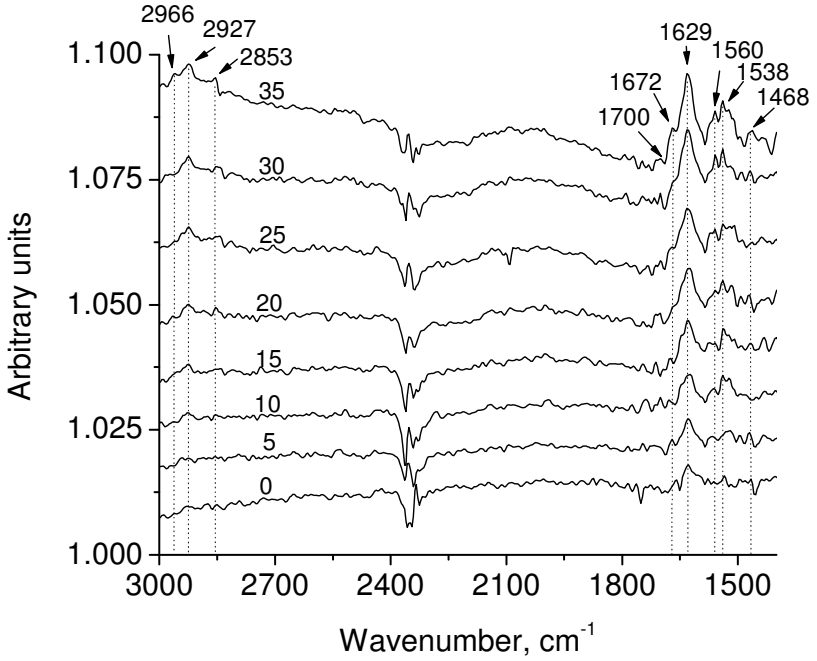

Figure 2.6. PM-IRRAS spectra of peptidolipid C_{18}-Aβ(25-35) Langmuir monolayer collected at the air-water interface at surface pressures from 0 to 35 mN·m^{-1}. The angle of the incident beam to the optical axis is 59°.

The region 3000-2800 cm^{-1} covers the methylene symmetric 2853 cm^{-1} ($\nu_s CH_2$), 2927 cm^{-1} antisymmetric ($\nu_a CH_2$) and 2966 cm^{-1} terminal –CH_3 group stretching bands (a comparison of compression and decompression for this region of the spectrum may be found in the Supporting Information). Note that the intensity of the bands increases as surface pressures raise; since the corresponding transition moments are perpendicular to the alkyl chain, this intensity increase indicates a tilt of the aliphatic chains toward the normal to the air-water interface as the Langmuir monolayer is compressed, along with a greater density of molecules per unit area, as a result of the compression of the Langmuir monolayer. This is direct proof that at the air-water interface the aliphatic chain coupled to the peptide moiety does not hamper its functional activity for the reason that the chains orient themselves towards the air phase upon compression: see Figure 2.7 below.

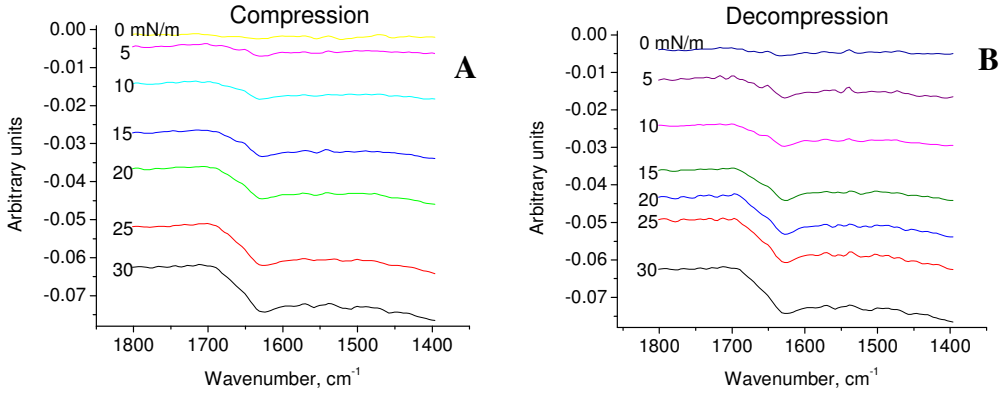

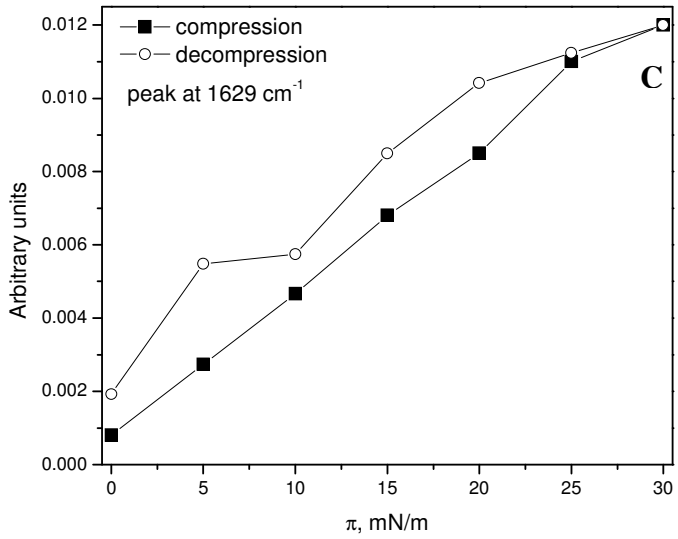

Figure 2.7. PM-IRRAS of the methylene region for C_{18}-Aβ(25-25) during (A) compression and (B) decompression; (C) signal intensity obtained by PM-IRRAS as function of surface pressure of compression and decompression of the Langmuir monolayer.

Secondly, the amide I region of the PM-IRRAS spectra 1600-1700 cm^{-1} of the peptidolipid reveals that higher surface pressures cause the absorption bands to increase, which is similar to the alkyl chains. The small band at 1700 cm^{-1} in Figure 2.6 corresponds to the –COOH group on Met35 position from Aβ(25-35). The absorption bands at 1629 and 1672 cm^{-1} are associated with the β-structures, parallel and disordered, respectively. Thus the aggregates formed by peptidolipid C_{18}-Aβ(25-35) in the plane of the air-water interface are composed of a mixture of disordered and β-sheet structures with a much larger amount of parallel β-sheet secondary structure. Between 1500 and 1600 cm^{-1} are the bands characteristic of the Amide II region but these bands are not as well defined as compared to the Amide I region. The aggregation that leads to domain

formation is confirmed by the PM-IRRAS measurements during the decompression of the Langmuir monolayer. During decompression, the amide I and II regions as well as the methylene region show higher intensities for the vibrations when measured at the same surface pressure. These results are in good agreement with the epifluorescence data during the compression and relaxation of the Langmuir film.

2.6 CD Spectroscopy of Langmuir-Blodgett films of amyloid peptide fragments

CD spectroscopy is a standard tool for determining conformation of proteins and polypeptides in aqueous solution.[26] It has also been shown that the films of adsorbed proteins and polyamino acids can give reproducible CD spectra which may be interpreted in terms of standard conformations.[27,28] However, one complication brought about by this methodology is the amount of material required in a film to produce a suitable signal. In the present study, 15 layers were deposited to prepare the peptidolipid C_{18}-Aβ(25-35) LB film onto the quartz support to ensure the signal collected by CD spectrometer would be strong enough for analysis. The deposition surface pressure to prepare the LB film was set at 25 $mN \cdot m^{-1}$. The rationale for choosing this value is that the formation of domains was observed by epifluorescence spectroscopy at this surface pressure. A Y-type deposition with a transfer ratio of 0.8 was observed. The CD spectrum, Figure 2.8, shows a single negative maximum at about 219 nm, accompanied by an intense positive maximum at 192 nm and a crossover point at 210 nm.

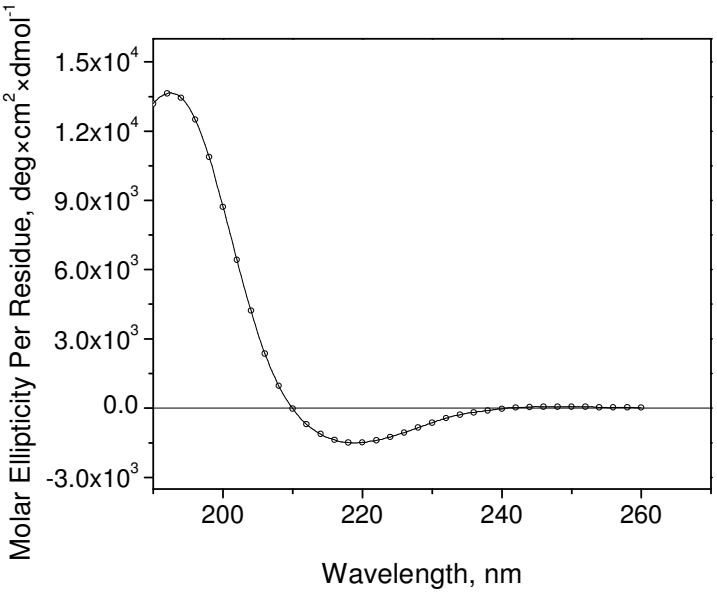

Figure 2.8. CD spectrum of peptidolipid C_{18}-Aβ(25-35) Langmuir-Blodgett film (15 layers) deposited at surface pressure of 25 $mN \cdot m^{-1}$.

Due to the nature of the LB film, it is not possible to quantitatively determine the secondary structure using programs such as SELCON3 and CONTIN, however, we can qualitatively identify the conformation of the peptidolipid LB film from the CD spectrum. In general, the characteristic CD bands of helical structure show negative double minima at 208 and 222 nm with a crossover point at around 198-201 nm,[29,30] while β-structure displays an intense negative band around 216-220 nm and a maximum at 192-197 nm with a crossover point at 204-207 nm. In the present case, the peptidolipid C_{18}-Aβ(25-35) LB film takes a conformation characteristic of a β-sheet that is typical of amyloid protofibrils, as observed in other proteins and peptides.[31] These results agree

with the data obtained from PM-IRRAS measurements indicating the presence of β-sheet secondary structure.

2.7 Conclusion

This study applied the 2D approach to the investigation of Aβ(25-35), while the Leblanc group has previously applied this method to shorter amyloidogenic peptide fragments, namely Aβ(31-35) (C_{18}-IIGLM) in both the carboxylic acid, and amide forms[23], the approach is added upon and used to compare the results of peptide fragments of varying lengths. Results from epifluorescence imaging along with PM-IRRAS and CD show that there is a gradual aggregation of Aβ(25-35) upon compression at the air-water interface although the aggregates are not visible until a surface pressure of about 20 mN m^{-1}, and that the peptidolipid, upon aggregation, takes a conformation characteristic of β-sheet structure typical of amyloid protofibrils, confirmed by both CD measurements of the LB films, and *in situ* PM-IRRAS of the Langmuir monolayer. The aggregates formed are stable upon multiple compression-decompression cycles as can be seen from the hysteresis. This indicates that the polar moieties of the peptidolipid do interact strongly, and that this interaction is stronger than that between the polar moieties and the subphase. While at low surface pressures, in the LE phase, the peptidolipid molecules are not in close proximity: there is minimal interaction between the peptide moieties resulting in a low degree of aggregation. When higher surface pressures are reached (LC phase), the peptidolipids are better packed and contact between the peptide moieties and consequently their side chains occurs. Under these conditions aggregates gradually form as can be seen from the epifluorescence micrographs, although this is not apparent until a

surface pressure of about 20 mN m^{-1} is reached. It is important to note that the surface pressure-area isotherm contains multiple kink points indicating the various phases the Langmuir monolayer undertakes upon organization as described above. From PM-IRRAS, it can be observed that even at low surface pressures there is a small component of β-sheet secondary structure, however, between 15 and 20 mN m^{-1} there is a rather large increase in the β-sheet content of the film that occurs upon entering into the liquid condensed phase, and subsequently from 20 all the way to 35 mN m^{-1}, every 5 mN m^{-1}, we see an even larger increase as compared to the increase at low surface pressures (below 20 mN m^{-1}). The β-sheet structure is stabilized by hydrogen bonding between amino acid side chains, and the vast majority of the aggregation appears with the onset of the liquid condensed phase, implying that in this state the Langmuir monolayer maximizes the interaction between side chains.

When comparing the two forms of C_{18}-Aβ(31-35) previously studied, the amide terminated peptidolipid more readily aggregates than the carboxylic acid peptidolipid. This is explained by the fact that the peptidolipid amide has a larger dipole moment than the peptidolipid carboxylic acid, and this implies larger dipole-dipole interactions between the hydrophilic moieties of the amide compared to the carboxylic acid upon compression. When comparing C_{18}-Aβ(25-35) to C_{18}-Aβ(31-35) it is seen that both the shorter peptidolipid fragments aggregate more readily than the larger peptidolipid Aβ(25-35); aggregation from epifluorescence imaging is easily visible for the Aβ(31-35) amide at surface pressures as low as 5 mN·m^{-1}, while for the C_{18}-Aβ(31-35) carboxylic acid this is not easily visible until a surface pressure of 10 mN·m^{-1}, and for C_{18}-Aβ(25-35) the aggregation is not readily visible until surface pressures of 20 mN·m^{-1} or greater. The

difference in surface pressure between the aggregation of the amide and carboxylic acid has been explained above. For the larger C_{18}-Aβ(25-35) the aggregation process does readily occur, however, the additional length of the peptidolipid chain slows this process. It has been shown previously that the minimum fragment necessary to observe amyloid like fibril formation is C_{18}-Aβ(31-35) or a linear amino acid sequence of IIGLM, indeed, in light of these studies, not only is it the minimum sequence necessary, but it is also one of the most efficient at inducing aggregation and fibril formation. While larger peptidolipids containing this sequence will aggregate, the core sequence of IIGLM most actively promotes the formation of aggregates and fibrils.

To conclude, this study indicates that the 2D model system is appropriate for investigating the aggregation process of the peptidolipid C_{18}-Aβ(25-35), and that these short peptide fragments are indeed useful for studying the aggregation properties of proteins as will be expanded upon in the subsequent chapter. This process can be monitored by real time epifluorescence microscopy, while PM-IRRAS allowes *in situ* investigation of the conformation of the Langmuir monolayer. CD measurements afforded supplementary information on the structure of the domains deposited as LB films. Further study of larger fragments and the full length peptidolipid Aβ(1-42) by the 2D approach is needed in order to further elucidate the mechanism of aggregation.

Chapter 3. Photoablation of amyloid-like peptide aggregates

3.1 Background

It was shown in the previous chapter that peptidolipids based on short peptide fragments of the larger β-amyloid protein are viable for the formation of protein based aggregates. Information about the aggregation process was determined, however, the aim of trying to disrupt the aggregation was not addressed. In this chapter, short peptides based on the peptidolipids of chapter 2 are studied with the aim of determining a method and mechanism for the destruction of the aggregated structures.

The neuritic plaques[32] composed of β-amyloid (Aβ) peptide in the brain of Alzheimer's Disease (AD) patients, the most common cause of senile dementia[33], is primarily composed of Aβ(1-42) and to a lesser extent Aβ(1-40). These peptides are used as the hallmark indicators of AD[34-36]. Extracellular plaques are composed of fibrillar structures, tens of nanometers in diameter and up to a micron in length, of individual Aβ peptides interwoven in their aggregated β-sheet state[37]. While the Aβ hypothesis is not universally accepted as the sole cause of the physiological conditions associated with AD, it is widely implicated as playing a key role in the pathogenesis of the disease. Aβ may be found in a soluble conformation in both the blood and brain of healthy and diseased individuals alike. However, in the case of AD patients a large amount of aggregated Aβ, primarily exhibiting β-sheet secondary structure, can be found in this neurotoxic form that leads to AD. The conformational changes of Aβ(1-40) and Aβ(1-42) promote self-assembly of the peptide molecules. Aβ has been found to aggregate

through a pathway involving interstrand hydrogen bonding that leads to fibrils having axes perpendicular to the β-strand and parallel to the cross-linking hydrogen bonds[37]. While the understanding of Aβ aggregation has advanced steadily, currently there are only a handful of known compounds capable of disrupting aggregation; namely, small organic molecules and peptide breakers[38-42].

Colloidal gold has been used for decades in a biological role[43] as a staining and contrast reagent. Gold is well suited for these biological applications as it is non-toxic, and easily visible using microscopic and spectroscopic techniques as a result of its density and optical properties, respectively. Gold nanoparticles in the range of a few to tens of nanometers exhibit a strong surface plasmon resonance band around 520 nm[44,45]. This surface plasmon resonance (SPR) is a result of the coherent oscillation of nearly free conduction electrons[46]. The extinction coefficient of gold nanoparticles is orders of magnitude higher than typical organic dye molecules. The utility of this interesting optical phenomenon arises upon the relaxation of the excited SPR; the Au nanoparticle will relax non-radiatively via a photothermal mechanism in which the hot electron gas will thermally equilibrate with the Au nanoparticle lattice followed by release of heat to the surroundings[47-51]. This process most commonly occurs on a picosecond time scale that results in a rapid increase in local temperature. While this phenomenon has been understood for some time varied applications[52,53] have been limited, however, notable work has been recently accomplished in the area of tumor ablation[54-56].

In the current work, photothermal ablation of peptide aggregates induced by gold nanoparticles is studied. While some microwave based methods[57-59] require magnetic assistance, this laser based system does not. There is also the potential of tuning the

system to use less harmful and deeper penetrating irradiation such as the near IR absorption of gold nanorods[60-64]. One of the largest problems with using nanoparticles for biological roles is in controlling the number of functional moieties attached to the nanoparticle surface and their location of attachment. This limitation has been overcome by using a previously reported solid phase synthesis strategy[60-64]: gold nanoparticles were prepared with a single or minimum number of carboxyl groups attached to the surface and a protecting layer of thiolated triethyleneglycol ligands for the present study.

The triethyleneglycol protecting layer imparts the nanoparticles with biocompatiblility by preventing nonspecific peptide or protein adsorption onto the surface of the particles. Analogues of physiological Aβ were synthesized and conjugated to the monofunctionalized gold nanoparticles (AuNP) by covalent modification through amide bond formation and verified using X-ray photoelectron spectroscopy (XPS). The Aβ monofunctionalized gold nanoparticle (AuNP-Aβ) conjugates were then mixed with amyloid peptide fragments and allowed to aggregate. Spectroscopic-- Circular Dichcroism (CD) and Bio-Attenuated Total Reflectance Fourier Transform Infrared spectroscopy (Bio-ATR-FTIR)-- and microscopic—epifluorescence microscopy, Transmission Electron Microscopy (TEM), Scanning Electron Microscopy (SEM), and Atomic Force Microscopy (AFM)—investigation provided confirmation of photothermal ablative damage, and in some cases, complete destruction of the aggregated peptide in the immediate area of irradiation, was clearly observed in this study.

3.2 Synthesis of peptide 'monofunctionalized' gold nanoparticles

Gold nanoparticles or colloids used for most biological studies are citrate-based gold nanoparticles. These nanoparticles are stabilized by a citrate ligand layer through electrostatic interactions. For this reason, the nanoparticles are not very stable and also very prone to nonspecific adsorption of proteins and other biomolecules. In this study, gold nanoparticles with a triethyleneglycol thiol ligand protecting layer were synthesized. It has been demonstrated that oligo(ethylene glycol) ligands are most effective at preventing nonspecific binding of peptides, proteins and enzymes to the nanoparticles. Also different from other existing nanoparticles, the gold nanoparticles used herein contain a single or a few limited carboxyl functional groups on the surface. This feature allows for controlled conjugation of peptides to the nanoparticles and avoids peptide-peptide interactions and aggregation within the same nanoparticle. Both TEM (Figure 3.1 A) and AFM (Figures 3.1 B) studies confirmed that the average size of the EG_3Au nanoparticles is approximately 5 nm with a relatively narrow size dispersity of around 10%. Figure 3.1 C presents the surface plasmon resonance band of the EG_3 AuNPs obtained by UV-Vis spectroscopy; the SPR band can be seen at 520 nm, which is characteristic of gold nanoparticles with diameters larger than 2 nm.

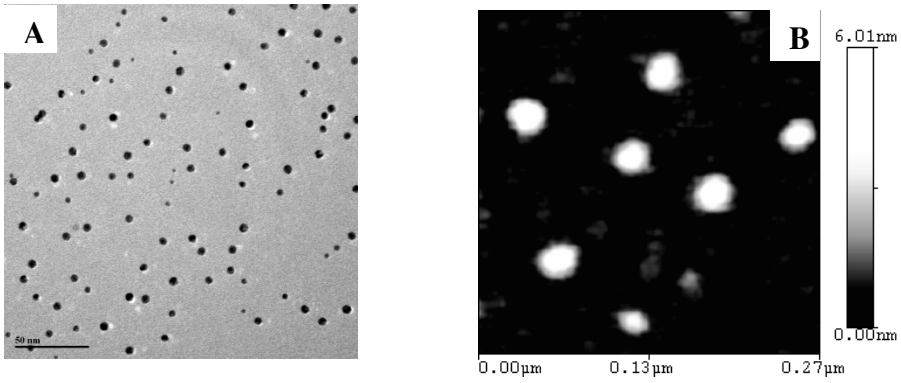

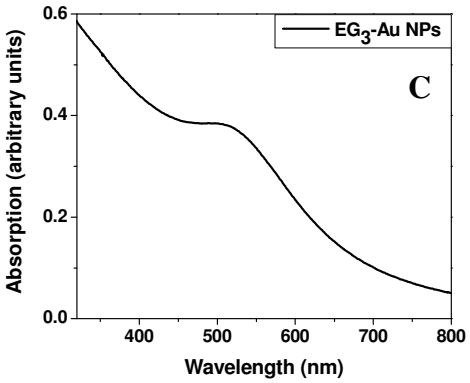

Figure 3.1. (A) TEM image of EG_3Au NPs; (B) AFM image of EG_3Au NPs (270 × 270 nm area); (C) UV-Vis absorption spectrum of EG_3Au NPs in dichloromethane, path length 1 cm.

While Aβ(1-40) and Aβ(1-42) are the physiologically relevant peptides, various analogues consisting of truncated versions of the full length Aβ peptides have been studied as models, including Aβ(31-35), Aβ(25-35), Aβ(10-35), and Aβ(12-28). For the purpose of this study Aβ(31-35) was selected as the model peptide for peptide aggregation studies because it contains the shortest linear combination of amino acids that will aggregate and remain neurotoxic, while Aβ(25-35) was synthesized as a result of the difficulty in obtaining accurate quantitative secondary structural information via circular dichroism spectroscopy for the shorter Aβ(31-35) peptide. These two types of peptides were coupled to monocarboxylic EG_3Au nanoparticles through a one-step *in situ* amide coupling reaction and the conjugated product was separated from uncounjugated peptides by gel permeation chromatograph. A schematic representation of the AuNP

complex can be found below in Figure 3.2. The single free carboxyl group is the site for attachment of the peptides.

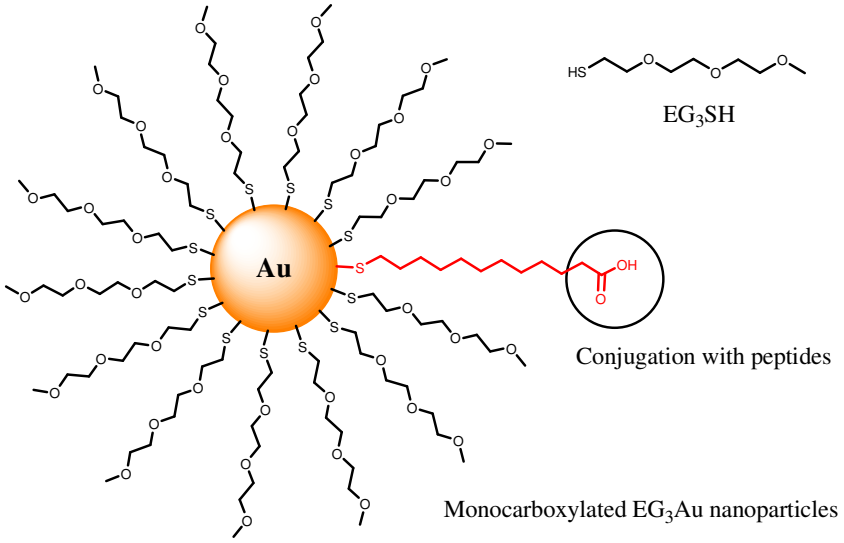

Figure 3.2. The chemical structure of EG_3SH ligand and monocarboxyl EG_3Au nanoparticle.

3.3. Characterization of peptide 'monofunctionalized' gold nanoparticles

In order to confirm that the AuNPs were indeed monofunctionalized an ethyldiamine coupling reaction was performed on the as prepared monofunctionalized AuNPs. This reagent causes conjugation of free carboxyl groups. The resulting solution was analyzed by TEM in order to determine how many AuNPs were indeed monofunctionalized; those that were monofunctionalized should form dimers, while any AuNPs with higher degrees of functionalization should result in the formation of AuNP trimers or higher order oligomers. The results of this experiment can be found below in Figure 3.3.

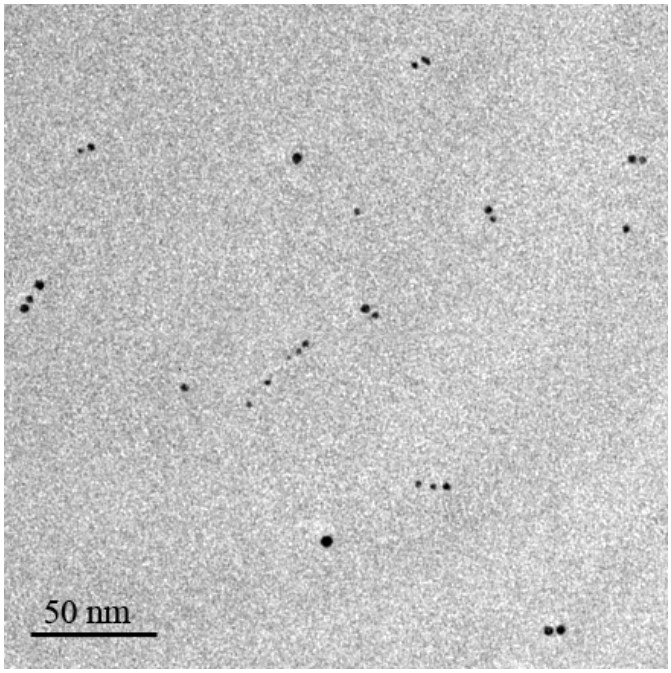

Figure 3.3. TEM image of monofunctional EG_3-Au NPs after ethyldiamine coupling

As can be seen, the majority of the AuNPs appear as dimers, however, monomers and trimers are observed. This would indicate that the monofunctionalization does occur, however, the reaction does not solely yield monofunctionalization particles: for this reason these AuNPs will be referred to as 'minimally functionalized' for the sake of accuracy.

Additional experiments were performed in order to verify the coupling of the peptides with the gold nanoparticles and this was confirmed by X-ray photoelectron spectroscopy (XPS) analysis. The initial EG_3Au nanoparticles contain no nitrogen. After coupling of the peptides, the nitrogen element should appear from XPS analysis. Indeed, XPS analysis detected a weak N 1S signal from the nanoparticle-peptide conjugates (Figure 3.4).

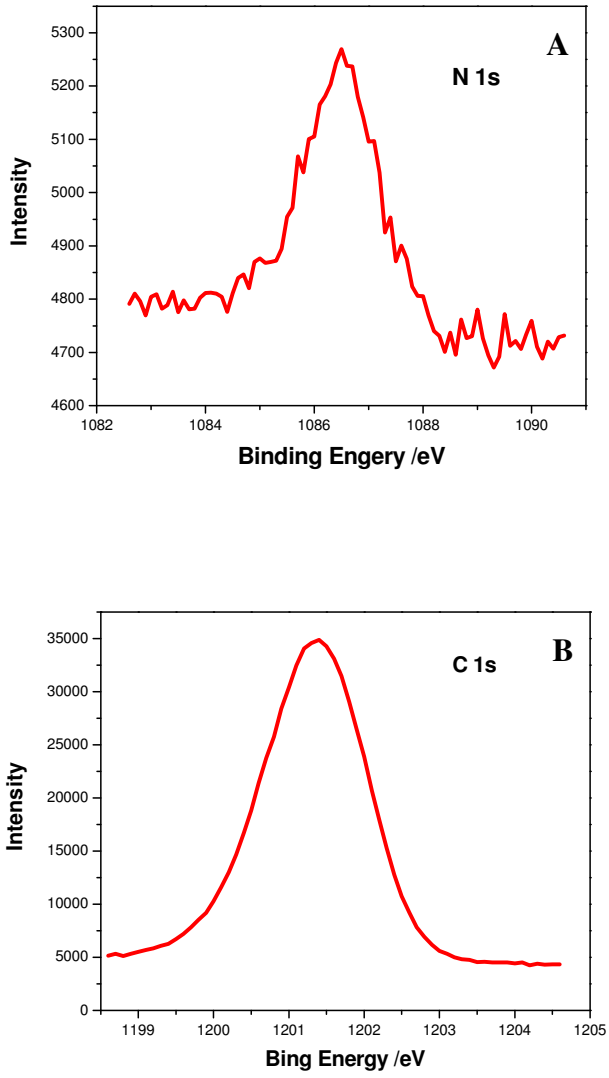

Figure 3.4: (A) XPS analysis of the peptide coupling to the AuNPs showing the N 1s and (B) the C 1s signals.

The detected N signal was not from the peptides that are not coupled to gold nanoparticles. After coupling peptides with EG_3Au nanoparticles, size exclusion chromatography was used to purify the nanoparticle-peptide conjugates. Using a size

exclusion chromatography (LH-20 sephadex gel) with the exact same dimension and solvents, the peptides were eluted from the column in 9-10 minutes after addition of the peptides into the column (confirmed by Ninhydrin test), while the nanoparticle-peptide conjugates were eluted from the column in 4-5 minutes after the sample solution was loaded into the column. The peptides and nanoparticle-peptide conjugates were well separated into two fractions. This confirmed that the nanoparticle-peptide conjugate sample did not contain free peptides and the nitrogen signal detected by XPS from the conjugated nanoparticles must come from peptides covalently coupled to the nanoparticles.

3.4. Formation and characterization of peptide aggregates with incorporated gold nanoparticles for photothermal ablation

The purified AuNP-Aβ conjugates were tested for their ability to aggregate. Congo red was added to the conjugate solution as a fluorescent label. It was evident from the epifluorescence micrographs, as shown in Figure 3.5, that the conjugates (Figure 3.5 B) readily formed protein aggregates very similar in structure and dimension to those of the pure peptide (Figure 3.5A).

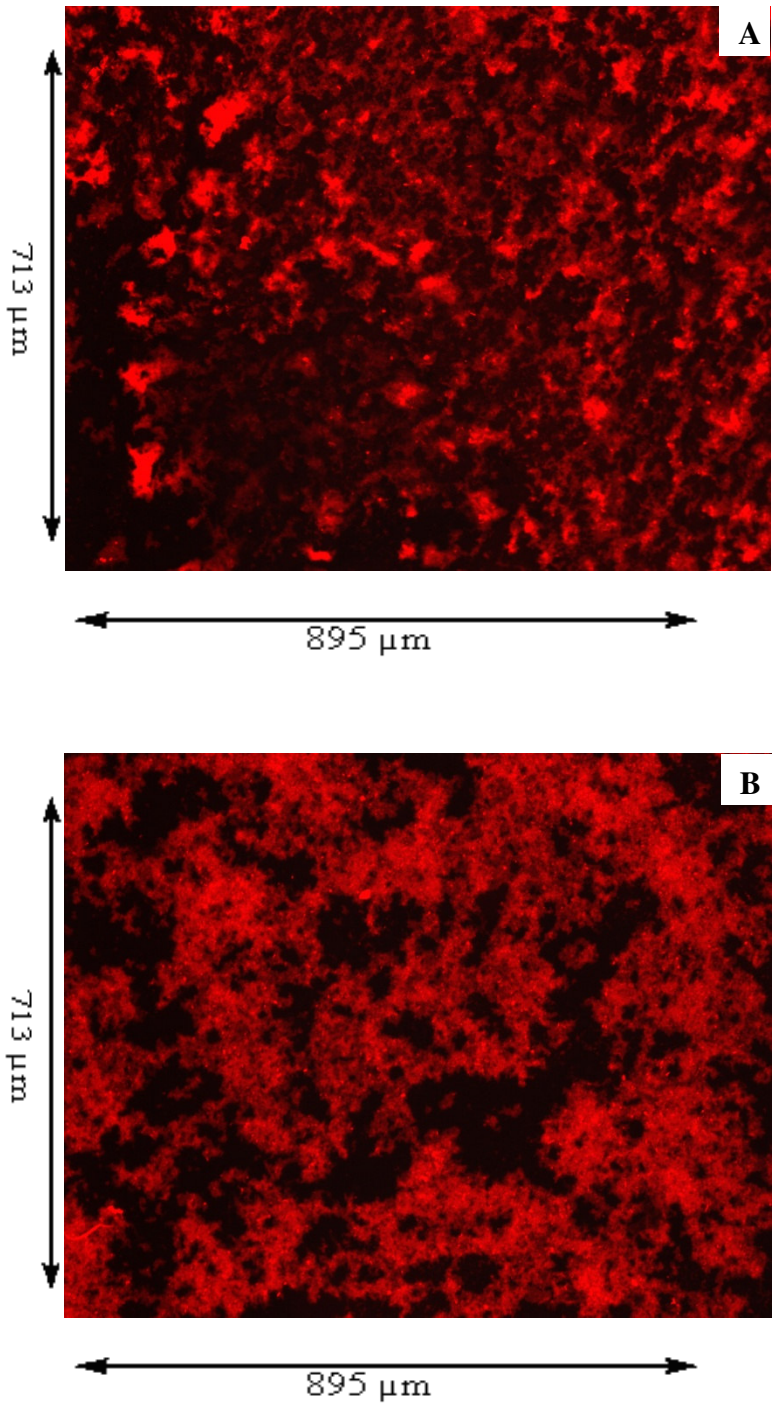

Figure 3.5: Epifluorescence micrograph of (A) Aβ(25-35) after Congo red staining, magnification 10x (B) AuNP-Aβ(25-35) conjugate after Congo red staining, magnification 10x.

When AuNP-Aβ(31-35 or 25-35) conjugates were mixed with pure Aβ(31-35 or 25-35) peptide in varying ratios, similar aggregates were observed after incubating the conjugates and peptides in solution for 24 h or longer. In control experiments involving EG_3 AuNPs (no peptide coupling) mixed with peptide, it was found that as the protein aggregates and precipitates out of solution the AuNPs remain in solution. Only after coupling peptide to the AuNP and then mixing with peptide will the AuNP interact with and become incorporated into the aggregates. EG_3 protected AuNPs without peptide coupling will not allow for photoablation to occur as these AuNPs will remain in solution and not become incorporated into the aggregates. An image of this experiment can be seen below in Figure 3.6.

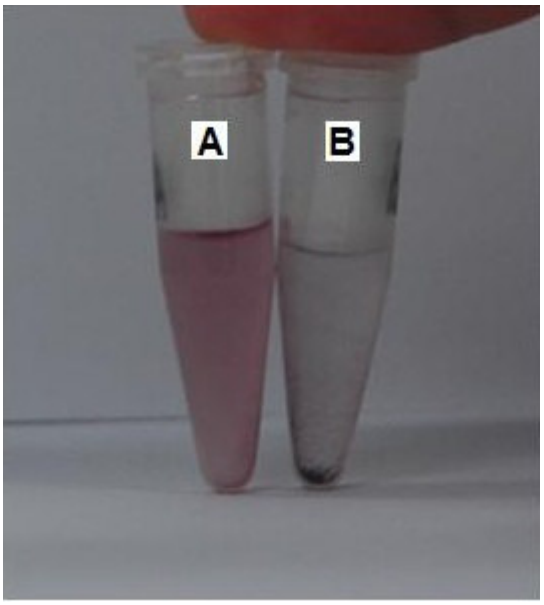

Figure 3.6: Control experiment (A) EG_3-Au NPs + Polypeptide in aqueous solution (B) EG_3-Au NPs/polypeptide conjugates + Polypeptide in aqueous solution.

Utilizing SEM, more details on the microstructure of the aggregates were revealed. As shown in Figure 3.7 A, the aggregates formed from pure Aβ(25-35) peptides are non-uniform in diameter and elongated in shape, with an average diameter of around 2 μm. The AuNP-Aβ(31-35) conjugate aggregate (Figure 3.7 B) is very similar in all regards except that it appears to have a much more uniform diameter and is slightly more globular in nature.

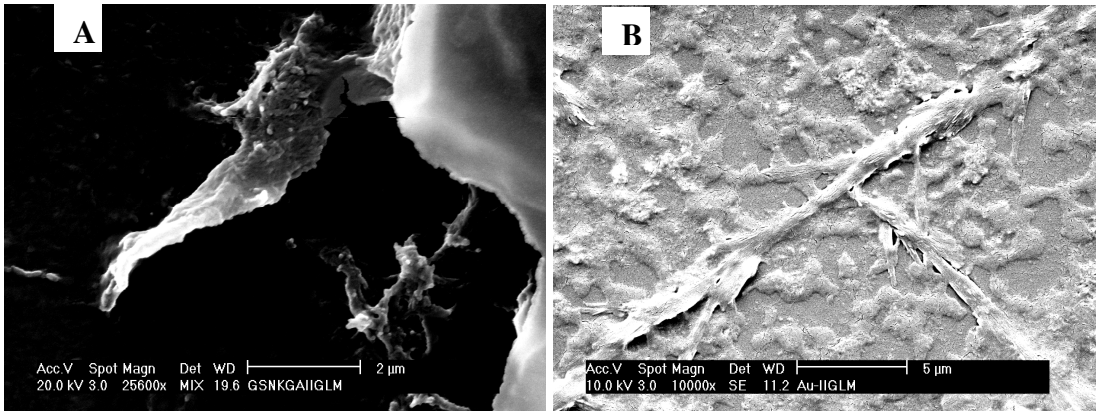

Figure 3.7. SEM micrograph of (A) Aβ(25-35), magnification 25,600x, scale bar 2 μm; (B) AuNP-Aβ(31-35) conjugate, magnification 10,000x, scale bar 5 μm.

The aggregates formed from pure peptides and peptide-nanoparticle conjugates were further analyzed and compared at the molecular level using Bio-ATR-FTIR. The amide A and amide B bands (Figure 3.8 A) arising from a Fermi resonance between the first overtone of the amide II and the N-H stretching vibration may be found at approximately 3500 and 3100 cm^{-1}, respectively. The amide I-- largely due to the carbonyl stretching vibration is directly related to the backbone conformation-- and

amide II-- resulting from the N-H bending and C-N stretching that are conformationally sensitive-- regions of the spectrum are seen in Figure 3.8 B. The assignment of relevant bands is as follows: the bands at 1625 and 1696 cm^{-1} may be assigned to the main component and secondary component of beta-sheet structure respectively, and the band at 1652 cm^{-1} corresponds to α-helical structure. In addition, the band at 1668 cm^{-1} is associated with a random coil, and the shoulder at 1680 cm^{-1} can be assigned to a β-turn structure. Standard secondary structure bands due to α-helical, β-sheet, and random coil conformations may be used to calculate the theoretical amide I spectrum as seen in Figure 3.8 C. The calculated spectrum based on the above mentioned conformations provided an excellent fit to the experimental data.

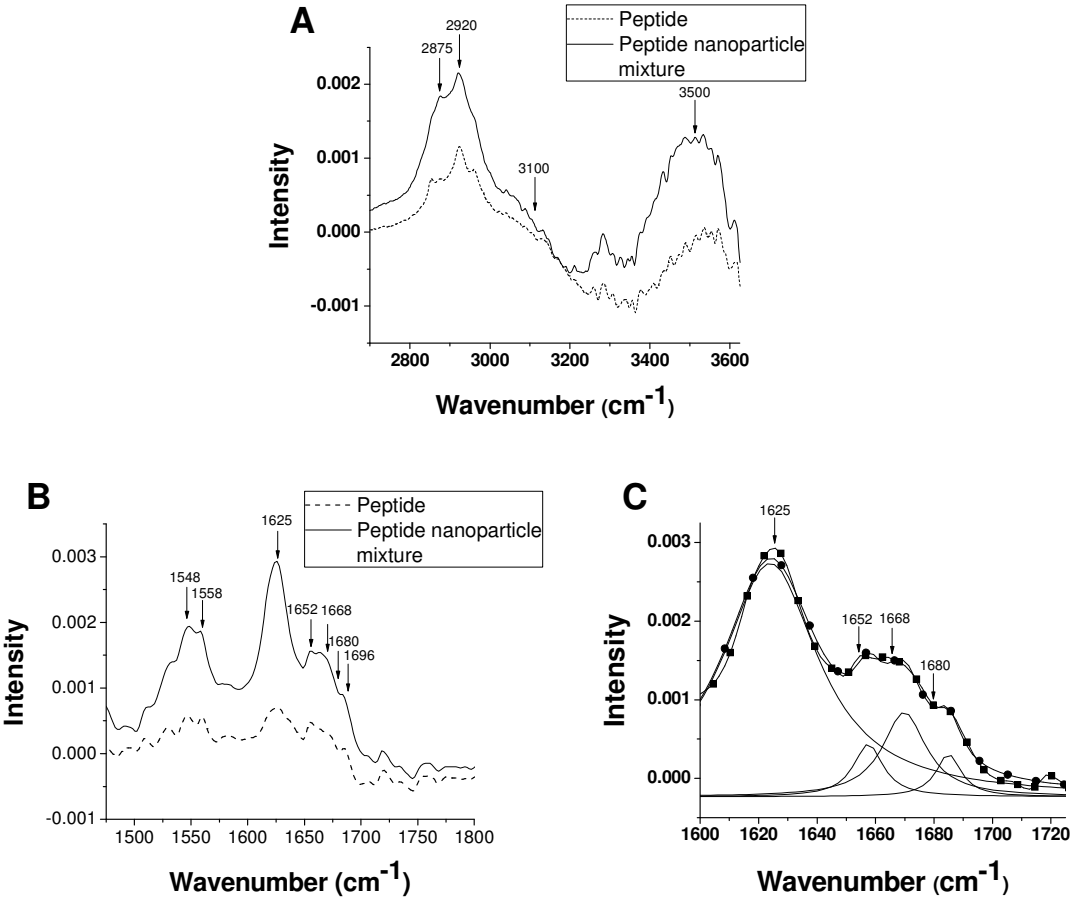

Figure 3.8. Bio-ATR-FTIR spectrum of (A) Amide A; (B) Amide I and II; (C) (-■-) the deconvolution of the spectrum as a result of secondary structure components (-) and the calculated spectrum due to the standard secondary structural components (-●-).

The FT-IR analysis clearly demonstrates that the expected secondary structural components found in Aβ(25-35) aggregates remain intact in the AuNP-Aβ(25-35) conjugate aggregates as their IR spectra are nearly identical within the observed range. One apparent difference is that the spectrum due to the conjugates is of much greater intensity than that of the pure peptide. This difference does not arise due to varying sample concentrations but rather is a result of the technique being used; the intensity of an ATR-FTIR spectrum is directly related to the amount of sample in immediate contact with the ATR crystal. The AuNP-Aβ(25-35) conjugate sample is likely much more dense than Aβ(25-35) as a result of the presence of AuNPs. This could allow for more conjugate peptide to be in contact with the ATR crystal.

CD spectroscopy was used to monitor the secondary structure of the peptide during aggregation over a 168 h period (every 24 h for the first 72 h, and then every 48 h thereafter). The results are summarized in Table 3.1 while the spectra may be found below in Figure 3.9. Pure Aβ(25-35) contained 28% β-sheet structure upon initially preparing the aqueous solution, and reached a maximum of 44% before settling around 42% after a 72 h period. The peptide was monitored for 168 h, however, little change was observed after 72 h. The increase in β-sheet structure is mainly at the expense of randomly structured segments of the peptide. AuNP-Aβ(25-35) conjugate mixed with

Aβ(25-35) (1:100, w/w) was monitored over the same time period. The percentage of secondary structure component did not deviate

Sample	***Hours***	***Alpha (%)***	***Beta (%)***	***Random (%)***
Aβ	*0*	*5*	*28*	*66*
Aβ	*24*	*9*	*36*	*55*
AuNP-Aβ	*24*	*7*	*38*	*55*
Aβ	*48*	*8*	*44*	*48*
AuNP-Aβ	*48*	*7*	*37*	*56*
Aβ	*72*	*8*	*42*	*50*
AuNP-Aβ	*72*	*7*	*39*	*53*

Table 3.1. Secondary structure composition from CD data of Aβ(25-35) and AuNP-Aβ(25-35) conjugates over a 72 h period as determined by k2d (http://www.embl-heidelberg.de/~andrade/k2d/).

from the pure Aβ(25-35) peptide by more than 7% for any structural component within the first 72 h of aggregation. Between 72 and 168 h there was less than 3% deviation. The relative changes of each secondary structure component directly correlated with those of the pure peptides over the time period studied. The CD spectra from which the data in Table 3.1 was made created can be found below in Figure 3.9.

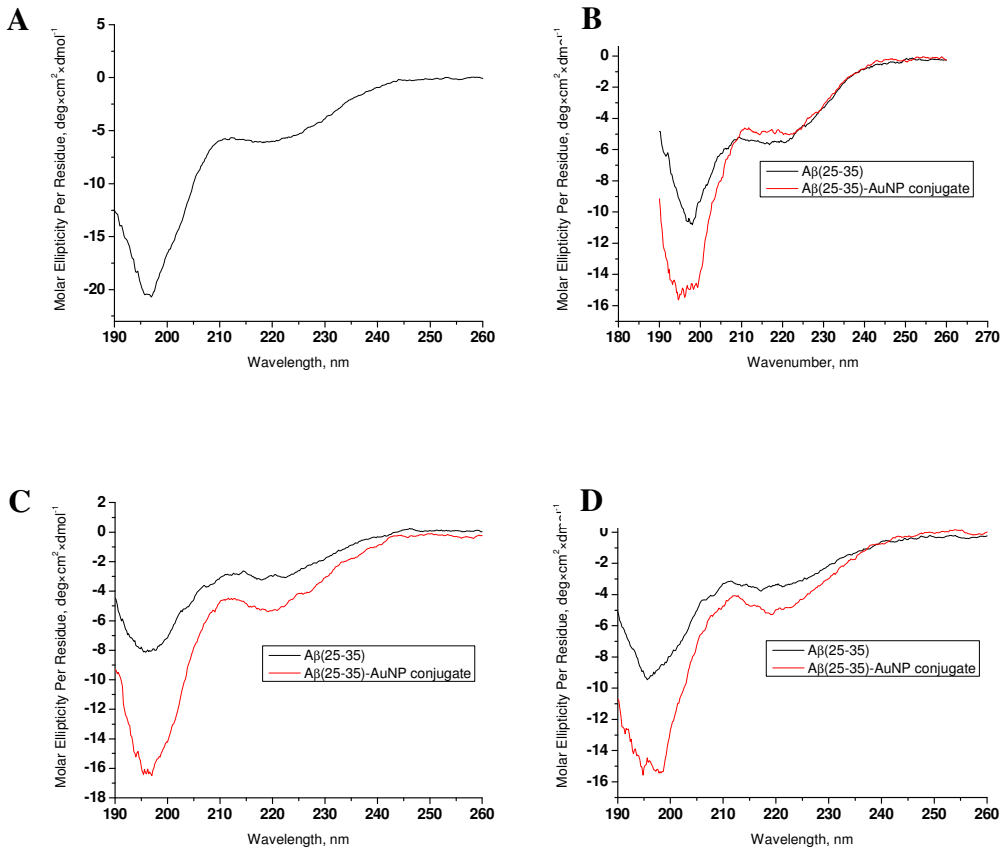

Figure 3.9. CD spectra for (-) Aβ(25-35) and (-) Aβ(25-35)-AuNP conjugates after (A) 0 h; (B) 24 h; (C) 48 h; and (D) 72 h.

3.5. Photothermal ablation studies of amyloid fragment monofunctionalized gold nanoparticles

Upon validating the aggregation formation by Aβ(31-35 and 25-35) and AuNP-Aβ(31-35 and 25-35) conjugates, photothermal ablation studies were conducted on the aggregates. Samples consisting of pure Aβ(31-35 or 25-35), AuNP-Aβ(31-35) conjugates, AuNP-Aβ(25-35) conjugates, and mixture of Aβ(25-35) with AuNP-Aβ(31-

35) or AuNP-Aβ(25-35) conjugates were irradiated with a continuous 532 nm laser (50 mW) for 5 min. For all samples, excluding pure Aβ(25-35), photothermal ablation of peptide aggregates was observed, however, to differing degrees. As a general trend, an increasing amount of ablation was observed with an increase in the ratio of AuNP-Aβ conjugate to Aβ peptide. The most effective sample was the AuNP-Aβ(31-35) pure conjugates. Shown in Figure 3.10 are the SEM micrographs of the irradiated AuNP-Aβ(31-35) conjugate sample. Samples were drop casted on a silicon substrate and the solvent (MeOH) was allowed to evaporate followed by 5 min of 532 nm laser irradiation. A uniform surface coverage of aggregates is observed in Figure 3.10 A interrupted by a crater structure in the middle of the micrograph. This crater is a result of photothermal ablation of Aβ aggregation. Figure 3.10 B is a magnified (1600x) micrograph of the ridge area around the crater. It is believed that this ridge structure is a result of a 45˚ irradiation angle with respect to the substrate surface normal. It is clear from Figure 3.10 B that the area irradiated has been cleared of Aβ peptide aggregates when compared to the area just above the ridge. Another magnified view (27000x) of the center of the

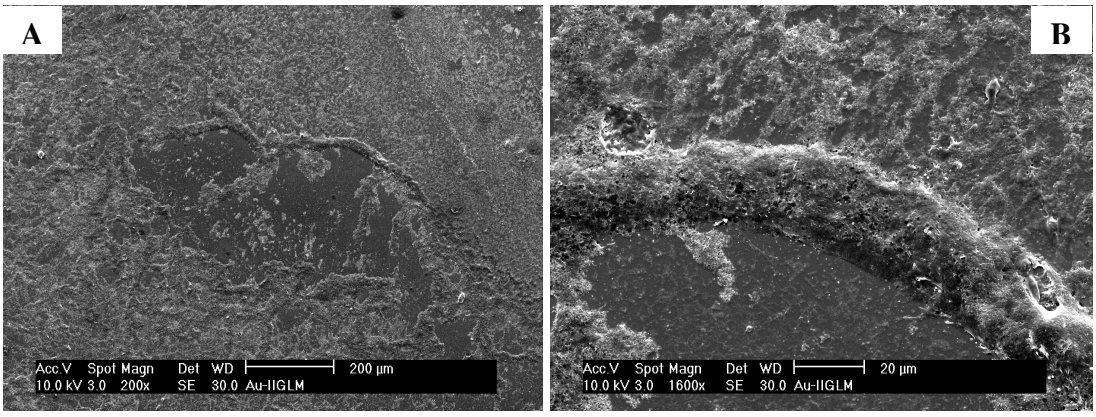

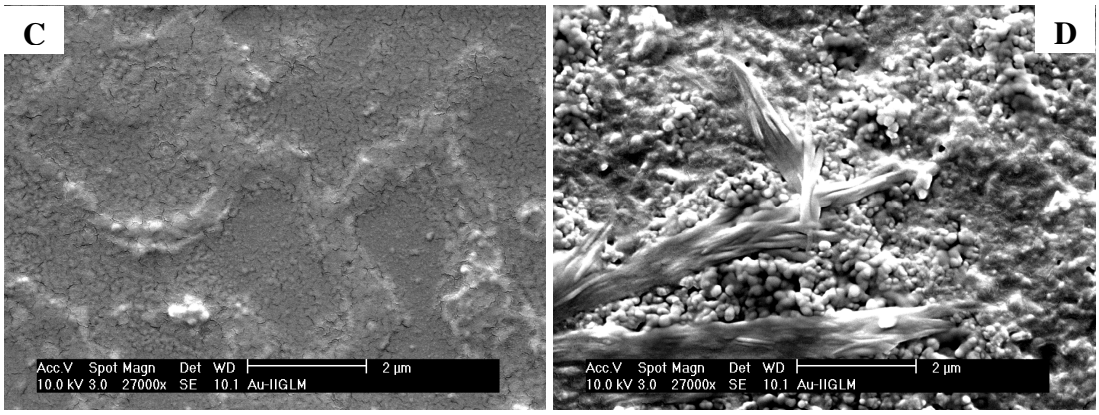

Figure 3.10. SEM micrograph of AuNP-Aβ(31-35) after laser irradiation. (A) Site of laser irradiation, magnification 200x, scale bar 200 µm; (B) Magnification of irradiation site, magnification 1600x, scale bar 20 µm; (C) Area of direct laser irradiation, magnification 27000x, scale bar 2 µm; (D) Area just outside laser irradiation, magnification 27000x, scale bar 2 µm. Not presented: Control experiments involving 5 min laser irradiation of pure peptide samples resulted in no visual ablation to the aggregated peptide surface.

crater (Figure 3.10 C) further confirmed this finding. In contrast, a magnified view (27000x) of the non-irradiated area above the ridge as shown in Figure 3.10 D reveals that the aggregates remained intact with only minimal damage due to thermal diffusion from the site of irradiation.

It is worth briefly discussing a control experiment in which EG_3 AuNPs (no peptide coupling) were mixed with Aβ peptide and allowed to aggregate. As the peptide aggregates it precipitates out of solution and when the AuNP is conjugated to peptide, it is incorporated into this precipitating aggregate. However, when there is no peptide

coupled to the AuNP as in this case, the AuNPs do not precipitate out with the aggregates but rather stay in solution (Figure 3.6 above). In this case photoablation of the aggregates would not occur as the AuNPs are not incorporated into the aggregates. This system is only effective towards photoablation when the AuNPs are coupled to a minimal number of peptides.

TEM microscopy was also used to investigate the ablative potential of the gold nanoparticles on aggregated peptide. Figures 3.11 A and 3.11 B present TEM micrographs of AuNP-Aβ(31-35) conjugate samples prior to and after irradiation, respectively. While the copper grids being used for sample deposition had a larger diameter (3 mm) than the laser beam, the entire surface of the grid was illuminated as a result of the laser beam scattering on the surface. Before irradiation, a large amount of globular aggregates connected by fibrillar structures were clearly visible. After irradiation for 5 min drastically fewer globular aggregates were observed, while the fibrillar bridges all but disappeared as a result of photothermal ablation.

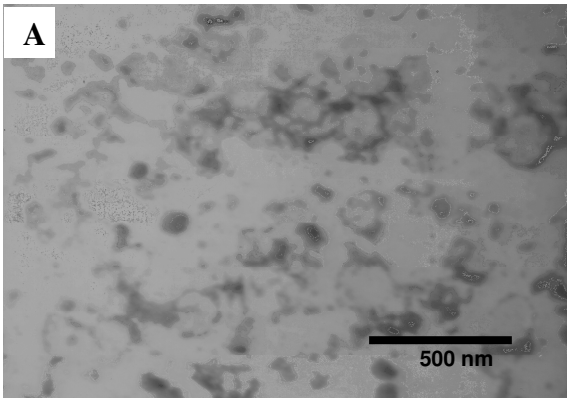

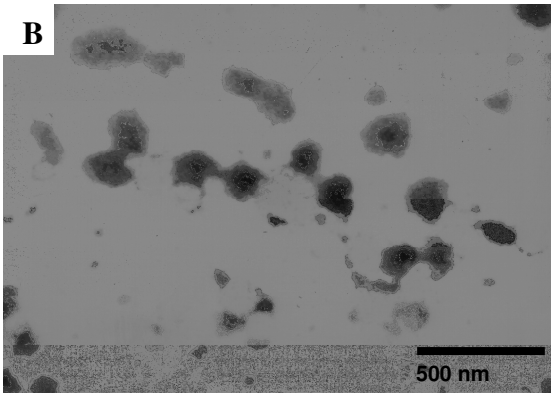

Figure 3.11. TEM micrographs, magnification 57000x, scale bar 500 nm, of (A) AuNP-Aβ(31-35) conjugates prior to and (B) after irradiation, magnification 47650, scale bar 500 nm.

The photothermal ablation of peptide aggregates was also studied by AFM on pure Aβ(31-35) peptide, and AuNP-Aβ(31-35) conjugates. Before laser irradiation, the characteristic aggregated structures were observed (Figure 3.12) from the pure Aβ(31-35) peptide. Many different localities of the sample were scanned, and it was found that the mica surface was uniformly covered by micro-globes and their aggregates. The small globes have diameters of 20-100 nm (Figure 3.13 B), and the film roughness is about 1.05 nm in RMS (Figure 3.13 C). Figure 3.13 A shows a close look at the hole structures. It is clear that there are small globes inside these holes consisting of aggregates. Figure 3.13 B is the phase image of Figure 3.13 A, providing the clearest view of these structures.

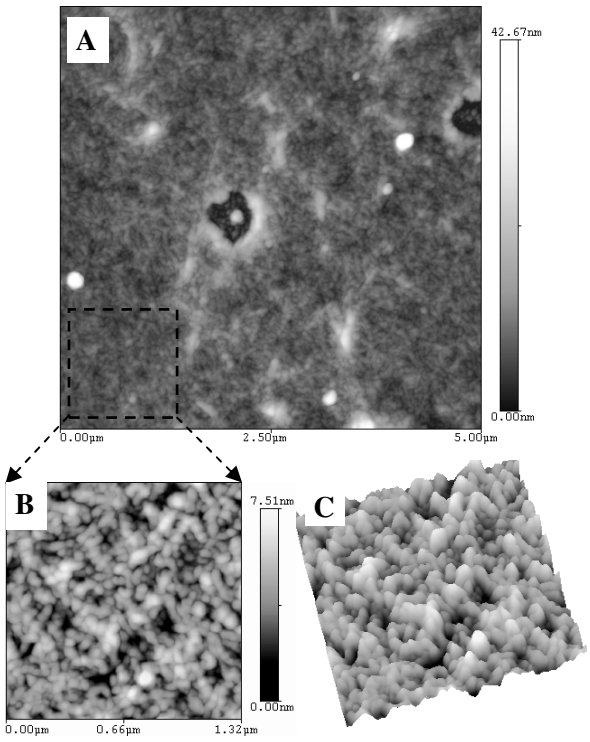

Figure 3.12. AFM micrograph of the typical topography of the pure Aβ(31-35) peptide sample: (A) 5 × 5 µm scan; (B) 1.32 × 1.32 µm; (C) 3D view of structure (B). The measured surface roughness of the structure in (B) is ~1.05 nm in RMS (not shown).

At least 10 different regions of the AuNP-Aβ(31-35) conjugates were scanned within the center of the sample (the site of irradiation), and it was found that the typical topography is different from the AuNP sample and the pure Aβ(31-35) (Figure 3.12) peptide sample. As shown in Figure 3.13, neither small globes (peptide in Figure 3.12) nor nanoparticles (Figure 3.1 B) were found. The surface is very smooth except for hole structures (Figure 3.13), which were also found on the pure Aβ(31-35) sample (Figure 3.12), however, they differ importantly.

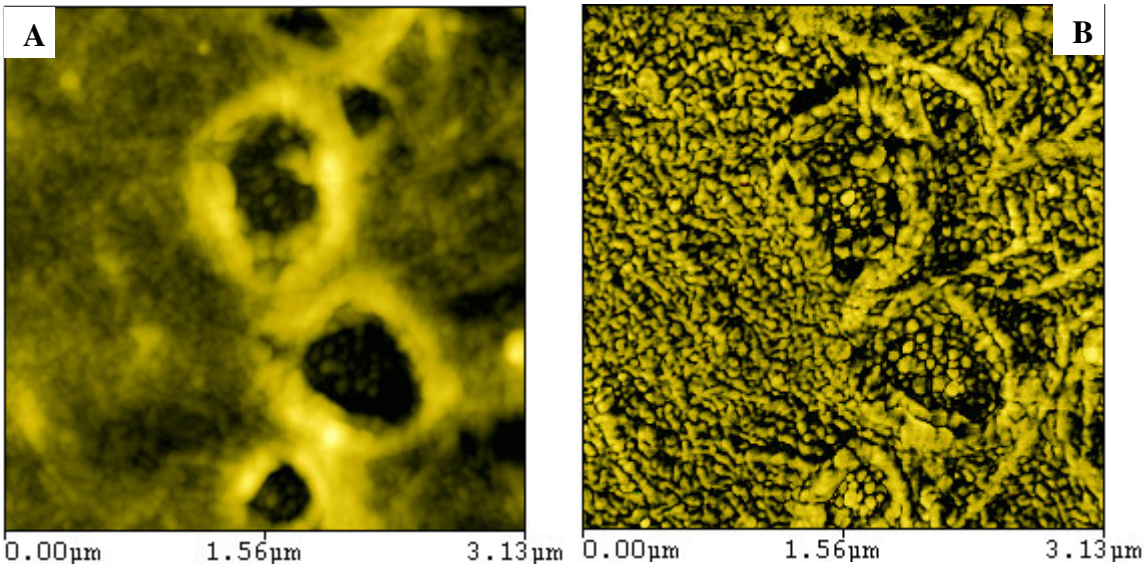

Figure 3.13. AFM micrograph of a close-look at the hole structures formed by Aβ(31-35) that are typical. (A) Topography; (B) Phase Image of the same structure.

Interestingly, the small globes inside the holes of Figure 3.12 were not visible in the AuNP-Aβ(31-35) sample (Figure 3.14 C). Figure 3.14 represents the most typical topography of the AuNP-Aβ(31-35) sample; no fiber-like structures were found. However, on the periphery of the mica substrate, outside the area of irradiation, micron-sized structures were occasionally found analogous to those imaged in the pure peptide sample (Figure 3.12). The phase image offers the most sensitive way to detect this filament. In the phase image of Figure 3.14 B which is the most typical topography, these fibers were not found in the entire 20 × 20 µm scanned area.

These results confirm that irradiation of the AuNP-Aβ conjugate samples results in photothermal ablation of Aβ aggregation as was also observed using epifluorescence

microscopy, TEM, and SEM, however, additional information is gained from the AFM experiments that was not observed using the other techniques.

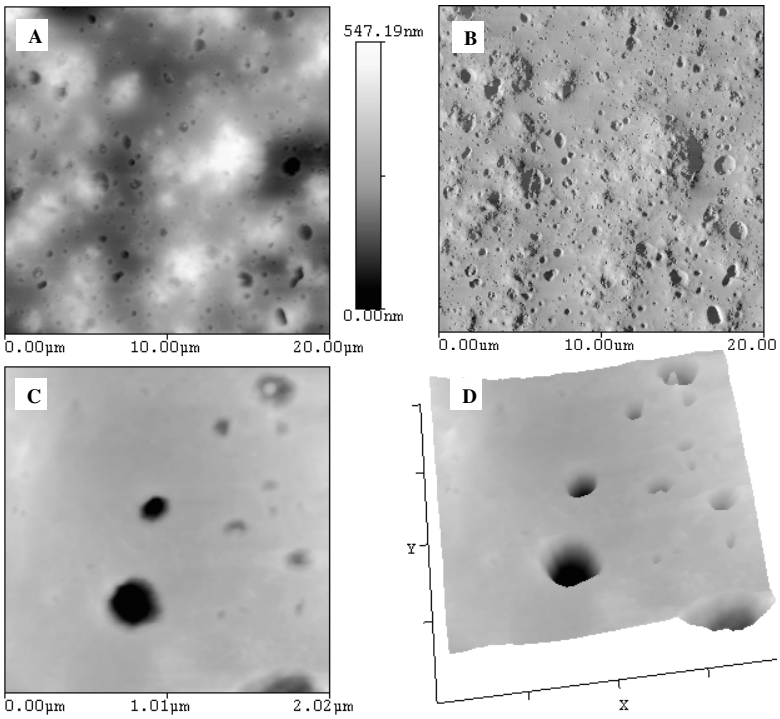

Figure 3.14. AFM micrograph of typical topography of the center of the AuNP-Aβ(31-35) sample (laser-irradiated Au-Peptide Complex). (A) 20 × 20 µm scan; (B) Phase image of the same area; (C) 2 × 2 µm scan with Z-height scale of 77.54 nm; (D) 3D view of the structure of C.

The topography of the pure Aβ(31-35) peptide samples is relatively rough and irregular while in the irradiated area of the AuNP-Aβ(31-35) conjugate sample the surface is uniformly smooth and regular with an occasional hole structure. It has been reported that long irradiation times (ranging from half an hour to several hours) may result in photothermal melting[66] or fragmentation of the AuNPs (this work involved a pulsed laser

as the source of irradiation). While the irradiation time in any one spot was not long for this sample, it was irradiated in six adjacent areas for 5 min intervals each. The heat produced by thermal diffusion could amplify the amount of heat being photothermally released at the next site of irradiation. While there is no conclusive evidence of melting or fragmentation, this possibility cannot be neglected.

3.6. Conclusion

Using Aβ monofunctionalized gold nanoparticles and continuous 532 nm laser irradiation it was shown that protein aggregates of Aβ can be photothermally ablated from surfaces using short irradiation times (5 min). However, mixing of AuNPs (no peptide functionalization) with peptide followed by irradiation does not lead to photothermal ablation indicating the importance of the peptide functionalization. Aggregation characteristics were investigated using Bio-ATR-FTIR and CD spectroscopies. Samples consisting of AuNP-Aβ conjugates mixed with Aβ peptide showed very little secondary structure deviation when compared to pure Aβ samples over the time of aggregation. Photothermal ablation was confirmed using low magnification and high magnification microscopic techniques of contrast microscopy, TEM, SEM, and AFM alike while the power of the system arises from the monofunctionalized nature of the nanoparticles. The ablation was highly localized to the site of irradiation with minimal damage due to thermal diffusion. Other amyloidogenic proteins, including the full length Aβ peptide, along with laser pulse width damage dependence from a pulsed

laser should be studied in order to optimize the ablation potential for in vitro investigation.

Chapter 4. Antibody-gold quantum dot-PAMAM dendrimer complex as an immunoglobulin immunoassay

4.1 Background

In the previous chapter the utility of gold nanoparticles was demonstrated. However, other nanostructures composed of gold with vastly differing physical and optical properties may also be used for analytical purposes. The synthesis of gold quantum dots has been recently reported while very few applications of their use in the literature exist. This chapter presents work with a complex composed of gold quantum dots for the detection of biologically relevant analytes.

During the past decade, fluorescence-based assays have become the premier choice for immunochemistry based in vitro diagnostic (IVD) tests and in vivo imaging assays. Fluorescent labels, i.e. fluorophores when compared to chromophores and radio chemistry labels have several advantages such as higher sensitivity, better dynamic range, and potential for easy multiplexing[67-70]. Of the fluorophores available, it is expected that semiconductor quantum dots (QDs) will become common replacements for traditional organic or organometallic fluorophores due to their optical characteristics including narrow bandwidth and size dependent, controllable emission spectra, high extinction coefficient, broad excitation, and most importantly, stability against photobleaching[71,72]. Due to all of the above characteristics, QDs allow for greater sensitivity when compared to organic fluorophores which in turn lowers the detection limit, leading in the near future to the ultimate goal of reaching reliable single cellular and single molecular diagnostics [73-79]. However, to ensure solubility and stability, a thin shell or capping layer is needed

and must be added through a separate chemical step in the synthesis of semiconductor-based quantum dots based on elements from periods III and V, such as CdSe. While various capping strategies have been used to minimize potential toxicity, the safe use of III-V element based semiconductors quantum dots in living systems is still questionable. Recently, small metallic water soluble gold quantum dots (AuQDs)[80,81] have been synthesized using poly(amidoamine) (PAMAM) dendrimers as capping ligands through a simple one step synthetic procedure. These AuQDs exhibit size dependent narrow emission, narrow excitation, and it is expected that they will provide excellent biocompatibility.

While gold has been used for decades in biological applications such as staining and contrast agents[82], the luminescent properties and applications of gold nanoclusters, which exibit quantum confinement, has not been thoroughly investigated and few references and applications of gold based QDs exist in the literature[83-85], although there is a large potential for AuQDs to replace, or more likely augment, semiconductor QDs. AuQDs synthesized with PAMAM dendrimer capping provide an easily modifiable system that is well suited for biological applications; the dendrimers may be covalently or electrostatically conjugated to DNA[86,87], RNA[88], carbohydrates[89], and proteins[90,91] as the end groups of the PAMAM dendrimer most typically consists of, (however are not limited to), hydroxyl or amine groups. PAMAM dendrimers have also proven to be excellent cell transfection agents[92-96]. The novel properties arising from such a well studied biologically inert material as gold, along with the biological compatibility, ability to penetrate cell membranes, and a plurality of conjugation strategies of the PAMAM

dendrimer provide the basis of a system that could lead to many life sciences applications, both in vitro and in vivo.

In this study, as a proof of concept of the use of gold quantum dots in construction of an immunoassay, a human IgG immunoassay has been formed with PAMAM encapsulated AuQDs electrostatically conjugated to goat derived anti-human IgG polyclonal antibody, as is schematically illustrated in Figure 4.1. As a complex of AuQD-PAMAM dendrimer is only electrostatically bonded to an antibody ligand it is necessary to test the assay selectivity against other antigens, and to establish the influence, if any, of non-specific protein binding on assay performance. In order to test assay selectivity and non-specific binding interference, the assay has been tested on samples of known concentrations of human IgG, and results compared with

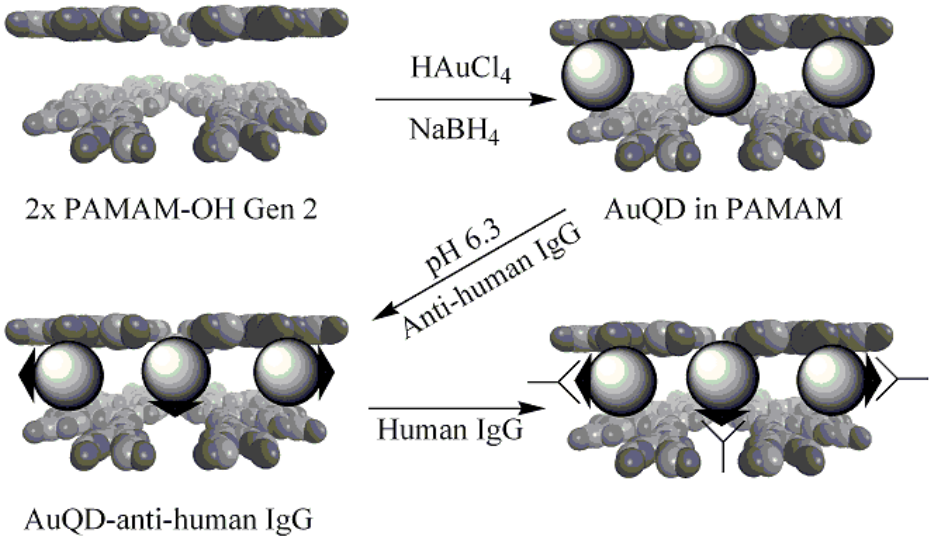

Figure 4.1. Schematic representation of PAMAM-OH generation 2 dendrimer, AuQD PAMAM complex, AuQD PAMAM- anti-human IgG (▲) complex, and formation of the quenching complex upon addition of the human IgG (Y).

the results obtained when tested with rabbit IgG, and the completely unrelated proteins, bovine serum albumin (BSA) and β-casein. Herein, it is demonstrated that the system provides a linear luminescence quenching response over a micromolar to nanomolar human IgG concentration range with little to no interference from BSA or β-casein, and slight interference from rabbit IgG, which is explainable in the terms of the anti-human IgG antibody specificity towards the unmodified bare AuQD surface.

4.2 Synthesis of PAMAM dendrimer stabilized gold quantum dots and surface conjugation for the formation of the antibody-gold quantum dot PAMAM dendrimer complex

Gold QDs with an emission maximum at 450 nm (λ_{exc} = 387 nm) were synthesized according to a method previously reported in the literature by Dickson *et al*[80,81]: in brief 0.5 μmol PAMAM G2-OH and 1.5 μmol $HAuCl_4 \cdot nH_2O$ were co-dissolved in 2 mL of distilled water (resistivity 18 MΩ·cm and surface tension of 72.6 mN/m at 20.0˚C, Continental Modulab 2020). The gold ions were sequestered within the dendrimer prior to the slow addition of an equivalent of the reductant $NaBH_4$ by allowing 30 min of stirring. The solution was stirred for 2 days so that reaction and aggregation processes could complete. Purification of the resulting solution was performed through ultracentrifugation at 16,000 g for 45 min in an L7 Ultracentrifuge resulting in size separation of the larger red fraction of Au nano and micro particles from the smaller AuQDs, leaving behind a transparent solution of AuQDs.

For the purpose of conjugating the AuQDs to anti-human IgG, the AuQDs were suspended in 2 mL phosphate buffer saline solution (PBS, pH 6.3) and mixed with 1 mg of polyclonal antibody specific to the human IgG (goat affinity purified antibody to human IgG). The antibody-dendrimer-AuQD complex was electrostatically conjugated at the above mentioned pH. The solution was then vortexed for 12 h. All of the work involving immuno-complexation of the antibody-QD complex with the recombinant human IgG antigen was performed in the presence of PBS buffer at a pH of 6.3. It was previously reported[81], as stated above, that AuQDs of varying sizes, and thus emission maxima, are able to be synthesized using this method. However, this finding was not able to be reproduced: only AuQDs with emission at 450 nm were succesfully synthesized.

4.3 Charaterization of PAMAM dendrimer stabilized gold quantum dots and the immunoglobulin complex formed

Characterization of the AuQDs was performed by a series of spectroscopic and microscopic techniques. It is worth noting that it has been experimentally shown that PAMAM dendrimers fluoresce[97], however, this fluorescence is only substantial at low pH levels[97]. All of the work presented here has been conducted at physiologically relevant pH ranges, in this particular case at a pH of 6.3, therefore, the luminescence observed results from the AuQDs and not the dendrimer: no luminescence at 450 nm in the absence of the AuQDs has been observed at the indicated pH. Spectroscopic characterization of the PAMAM dendrimer stabilized AuQDs revealed narrow excitation and emission maxima at 387 and 450 nm, respectively, (Figure 4.2 B) agreeing with the

results published in the literature[80,81]. Upon electrostatic coupling to goat-derived polyclonal anti-human IgG these maxima were unchanged.

Absorbance measurements revealed no Mie-scattering plasmon band, which for Au is at 520 nm (Figure 4.2A), indicating that the core AuQDs embedded within the dendrimer are smaller than 2 nm[98,99]. The main absorption band at 300 nm is a result of the antibody present in the complex[100]. It has been shown that AuQDs with the above mentioned optical properties are composed of only eight gold atoms[81], and that the only active fluorescence coming out of the complex is coming from the small fraction of particles.

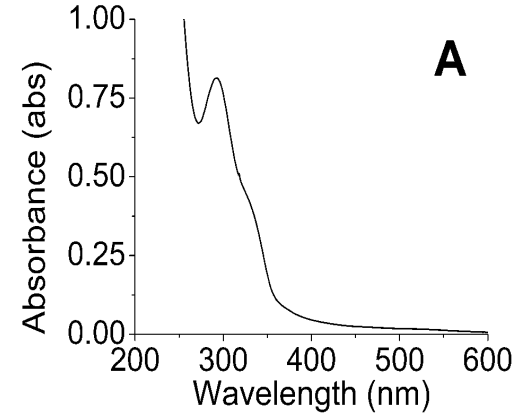

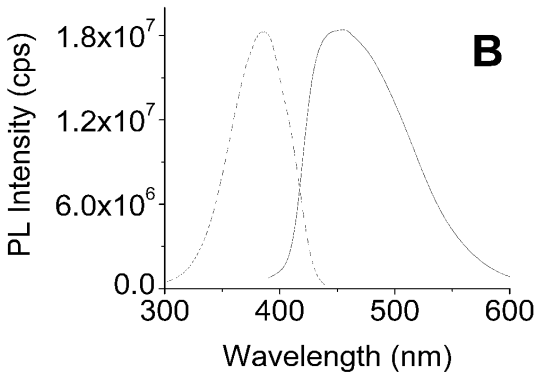

Figure 4.2. (A) Absorption spectrum of AuQD; (B) Excitation and emission spectra of AuQD in aqueous solution pH=6.3 (--) excitation and (-) emission.

While the core AuQDs are extremely small, the dendrimer capping enlarges the system by a few nanometers allowing for microscopic investigation; the second generation PAMAM dendrimer is approximately 2.9 nm in diameter[100]. The size and topography of the AuQD complex including the PAMAM dendrimer stabilizer were further investigated by high resolution transmission electron microscopy (HR-TEM) and atomic force microscopy (AFM). HR-TEM revealed an overall average complex size of 4.8 nm (sample size of 100)—this includes the core AuQDs and the second generation PAMAM dendrimer in which they are embedded. While the individual AuQDs are not visible as a result of their small size, the difference in contrast between the AuQDs and dendrimer due to vastly differing densities may be observed in Figure 4.3 A. The complex is spherical in shape with AuQDs found in various localities including the center and edges of the dendrimer.

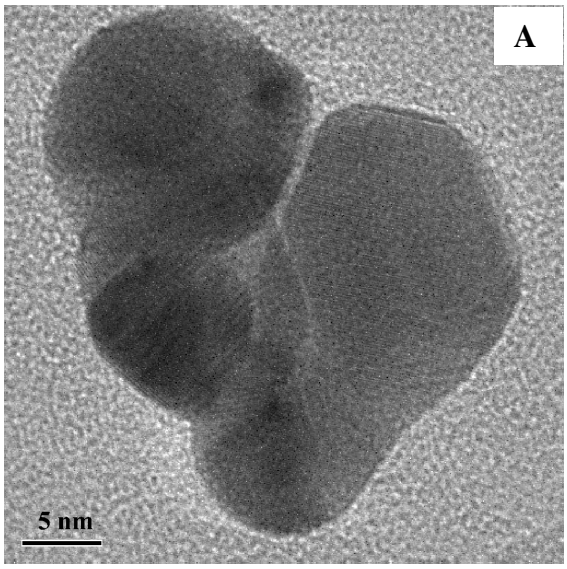

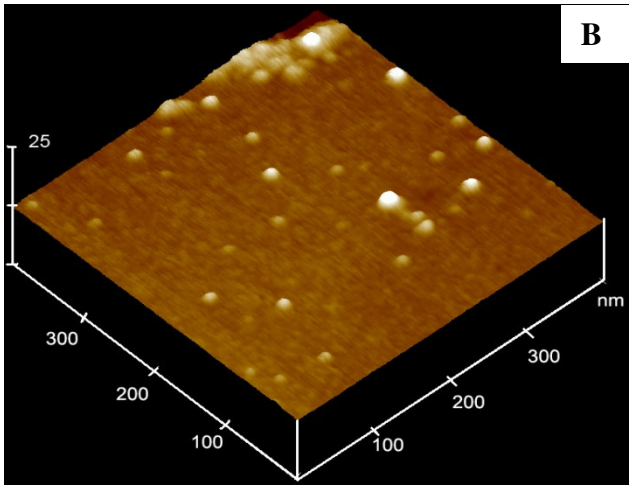

Figure 4.3. (A) HR-TEM micrograph of the AuQD-antibody conjugates showing the difference in densities of the Au and PAMAM dendrimer, data bar size 5 nm. (B) AFM micrograph of the AuQD-antibody conjugates, image size 400x400 nm.

The AFM micrograph of the AuQD-antibody conjugates is shown in Figure 4.3 B. These results show that the complex is overall uniformly spherical and the size determined by measurement of the structure height is 4.9 nm, consistent with the size determined by HR-TEM of 4.8 nm. The experimental values obtained also agree with calculations accounting for the size of the AuQD, the dendrimer, and a complex formed between these two species. In this case it is possible to discern individual AuQDs as the AFM technique allows for higher resolution imaging. The AuQDs are randomly distributed on the surface of the substrate with occasionally clustered groups. The observation of clusters could either be aggregated AuQDs or multiple AuQDs within the same dendrimer appearing as separate species.

The complex was further analyzed using Bio-attenuated total reflectance fourier transform infrared spectroscopy (Bio-ATR FTIR). While the dendrimer and the anti-human IgG can be identified by Bio-ATR FTIR, the AuQDs cannot. Figure 4.4 presents the Bio-ATR FTIR results of reference solutions of dendrimer (4.4 A) and anti-human IgG (4.4 B) along with the PAMAM encapsulated anti-human IgG conjugated AuQD complex (4.4 C).

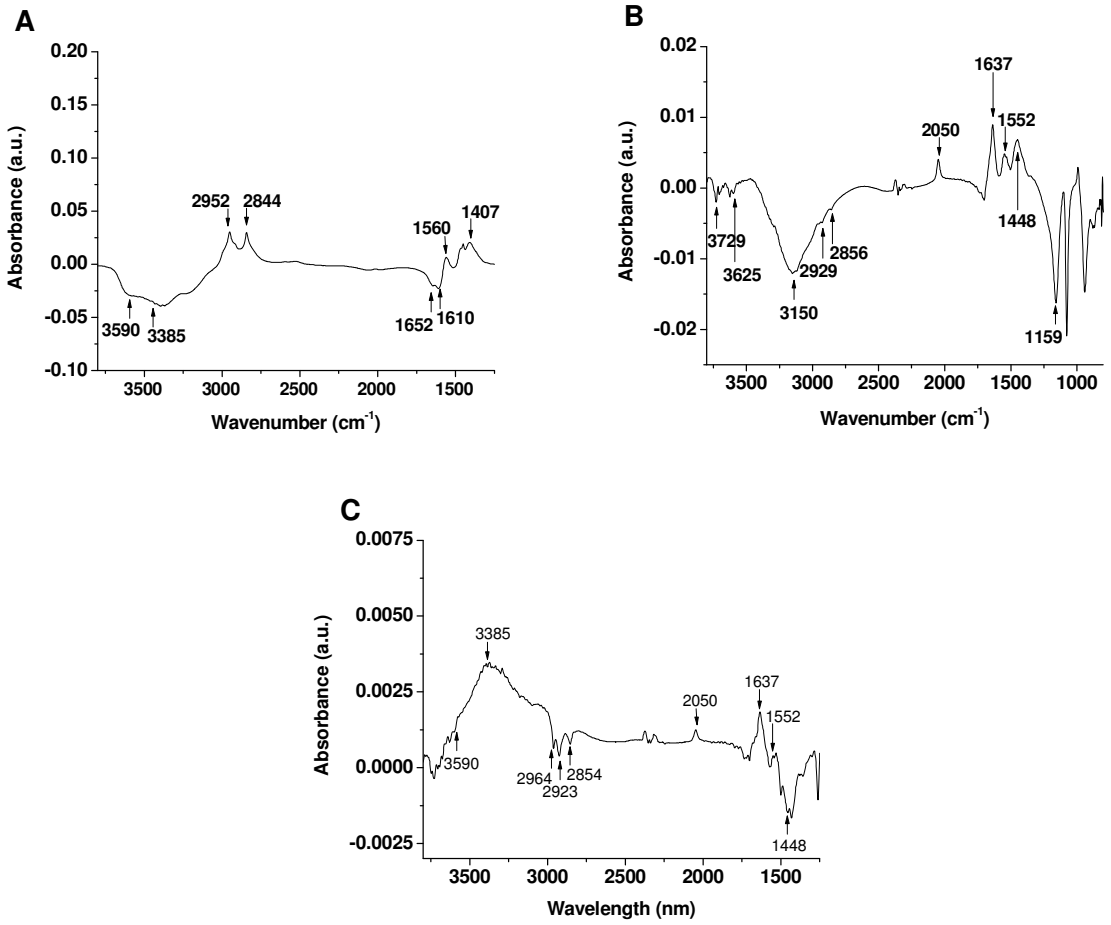

Figure 4.4. Bio-ATR FTIR spectra of aqueous (A) PAMAM-OH generation 2 dendrimer; (B) anti-human IgG; (C) PAMAM encapsulated anti-human IgG conjugated AuQDs.

The spectrum of the dendrimer (Figure 4.4A) is characterized by a large amide absorption at 3590 cm^{-1} and a band at 3385 cm^{-1} resulting from the terminal hydroxyl groups of the dendrimer, along with an amide I band at 1610 cm^{-1}. Other less characteristic bands found in the spectrum are –NH bending at 1560 cm^{-1} and methylene bending at 1407 cm^{-1}. In contrast, the spectrum of the anti-human IgG (Figure 4.4B) is characterized by amine stretching at 3729 and 3625 cm^{-1}, hydroxyl stretching at 3150 cm^{-1}, a band at 2050 cm^{-1} that could result from C, N, O stretching or stretching of a carbon-carbon double bond, and an amide I band at 1637 cm^{-1}. Less characteristic bands are found at 2929 and 2856 cm^{-1} resulting from methylene stretching, 1552 cm^{-1} resulting from –NH bending, and 1448 cm^{-1} resulting from methylene bending. It is worth indicating that the sign of the absorbance bands of the sample is a result of the technique used and is related to the orientation of the sample to the crystal surface resulting in both positive and negative bands.

Figure 4.4C presents the Bio-ATR spectrum of the AuQD-PAMAM-AntiIgG complex (dendrimer encapsulated Au quantum dot and anti-human IgG conjugated to it). The resulting spectrum is a convolution of the Bio-ATR spectra of the PAMAM dendrimer and the anti-human IgG. An amide absorption resulting from the dendrimer can be seen at 3590 cm^{-1}, while the band resulting from the terminal hydroxyl groups of the dendrimer is at 3385 cm^{-1}; both are found in the same position as in the spectrum of the dendrimer alone. Methylene stretches can be seen at 2964, 2923, and 2854 cm^{-1}. The band at 2050 cm^{-1} found in the spectrum of the anti-human IgG along with the amide I at 1637 cm^{-1} are also present in the spectrum of the AuQD complex. The results of the

luminescence, TEM, AFM, and IR indicate that indeed, the AuQD is stabilized by the dendrimer and that the antigen is conjugated to the system through the specific binding of the antibody variable chains.

4.4 Immunoassay for the detection of human IgG in solution

The purpose of designing this complex was for the proof-of-concept of a fluorescence-based immunoassay. As a particular implementation of such an assay, the detection of human IgG in aqueous solution was chosen. The mechanism of action is a well-known direct-binding immunoassay principle. Immunoglobulins may have various sites available for binding, however, in this case of human IgG there are two sites available for binding of the human IgG antigen. As can be seen from the results presented in Figure 4.5, the introduction of antigen into the system results in nano-sized agglomeration, and additionally, luminescence quenching of the AuQD results. The luminescence can be effected in two ways; first, as QDs are sensitive to surface effects, the introduction of antigen and selective binding of an antibody-PAMAM-dendrimer-Au QD complex with an introduced antigen such as human IgG results in interaction with the portion of the chain of the antigen anti-human IgG and the surface of the AuQD. Another possibility is that the resulting agglomeration that occurs after antigen introduction, as visualized in Figure 4.5, can act as a filter decreasing the luminescence intensity of emission.

As can be seen, prior to the addition of human IgG (Figure 4.5 A), the AuQD anti-human IgG complex is found virtually free of clusters. However, after the

introduction of human IgG antigen, (Figure 4.5B) agglomeration occurs to an extent that could indeed filter out or scatter the emission of the AuQDs.

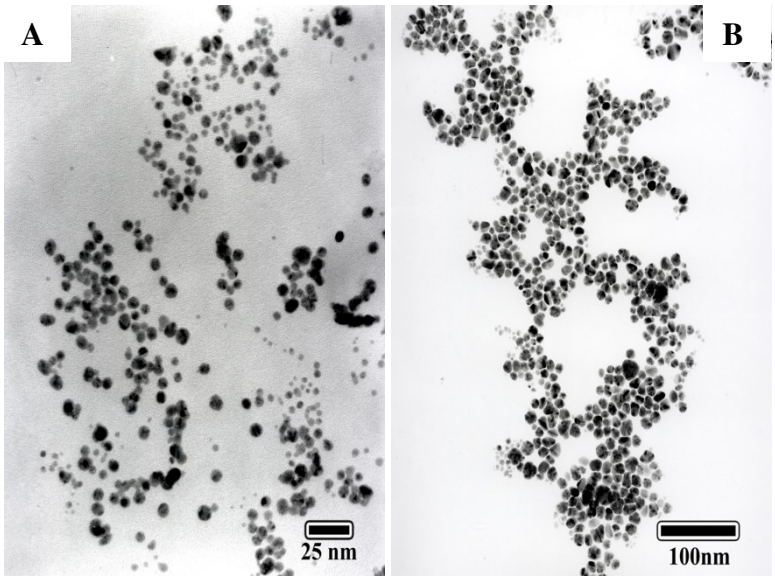

Figure 4.5. (A) HR-TEM micrograph of AuQD-antibody conjugates, data bar size 25 nm (B) HR-TEM of the formation of the complex agglomerate formed upon the addition of human IgG, data bar size 100 nm.

To determine the mechanism of quenching, selectivity, stability, and possible interference, various quenching studies were performed with numerous complexes. Human and rabbit IgG were used to compare the specificity of the system towards immunoglobulins, while bovine serum albumin (BSA) and β-casein were used as model proteins that are found in high concentration in biological systems to probe sources of interference and to demonstrate assay selectivity against non specific protein binding. The as used antibody did not show a good selectivity between rabbit and human IgG

antigen, the quenching of fluorescence occurred with addition of rabbit IgG also. However, the system does not respond to non-specific binding, as addition of both BSA and β-casein resulted in a minor luminescence quenching effects, as depicted in Figure 4.6A.

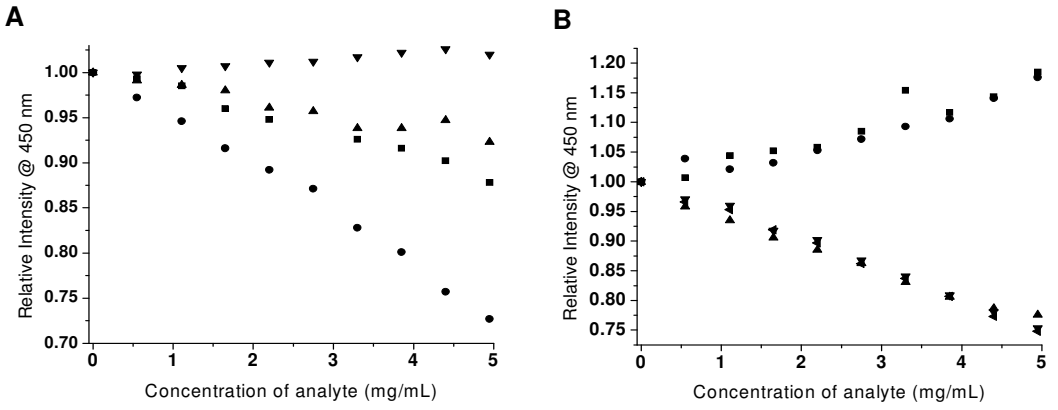

Figure 4.6. Relative intensity at 450 nm of the photoluminescence versus concentration of analyte added in aqueous solution for (A) AuQD PAMAM anti-human IgG complex titrated with β-casein (▼), rabbit IgG (●), BSA (▲), and human IgG (■) and (B) AuQD PAMAM complex titrated with BSA (■), β-casein (●), human IgG (▲), rabbit IgG (▼), and goat IgG (◄).

In order to determine how the various non-specific immunoglobulins and proteins interact with the surface of the AuQDs, the AuQD PAMAM complex (without anti-human IgG) was used in the titrations, the results of which can be seen in Figure 4.6. Both BSA and β-casein resulted in an increase in the luminescence intensity with increasing concentrations. With increasing concentrations of IgGs the luminescence

intensity decreased, interestingly, however, they caused a decrease of the same magnitude, such that they were indistinguishable based on the quenching curves. This would indicate a strong non-specific interaction between the AuQD surface and the immunoglobulin regardless of its source. Based on the observed results, the luminescence quenching when antigen is present in the vicinity of the complex is a result of multiple antibodies binding leading to agglomeration and surface quenching of the AuQDs. In the proof-of-concept case of the human IgG detection, the system is linearly sensitive and linear over a broad range from micromolar to nanomolar concentrations, as demonstrated on a dynamic curve.

The other proteins tested, namely BSA and β-casein, did not cause a large change in the fluorescence signal. BSA resulted in a minor decrease in the intensity of the luminescence, while β-casein resulted in a minor increase in the luminescence intensity, which can be attributed to some of the non-specific binding of those proteins to PAMAM or directly to the gold QDs. Thereby, it is to expect, that with a higher saturation of the antibody-PAMAM-AuQD complex with antibodies, the statistically available surface of PAMAM or AuQD for non-selective binding will decrease, and the assay specificity will further increase.

4.5 Conclusion

AuQDs encapsulated within second generation PAMAM dendrimers were electrostatically conjugated to anti-human IgG for the purpose of detecting human IgG in solution. The complex formed exhibits excellent stability. A linear decrease in the luminescence of the AuQDs was found with increasing concentrations of human IgG

over a micromolar to nanomolar concentration range. Neither BSA nor β-casein caused significant interference. The results teach us that the mechanism of antibody-induced selectivity in competitive surface quenching, coupled with the inherent property of quantum dots of size-controlled fluorescence spectra has a great promise for the use and design of a variety of ligand-specific assays for diagnostics and imaging applications.

Chapter 5. Protein and enzyme stabilized CdS quantum dots

5.1 Background

Differing nanoapplications of gold have been discussed in the previous two chapters: both nanoparticles and quantum dots were investigated. Numerous synthetic routes for direct single step preparations of nanoparticles for biological applications without further modification for biological activity are well known, however, a major limitation of semiconductor quantum dots is that separate reactions for the synthesis, aqueous solubility, and bioconjugation of these particles are needed before they are made suitably biologically active. This chapter presents a method for a single step reaction that results in biologically active semiconductor nanoparticles. In addition, an application of OPAA CdS quantum dots prepared in this fashion is investigated.

Quantum dots (QDs) have controllable optoelectronic properties making them attractive for applications in a variety of fields[101]. Biological hybrids of these nanoparticles have been used as luminescent probes for imaging, detection, clinical diagnostics, and drug delivery[102]. Of the available synthetic routes for the synthesis of QDs arrested precipitation is a common technique in which the QDs are stabilized by surface ligands. The nature of the ligand stabilizing the QD can influence its solubility, net charge, stability, optical, and electronic properties[103]. Nanoparticle size can be controlled by using different ligands at various concentration levels[104]. In addition, various surface ligands have been utilized to manipulate the shape and physicochemical properties of QDs[105]. As a result, most QD-based applications rely on surface chemistry to achieve the required functionality. New stabilizer systems for the synthesis and

manipulation of quantum dots are of great interest for their bioapplications. A major limitation to the established synthetic routes is that the majority of these bioapplications of QDs involve a separate synthetic step for the formation of a bioactive QD with a stabilizing surface ligand, which involves either a place exchange reaction between the biomolecule and the surface ligand, electrostatic or covalent conjugation of the biomolecule of interest to the surface stabilizing ligand, or use of adaptor proteins such as biotin and avidin, or polyhistidine tags. Recently however, direct conjugation of proteins (e.g. bovine serum albumin) with QDs has been reported in the literature[106]. In this conjugation process, the templating effect is provied by the rapid expansion of a supercritical fluid in place of surfactants/surface ligands.

In this chapter a direct synthesis for a bioconjugate of protein stabilized QDs is described. Various proteins and enzymes were selected and tested for their stabilizing capability. Of those tested, bovine serum albumin (BSA), β-casein, and organophosphorus acid anhydrolase (OPAA) produced water soluble CdS QDs in a single step reaction. As a representative example of an application of such QDs, OPAA Cds QDs are discussed in detail.

Organophosphorus acid anhydrolase (EC 3.1.8.2) is a hydrolytic enzyme. It has been identified for the detection and decontamination of various neurotoxins including pesticides, G-type and V-type chemical nerve agents[107]. In the synthesis, OPAA was used as the only stabilizer for CdS quantum dots, therefore, after the synthesis, OPAA was directly conjugated to the surface of the QDs. This direct conjugation eliminates the need for electrostatic interactions or surface modifications[108], which are commonly used to link QDs and enzymes. Direct conjugation is advantageous in that it is expected to

minimize enzymatic structural changes and loss of protein/enzyme activity. Upon the successful synthesis of the OPAA-QD conjugate, an application involving the detection and detoxification of a neurotoxin analogue compound, diisopropylfluorophosphate (DFP) was examined. DFP is an attractive analogue for chemical warfare nerve agents in research as DFP has a similar phosphonofluoridate neurotoxic structure but a significantly reduced toxicity compared to G-type nerve agents such as sarin and soman[109].

5.2 Proteins and enzymes studied

Various parameters that can effect QD formation include ligand charge, size, and concentration. In determining which proteins and enzymes to test for direct QD stabilization these parameters along with molecular weight, isoelectric point and charge stabilizing residues must be examined. Compounds containing free sulfur atoms are well known to stabilize and impart water solubility to QDs. Therefore, it was believed that proteins with a large number of cysteinee residues could promote QD formation. It was hypothesized that isoelectric point, net charge at synthetic pH, molecular weight and number of cysteinee residues could potentially influence QD stabilization. To test the above mentioned hypothesis various well characterized and commonly utilized proteins were selected.

Table 5.1 provides a list of each protein along with important characteristics. A total of seven proteins were examined with three successful cases of protein stabilized QD formation.

QD formation	Protein	Molecular Weight	pI	Cysteinee Residues	Overall Charge
Y	OPAA	58,000	6.8	5	+
N	OPH	35,000	7.6	1	+
Y	BSA	66,000	4.7	35	+
N	Cytochrome C (bovine heart)	12,300	10	2	-
N	Hen Lysozyme	14,400	10.5	6	-
N	Pepsin	35,000	3.3	7,13,14	+
Y	β-Casein (Bos Taurus)	23,000	4.5	0	+

Table 5.1. Proteins studied and selected characteristics.

As can be seen in Table 5.1 above proteins chosen, namely, organophosphorus acid anhydrolase (OPAA), organophosphorus hydrolase (OPH), bovine serum albumin (BSA), cytochrome c, hen lysozyme, pepsin, and β-casein varied in their molecular weight, isoelectric point, number of cysteinee residues, biological function, and overall charge at the synthetic pH. OPAA, BSA, and β-casein were successful in stabilizing QDs.

5.3 Synthesis and characterization

An arrested precipitation procedure was used for all syntheses. The method for the OPAA CdS QD synthesis will be discussed as a representative example. The OPAA-CdS QDs were synthesized by first preparing a solution containing 0.43 mg/mL of OPAA and Cd^{2+} in Ar-flushed purified water. The pH of the solution was adjusted to 8.5 with concentrated NaOH. Then, S^{2-} was introduced into the solution with rapid stirring. The final concentration of Cd^{2+} and S^{2-} ions was $1x10^{-3}$ M each. Finally, the solution was continuously mixed for 1 h. The solution was purified by a Sephadex G75 column.

The OPAA-CdS QDs and excess OPAA were eluted by the Borex/HCl (pH 8.5) buffer through a 2.22 x 22.25 cm (Diameter x Height) Sephadex G75 column (Fig. 5.1 A). Each 3 mL fraction was collected and measured by UV-Vis spectroscopy. From fractions 9-13, the absorption of OPAA-CdS can be clearly observed at 410 and 278 nm (Fig. 5.1 B). In the fractions 27-34, the OPAA absorption band was observed at 278 nm as shown in Figure 5.1 C.

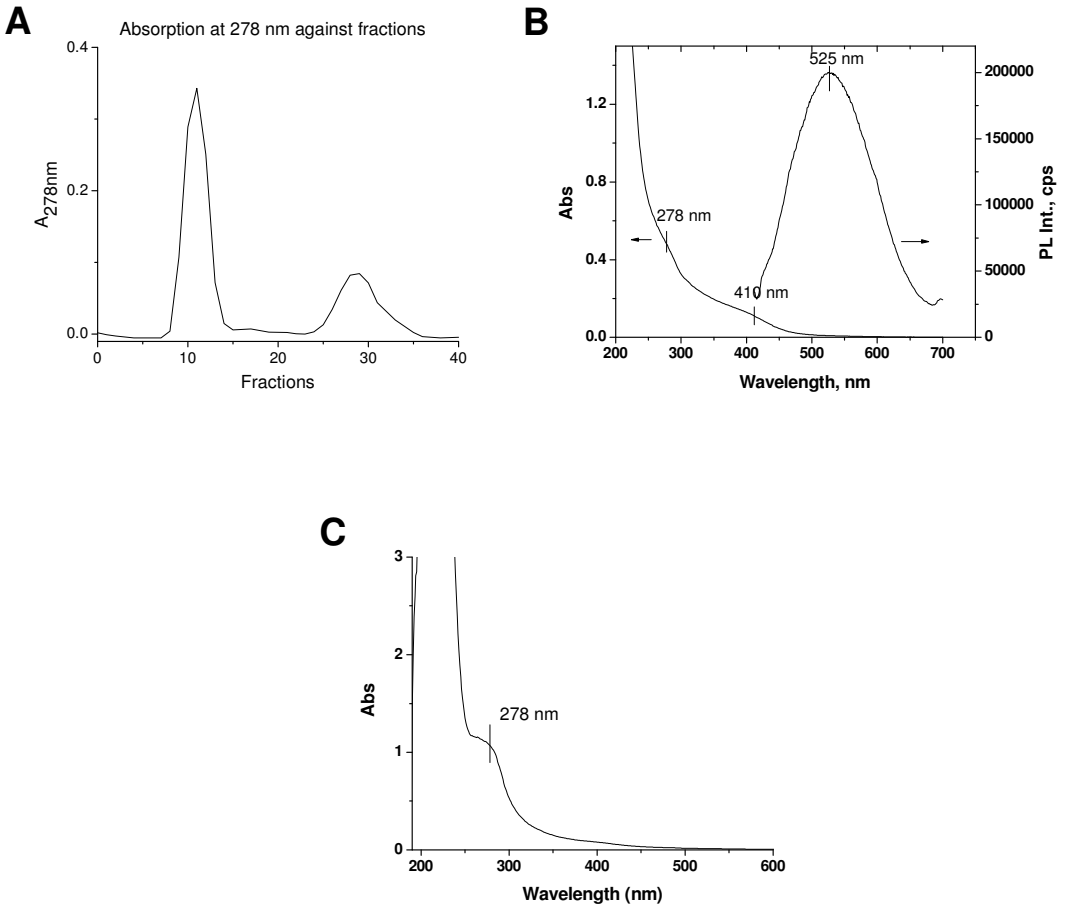

Figure 5.1. (A) Absorption spectrum of the fractions at 278 nm; (B) Absorption and luminescence spectra of OPAA-CdS QDs after purification by Sephadex G75 column (all fractions from 9-13); and (C) Absorption spectrum of OPAA (all fractions from 27-34).

One of the parameters studied in the synthesis of the CdS QDs included pH (5.0, 6.8, and 8.5). OPAA has an isoelectric point of 6.8. Therefore, at the basic pH, the enzyme should have a net negative charge. However, at pH 5.0, it should be positively charged. The synthesis of the OPAA QDs was most successful under basic conditions. At other pH values, precipitation of CdS was observed.

QDs were characterized by absorption and luminescence spectroscopies. Figure 5.2 presents the absorption and luminescence spectra of the protein QDs. In Figure 5.2 A the absorption spectrum of the OPAA QDs are shown. It can be seen that the spectrum is characteristic of a QD; the absorption is broad with two visible transitions, one at 278 nm and another at 410 nm. This absorption shoulder corresponds to a particle size of 4.1 nm. The photoluminescence spectrum reveals an emission maximum at 525 nm for the OPAA QDs. In contrast, the BSA QDs exhibit an emission maximum at 543 nm and show a broad absorption with no clear transition wavelength.

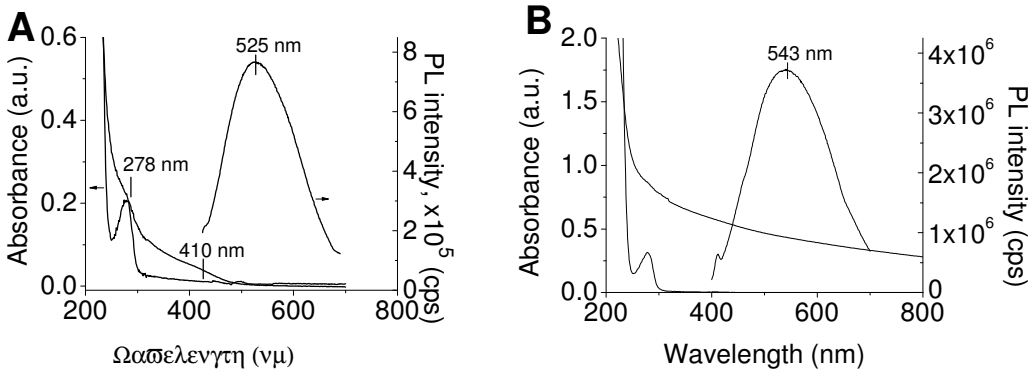

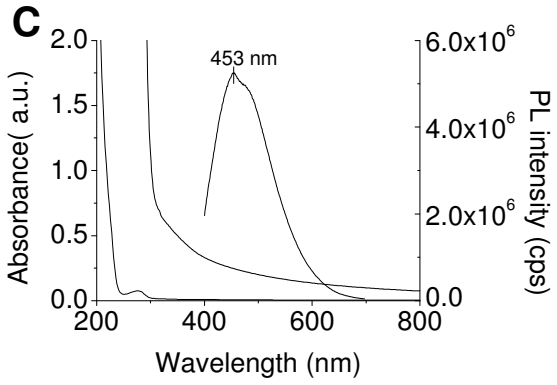

Figure 5.2. Absorption and luminescence spectra of (A) OPAA, (B) BSA, and (C) β-casein.

Similarly, the β-casein QDs show a broad absorption with no clear transition, while the emission maximum is at 453 nm. As a reference, the absorption spectra of the corresponding pure proteins in solution may be seen in Figure 5 as well. The characteristic peptide bond absorption at just above 200 nm may be seen for all three proteins along with an absorption band at 278 nm corresponding to the absorption of tyrosine and tryptophan residues.

OPAA QDs were additionally investigated by HR-TEM in order to determine the size of the QDs formed. According to HR-TEM analysis (Figure 5.3 below), the size determined was 4.0 nm agreeing well with the absorption measurements indicating a size of 4.1 nm as mentioned above. The particles appear spherical in shape and fairly well distributed over the substrate surface.

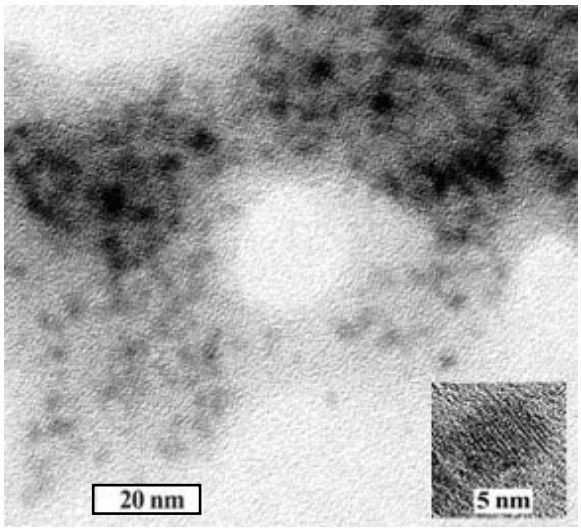

Figure 5.3. HR-TEM micrograph of OPAA CdS QDs.

Due to a large organic component of the OPAA CdS QDs there was quite a large amount of difficulty in obtaining the micrographs which are not very clear. However, the metallic CdS core is still visible in enough detail to perform size analysis and obtain morphological details.

Circular dichroism (CD) spectroscopy was used to investigate any possible secondary structural change to OPAA prior to and after CdS QD formation; the results of which can be seen in Figure 5.4 and Table 5.2 below.

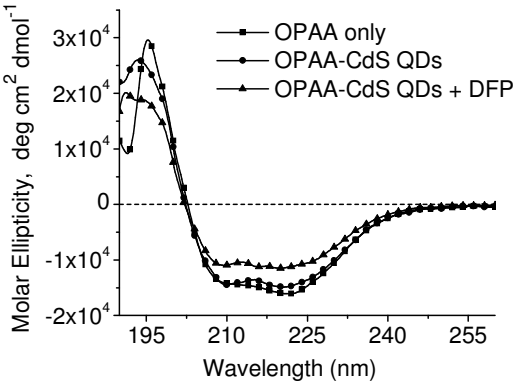

Figure 5.4. CD Spectra of OPAA, OPAA-CdS QDs and OPAA-CdS QDs in the presence of 1 $\times 10^{-4}$ M DFP.

The CD spectra presented were analyzed using CDPro software. Visual inspection shows very little change in the spectrum of OPAA alone compared to the spectrum of the OPAA CdS QDs. Before the conjugation, there are two obvious double negative peaks at 209 and 222 nm and a strong positive peak at 195 nm, all indicating an α-helical structure. Table 5.2 shows the average percentage of the secondary structures estimated from the data analyzed by CDPro software. Before conjugation, the regular and distorted α-helical contents were 24.1 and 21.3%, respectively. After formation of CdS QDs the two double negative peaks remained almost the same and the positive peak blue shifted only slightly, around 1-2 nm. Both the positive and negative peaks are slightly less obvious

	Fraction of Secondary Structure					
	α-helix		**β-strand**		**Other**	
	Regular	distorted	Regular	distorted	Turn	Unordered
OPAA	24.1	21.3	7.9	10.1	18.1	18.2
OPAA/QDs	23.1	20.7	10.7	6.8	19.8	16.9

Table 5.2. Secondary structure percentage of of OPAA, OPAA-CdS bioconjugate with and without the presence of 10^{-4} M DFP.

which is confirmed by the secondary structure changes from CDPro. The regular and distorted α-helical contents decreased from 24.1 and 21.3% to 23.1 and 20.7%, respectively. These changes indicated that OPAA retained its main secondary structure after conjugation with CdS QDs. In the presence of $1x10^{-4}$ M DFP, the CD spectra of OPAA-CdS QD solution lost the two double minima and the positive peak. The data from CDPro showed that the regular and distorted α-helical contents decreased from 23.1 and 20.7% to 13.9 and 12.5%, respectively. The regular and distorted β-strand increased from 10.7 and 6.8% to 16.4 and 17.6%, respectively. These spectral changes are due to the hydrolysis of DFP catalyzed by OPAA favouring β-strand over α-helical structure.

5.4 Application: OPAA stabilized CdS quantum dots for the detection and decontamination of organophosphorus compounds

OPAA (EC 3.1.8.2) is a hydrolytic enzyme and it has been identified for detection and decontamination of various neurotoxins including pesticides and G-type chemical nerve agents[110]. Towards this purpose studies were performed to determine if these directly conjugated OPAA CdS QDs were suitable for the optical detection and detoxification of a neurotoxin diisopropylfluorophosphate (DFP), an analogue of more potent OPAA neurotoxin substrates. Titrations were performed in which various concentrations of DFP were added to a solution of the OPAA CdS QDs and the

photoluminescence spectrum was acquired. It was found that the photoluminescence intensity decreased with increasing concentrations of DFP. The QDs were able to detect DFP down to nanomolar concentrations, the results of which can be found in Figure 5.5, below.

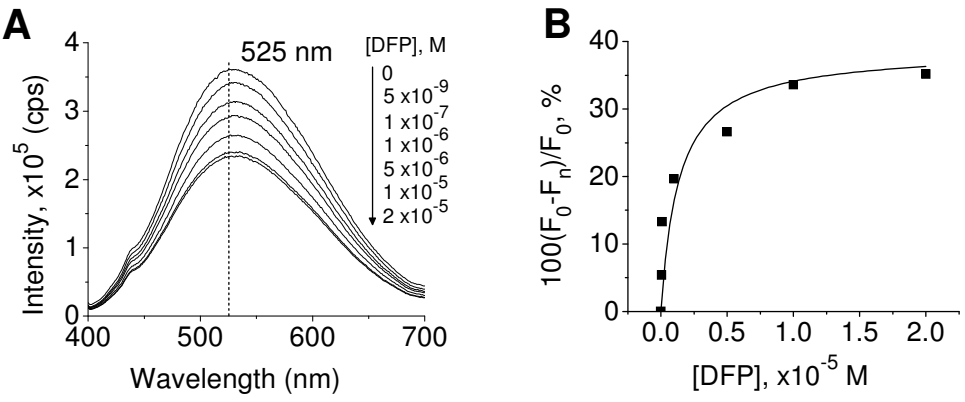

Figure 5.5. (A) PL spectra of OPAA-CdS QD solution in the presence of DFP at different concentration levels; (B) Plot of percent PL quenching as a function of DFP concentration. F_o and F_n represent maximum PL intensity in the absence and presence of DFP, respectively.

It can be seen that with increasing concentrations of DFP, there is decrease in the PL intensity. DFP did not induce PL quenching of CdS QDs stabilized with thioglycolic acid or in the absence of OPAA. Therefore, changes in OPAA secondary structure, enzyme-substrate complex, and/or product formation may account for the quenching effect of DFP. Changes in surface passivation and charge transfer may be possible mechanisms. Figure 5.5 B shows that the relative PL intensity percentage of OPAA-CdS QDs is hyperbolically dependent on the concentration of DFP, $y = (38.73871x) / (1.2576x10^{-6} +$

x). The maximum quenching percentage to DFP calculated from Figure 5.5 B was 38.7% for the OPAA-CdS QD conjugate.

5.5 Conclusion

Protein stabilized CdS QDs in which the protein is directly conjugated to the metallic core have been synthesized. Various proteins were investigated, and while no strict criteria have been determined for successful formation, all those formed had isoelectric points between 4.5 and 7 and posses some sort of binding capacity or function in vivo. The number of cysteine residues present in the protein along with molecular weight may also play a role in the successful synthesis. This would imply that the overall charge on the protein is important along with its capability to bind species. OPAA CdS QDs synthesized were able to detect and decontaminate a neurotoxic solution of DFP. It is possible to detect DFP at a nanomolar level under the conditions above. We hypothesize that MW is an important parameter in the successful formation of protein stabilized QDs.

Chapter 6. Conclusion of work completed and future considerations

This dissertation set out to present various relevant biological applications of nanoparticles and nanocrystals while highlighting methods for overcoming accepted limitations of the technologies. The research conducted utilized various methodologies including Langmuir surface chemistry, photoablation, a fluorescence quenching immunoassay, and enzyme stabilized QDs for the detection and decontamination of an organophosphorus compound.

Chapter 2 was concerned with validating short peptide fragments based on the full length β-amyloid peptide for use as a model for aggregated peptide. Using classic Langmuir surface chemistry techniques of surface-pressure and surface-potential area isotherms, along with the techniques of FTIR and CD spectroscopies, and the microscopic technique of epifluorescence microscopy, it was determined that these short peptide fragments do indeed aggregate, and in relatively short time periods. It was determined that the shortest peptide fragments Aβ(31-35) were the most potent aggregators as compared to the larger Aβ(25-35) fragments. The point of validating these peptides was for their further use in photoablation experiments based upon Au nanoparticles which is discussed in detail in chapter 3.

Chapter 3 presented a gold nanoparticle based system for the photoablation of aggregated peptide samples. The system was composed of mono- or minimally functionalized Aβ(31-35) and Aβ(25-35) Au nanoparticles. These particles were introduced into peptide solutions and they were allowed to be incorporated into the aggregated formed. Laser irradiation at the surface plasmon band, 520 nm, of the Au

nanoparticles resulted in photoablation of the aggregated protein as confirmed by TEM, SEM, and AFM microscopies. It was also shown that the incorporation of the gold nanoparticles did not greatly alter the aggregation characteristics of the proteins. This chapter provided for an application of photoablation based on Au nanoparticles, which happen to be greatly lacking in the literature. The general method used may also be readily extended to DNA and RNA samples as a result of the unique functionalization strategy that utilized a solid phase based method for simple and directed conjugation of a minimal number of target molecules to the surface of the Au nanoparticles.

Chapter 4 dealt with a different type of particles, namely quantum dots. While applications of semiconductor quantum dots have been well studied in the literature over the past decade or so, the use of newly discovered AuQDs have not. At the time of investigation, surprisingly, no applications of these particles had been reported, and to date very few applications have been published. This chapter discussed the details of a strategy for an immunoassay directed at the detection of human IgG in solution at nanomolar concentrations based on anti-human IgG conjugated AuQDs. An electrostatic conjugation method was employed for the attachment of the antigen to the AuQDs. The detection was based upon a fluorescence quenching mechanism that was a result of two factors; direct surface quenching of the gold QDs, and an agglomeration effect that is common to immunoglobulins. While IgG was used, this method may be extended to other immunoglobulins, and as a result of current immunochemistry capabilities, this opens the possibility for the detection of a wide range of biological analytes.

Finally, chapter 5 was concerned with overcoming the need for multiple synthetic steps for the production of biologically active semiconductor quantum dots. As all

quantum dots rely on surface stabilization, it was hypothesized that perhaps proteins and enzymes could be used to directly stabilize these particles. In order to test this hypothesis, various proteins and enzymes were investigated for their potential stabilization. Surprisingly, three such examples were found: BSA, β-casein, and OPAA were able to directly stabilize CdS QDs. The synthesis, outlined in detail in chapter 5, was conductor under mild conditions and resulted in water soluble CdS QDs. Also of importance, was the fact that the stabilizing enzymes retained their secondary structure which leads the authors to believe that their biological activity may not be effected. As an application, the use of OPAA CdS QDs were studied for their usefulness in detecting and decontaminating solutions of the organophosphorus compound DFP. The success of this synthetic strategy resulted in QDs that were water soluble and biofunctionalized in a single synthetic step, and after simple purification, were readily available for bioapplications.

While various shortcomings related to the technologies used were circumvented, it still remains that the best use of these nanoparticles is not to replace existing research capabilities but rather to augment them. In general, for a particular biological application, a certain particle must still be tailored for specific use; no general synthetic strategy, conjugation scheme, or detection mechanism is universally available for the investigation of any biological phenomenon. However, there is no doubt that future research into the area of nanotechnology will result in numerous applications and consumer products of importance, and in particular, the fields of molecular biology and medicine will be greatly enhanced by these technologies.

Chapter 7. Experimental

7.1 General

All chemicals and solvents used were purchased from either Sigma-Aldrich (St. Louis, MI) or VWR (Westchester, PA) unless otherwise noted. Chemicals and solvents obtained were at least reagent grade if not at the highest purity available. For the purpose of surface chemistry measurements solvents used were a minimum 99.99% pure.

7.2 Chapter 2 experimental-Amyloid peptide fragments as model for aggregated protein: a two dimensional approach

The Wang resin and amino acids used for peptidolipid synthesis were purchased from Advanced Chem. Tech. (Louisville, KY). All amino acids were of the L-configuration, except for glycine. All organic chemicals and solvents were of reagent grade and obtained from Aldrich (St. Louis, MO). The ^{1}H-NMR data were acquired with a Bruker 500 MHz spectrometer (Boston, USA). Low resolution FAB was recorded on a VG-Trio 2000 mass spectrometer. High resolution FAB was conducted on a 70-4F instrument and performed at the Mass Spectrometry Laboratory of the University of Illinois at Urbana-Champaign or the University of Miami.

Synthesis and purification of the peptidolipid Aβ(25-35). Peptidolipid Aβ(25-35) was prepared by the solid-phase methodology on Wang resin (1.3 mmol/g). Briefly, coupling reactions were carried out with a 3-fold excess of Fmoc-amino acids with

diisopropylcarbodiimide(DIC) / 1-hydroxybenzotriazole (HOBT) as activating agent in dimethylformamide (DMF). Intermediate deprotection was achieved with 20% (v/v) piperidine in DMF for 30 min. After an average coupling period of 1 h, the extent of acylation was monitored via the standard ninhydrin test. In the event of incomplete coupling, the coupling procedure was repeated. After final deprotection, stearoyl chloride was coupled to the peptide-resin using the same coupling protocol as mentioned above to yield the peptidolipid product. The cleavage of the peptidolipid from the resin was performed with trifluoroacetic acid in the presence of 8% anisole, 2% dimethyl sulfide, 2% p-cresol, and 2% thiocresol at 0 °C for 2 h. After removal of the trifluoroacetic acid under a stream of nitrogen followed by vacuum, the crude peptidolipid was precipitated with diethyl ether, filtered off, washed with water and diethyl ether, extracted with 50% (v/v) aqueous acetic acid, and lyophilized. The synthesized peptidolipid was purified by semipreparative reversed-phase high-performance liquid chromatography (RP-HPLC) on a Waters 2690 separation module. Eluants used were 0.1% trifluoroacetic acid in water (v/v; A) and 0.1% trifluoroacetic acid in n-propanol : acetonitrile (50:50, v/v; B). Column conditions: Vydac 219TP1010 (diphenyl, 10 μm, 10 mm i.d.×250 mm). The purity of the synthesized peptidolipid was verified by analytical RP-HPLC and MS. Analytical RP-HPLC was conducted on a small-scale column (Vydac 219TP54, diphenyl, 5 μm, 4.6 mm i.d.×150 mm). The same eluants were used as described above and elution gradient was 100-85% B in 50 min; the flow rate was 0.6 ml/min. The purity was greater than 95%.

General methods for surface chemistry study. All the isotherm measurements were conducted in a clean room [class 1000] where constant conditions of temperature (20.0 ± 0.5°C) and humidity (50 ± 1%) were maintained. The spreading solvent was 0.1%

TFA in chloroform: methanol (5:1; v/v), and the solvents [HPLC grade] were purchased from Fisher Scientific Co. (Pittsburgh, PA). The water utilized as subphase (pH 5.8) for the monolayer study was purified by a Modulab 2020 water purification system (Continental Water System Corp., San Antonio, TX) with a specific resistivity of 18 MΩ·cm and a surface tension of 72.6 $mN \cdot m^{-1}$ at 20.0 ± 0.5 °C. The spreading volume of the peptidolipid solutions (4×10^{-4} mmol ml^{-1}) was 30-60 μL. After the solution was spread, a 15 min period was allowed for complete evaporation of the spreading solvent prior to compression. The compression rate for the Langmuir trough was set up at 8 mm min^{-1}. A KSV mini-trough (KSV Instrument Ltd., Helsinki, Finland) was utilized for surface pressure-area isotherm measurements. Computer-controlled symmetrically movable barriers were used to regulate the surface area. The area available for spreading solution was 7.5×30.0 cm^2. The surface pressure was measured by the Wilhelmy method with a sensitivity of ± 0.01 $mN \cdot m^{-1}$. Surface potential measurements were obtained on the KSV trough using a Kelvin probe. This probe consisted of a capacitor-like system. The vibrating plate was set at approximately 1 mm above the surface of the Langmuir monolayer and a counter electrode was dipped into the clean subphase which was taken as the zero reference. All the surface pressure and surface potential-area isotherms were measured at 20.0 ± 0.5 °C.

Microscopic study. An epifluorescence microscope (Olympus IX-FLA) was used for acquiring the fluorescence micrographs of the Langmuir monolayer at the air-water interface at different surface pressures. A Kibron mini-trough (area available for spreading solution 5.9×19.5 cm^2, Kibron Inc., Helsinki, Finland) was used for the preparation of the Langmuir monolayer. A thermoelectrically cooled Optronics

MagnafireTM CCD camera detected the emission of a fluorescent probe, namely (5-octadecanoylamino) fluorescein (ODFL); this fluorescent probe was mixed with the peptidolipid prior to spreading, the molar mixing ratio of ODFL : peptidolipid was 1:100.

Spectroscopic study. Polarization Modulation-Infrared Reflection Absorption Spectroscopy (PM-IRRAS) measurements were performed on the Bruker EQUINOX 55 FT-IR spectrometer (Bruker Optics Inc., Billerica, MA) equipped with a XA-511 external reflection-absorption accessory for air-water interface measurements. The IR beam was conducted out of the spectrometer and focused onto the water surface of the Langmuir trough. The accessory was enclosed in a polymethylmethacrylate cover. The spectra were acquired for 1200 scans with water as background. Spectral resolution was 4 cm^{-1} with an MCT liquid nitrogen cooled detector that assures high scan velocity and a good signal to noise ratio. Prior to interaction with the sample, the IR signal was polarized using a BaF_2 polarizer and modulated using a photoelastic modulator (PEM, Hinds Instruments, Inc., Hillsboro, OR) throughout the measurements. Demodulation was performed using a SSD 100 unit (GWC Technologies, Madison, WI). The spectra were not smoothed in the present study. The circular dichroism spectrum of the peptidolipid Langmuir-Blodgett (LB) films was measured using a Jasco J-810 spectropolarimeter (Easton, MD) fitted with a 150-watt xenon lamp. The measurement with LB films used a quartz slide placed perpendicular to the light beam. The spectrum was recorded in the far-UV region (185-260 nm) with a response time of 8 s and scan speed of 50 $nm \cdot min^{-1}$. Three scans were accumulated and averaged for each spectrum after the background of the blank quartz slide was subtracted.

7.3 Chapter 3 experimental- Photoablation of amyloid-like peptide aggregates

Peptide synthesis, characterization and purification. All peptides were synthesized using standard Fmoc solid-phase peptide synthesis (SPPS) procedures with the aid of an AAPPTEC APEX396 automated multiple peptide synthesizer. Pre-loaded Fmoc-Wang resins (Sigma-Aldrich) were swelled in dimethylformamide (DMF) (Sigma-Aldrich) followed by two washing cycles. Amino acids (Advanced ChemTech) were dissolved in a mixture composed of dichloromethane (DCM) (Sigma-Aldrich), DMF, and methanol (MeOH) (Sigma-Aldrich) in equal proportions along with coupling agents hydroxybenzotriazole (HOBt) (Sigma-Aldrich) and benzotriazole tetramethyluronium hexafluorophosphate (HBTU) (Sigma-Aldrich). 0.5 M solutions of both diisopropylcarbodiimide (DIC) (Sigma-Aldrich) and dicyclohexylcarbodiimide (DCC) (Sigma-Aldrich) in N-methyl-2-pyrolidinone (NMP) (Sigma-Aldrich) were prepared and used as activating agents. Double coupling procedures were employed to ensure successful amino acid coupling. Deprotection of amino acids was accomplished by two washing cycles of 20 min each using a 20 v% piperidine solution in DMF. The cleavage of the peptides from the resin was performed with trifluoroacetic acid (TFA) in the presence of 8% anisole, 2% dimethyl sulfide, 2% p-cresol, and 2% thiocresol at 0 °C for 2 h. After removal of the trifluoroacetic acid under a stream of nitrogen followed by vacuum drying, the crude peptide was precipitated with diethyl ether, filtered off, washed with water and diethyl ether, extracted with 50% (v/v) aqueous acetic acid, and lyophilized.

The synthesized peptide was purified by semipreparative reversed-phase high-performance liquid chromatography (RP-HPLC) on a Waters 2690 separation module.

Eluants used were 0.1% trifluoroacetic acid in water (v/v; A) and 0.1% trifluoroacetic acid in n-propanol: acetonitrile (50:50, v/v; B). Column conditions: Vydac 219TP1010 (diphenyl, 10 μm, 10 mm i.d.×250 mm). The purity of the synthesized peptide was verified by analytical RP-HPLC and MS. Analytical RP-HPLC was conducted on a small-scale column (Vydac 219TP54, diphenyl, 5 μm, 4.6 mm i.d.×150 mm). The same eluants were used as described above and elution gradient was 100-85% B in 50 min; the flow rate was 0.6 ml/min. The purity was greater than 95%.

Synthesis, characterization, and purification of triethyleneglycolthiol (EG_3-SH)-protected gold nanoparticles (EG_3Au) and monocarboxylated EG_3Au. To a 100-mL, Erlenmeyer flask, 22.5 mL of methanol was mixed with 3.75 mL of acetic acid. To the stirred solution, 120 mg (0.3 mmol) of hydrogen tetrachloroaurate (III) hydrate and 23 mg (0.13 mmol) of EG_3-SH ligand, prepared according to a reported procedure [34], were added. The clear yellow solution was vigorously stirred while 128 mg (3.4 mmol) sodium borohydride in 3.8 mL deionized water was added dropwise. The color turned immediately dark black due to nanoparticle formation. After reacting at room temperature for two hours, the nanoparticle solution was centrifuged at 5000 rpm for 5 min to remove any large precipitates. The remaining solution was evaporated in a rotary evaporator and the nanoparticles were washed with petroleum ether twice to remove small organic molecules and then recollected in dichloromethane. The nanoparticles were further purified by column chromatography using a silica gel column (pore size 60 Å, particle size 40-75 μm) and a solvent mixture of DCM/MeOH (4:1, v/v) as eluent to narrow the size distribution. The first band contained nanoparticles with an average core diameter of 2 nm and the second band contained nanoparticles with an average size of 5 nm. The

second band nanoparticle product was collected for further modification and conjugation with peptides. The nanoparticle size was characterized and confirmed by TEM analysis.

Monocarboxylated EG_3Au nanoparticles were prepared using a solid phase modification method as reported previously [29-33]. 11-Mercaptoundecanoic acid (MUA) was immobilized on Amberlite IRA-67 ion-exchange resin in a 400:1 mole ratio (NH_2:MUA) through electrostatic interaction between the tertiary amine groups from the resin and carboxyl groups of MUA ligands. A typical loading recipe is the following: 3 g of dried ionic resin (NH_2 group density: 3.6 mmol/g) was suspended in 8 mL dichloromethane. Following the addition of 0.03 mmol 11-mercaptoundecanoic acid, the mixture was shaken at room temperature for 12 h. After washing with dichloromethane and drying with a stream of nitrogen flow, EG_3Au nanoparticle solution in DCM/hexane (1:1, v/v) was added to the resin. The place exchange reaction was allowed to proceed for 1 h at room temperature. During this period the resin turned black. The resin was then washed with DCM and hexane until the solution became clear. The nanoparticles were then cleaved from the resin by adding 5 mL of 10% acetic acid in DCM with gentle shaking at room temperature for 10 min. The solution was separated from polymer resin, collected and concentrated to obtain the crude product. The crude product was washed with petroleum ether to remove any free ligands. The nanoparticles were re-dissolved in a solvent mixture of DCM/MeOH (4:1, v:v) and purified by gel permeation chromatography (LH-20 gel) using the same solvent. A diamine coupling reaction was conducted on the obtained nanoparticle product and the coupled product was analyzed by TEM. The majority of the coupled product was observed as nanoparticle dimers with a small percentage of trimers and other oligomers indicating that monofunctional

nanoparticles were the major product along with a small percentage of nanoparticles containing a few limited number of carboxyl groups on the surface. After coupling peptides with EG_3Au nanoparticles, we used size exclusion chromatography to purify the nanoparticle-peptide conjugates. Using a size exclusion chromatography (LH-20 sephadex gel) with the exact same dimension and solvents, the peptides were eluted from the column in 9-10 minutes after addition of the peptides into the column (confirmed by Ninhydrin test), while the nanoparticle-peptide conjugates were eluted from the column in 4-5 minutes after sample solution was loaded to the column. The peptides and nanoparticle-peptide conjugates were well separated into two fractions. This confirmed that the nanoparticle-peptide conjugate sample did not contain free peptides and the nitrogen signal detected by XPS from the conjugated nanoparticles must come from peptides covalently coupled to the nanoparticles.

Conjugation and purification of monocarboxylated EG_3Au nanoparticles to Aβ peptide. Amyloid peptide Aβ(31-35) or Aβ(25-35) solution (0.5 mg/mL, 500 μL in methanol) was mixed with monofunctionalized EG_3Au nanoparticles solution (0.5 mg/mL, 2 mL in DCM/MeOH, 4:1, v/v). Following the addition of 40 μL DIC, the reaction mixture was gently shaken at room temperature overnight. After removal of the solvent with a stream of nitrogen, the product was purified by passing the nanoparticle-peptide conjugate solution through a small column of Sephadex LH-20 gel (Sigma-Aldrich) to remove any remaining small chemical reagents.

Bio-ATR-FTIR measurements. For Bio-ATR-FTIR measurements the Equinox 55 (Bruker Optics, Billerica, MA) equipped with the Bio-ATR cell II was used with a resolution of 4 cm^{-1} and 137 scans were averaged per sample.

Circular Dichroism measurements. CD measurements were performed using the Jasco J-810 spectropolarimeter (Easton, MD). The source of illumination was a 150-watt Xenon lamp. Samples prepared were aqueous 2 mg/ml Aβ(25-35) solutions at a pH of 5.6 (ultra-pure water) or 2 mg/ml MeOH solutions. The samples were placed in 1.0 mm quartz cuvettes situated perpendicular to the light beam. The spectra were recorded in the far-UV region (185-260 nm) with a response time of 8 s and scan speed of 50 nm min^{-1}. Three scans were recorded and averaged.

Sample preparation for microscopic studies. Samples were prepared as 2 mg/ml solutions (either aqueous or MeOH) and a 20 μl volume (unless otherwise noted) was allowed to evaporate from the surface of a quartz slide for epifluorescence microscopy, a mica substrate for AFM, a silicon substrate for SEM, and a copper grid for TEM, leaving the aggregates.

TEM measurements. Transmission electron microscopy was performed on a Philips EM300, 80-100kV microscope with eucentric goniometer stage (45° sample tilt). Sample preparation consisted of drop coating the AuNPs onto carbon-coated copper grids and air-dried.

SEM measurements. The Scanning Electron Microscope (Phillips XL 30) was used in order to image three different solution samples, i.e. pure gold nanoparticle conjugate, pure amyloid protein (not conjugated to nanoparticles) and mixture of gold nanoparticle conjugates and amyloid protein. For each sample small droplets (20 μl) of these solutions were put on a clean silicon (100 orientation) surface. Samples thus prepared were then analyzed by SEM before and after laser irradiation in order to

evaluate any change in surface topography. Therefore, low beam voltage (5 keV) capabilities of SEM were used over the gold nano-coating to avoid charging effects. In some cases, where higher magnification images were required, the samples were gold coated. High resolution images of different magnification (200-27,000x) were acquired digitally and are presented without further modification.

AFM measurements. All sample measurement was carried out in air using the Close-Contact Mode of Nano-R2™ AFM equipped with a light lever scanner. The Close-Contact Mode was found the most suitable for these samples. Regular Close-Contact probes with a normalized radius of < 10 nm were used in all data acquisition. The Nano-R2™ system was calibrated in the X, Y, and Z axes before measurement. We utilized the standard samples to calibrate Z-height channel, and resulting system accuracy was ± 1 %. The resonant frequency of used probes was tested to comply with manufacturers' data sheet. We minimized the drive amplitudes to enhance the measurement stability in the Close-Contact Mode. Raw scanning data were processed using the NanoRule+ software. Different scanning rate, resolution and angle were used to achieve optimal results.

7.4 Chapter 4 experimental- Antibody-gold quantum dot-PAMAM dendrimer complex as an immunoglobulin immunoassay

Synthesis and conjugation of gold QDs. Gold QDs with an emission maximum at 450 nm (λ_{exc} = 387 nm) were synthesized according to a method previously reported in the literature[14,15]: in brief 0.5 μmol PAMAM G2-OH (Sigma-Aldrich, St. Louis, MO) and 1.5 μmol $HAuCl_4 \cdot nH_2O$ (Sigma-Aldrich) were co-dissolved in 2 mL of distilled

water (resistivity 18 MΩ·cm and surface tension of 72.6 mN/m at 20.0˚C, Continental Modulab 2020). The gold ions were sequestered within the dendrimer prior to the slow addition of an equivalent of the reductant $NaBH_4$ by allowing 30 min of stirring (Sigma-Aldrich). The solution was stirred for 2 days so that reaction and aggregation processes could complete. Purification of the resulting solution was performed through ultracentrifugation at 16000 g for 45 min (Beckman L7 Ultracentrifuge, Fullerton, CA) resulting in separation of the larger Au nanoparticles from the smaller AuQDs, leaving a clear solution of AuQDs. Then, the AuQDs were suspended in 2 mL phosphate buffer saline solution (PBS, pH 6.3) and mixed with 1 mg of polyclonal antibody to human IgG (goat affinity purified antibody to human IgG; MP Biomedicals, Irvine, CA). The antibody-dendrimer-AuQD complex was electrostatically conjugated at the above mentioned pH. The solution was then vortexed for 12 h. All of the work involving immunocomplexation of the antibody-QD complex with the recombinant human IgG antigen was performed in the presence of PBS buffer at a pH of 6.3. It was previously reported[15], as stated above, that AuQDs of varying sizes, and thus emission maxima, are able to be synthesized using this method. However, we were unable to reproduce this finding: only AuQDs with emission at 450 nm were able to be synthesized.

Nanoscale imaging of particles, antibody-particle conjugates, and antigen-conjugate complex. For the purpose of visualizing the structure and topography of the gold nanoparticles, Au nanoparticle- anti-human IgG polyclonal antibody conjugates, and immunocomplex formed after addition of recombinant human IgG antigen, high-resolution transmission electron microscopy (HR-TEM) was utilized. All of the high-resolution TEM imaging was performed on the Philips CM 20 TEM with LaB6 electron

gun and EDS (EDAX/4pi) system. The system has an accelerating voltage of 200 keV with an image point resolution of 0.278 nm, line resolution of 0.14 nm and maximum magnification of 750,000 X in the high-resolution mode. Diluted samples were drop-coated on the surface of lacey carbon grids, allowed to dry and then introduced into the vacuum chamber.

For the purpose of topographic characterization atomic force microscopy (AFM) measurements were conducted on the Dimension 5000 AFM microscope (Veeco Instruments Inc, Santa Barbara, CA), in tapping mode. Imaging was performed with a sharp silicon cantilever and under a moderately-slow scan, with a scanning frequency of 1.508 Hz.

Photoluminescence characterization was performed on a Fluorolog-3 spectrofluorometer (Horiba Jobin Yvon, Edison, NJ). Absorption measurements were performed on a Lambda 900 UV/Vis/NIR spectrometer (Perkin Elmer, Waltham, Massachusetts). Sample cells used for both measurements were composed of quartz and had an optical pathlength of 1 cm.

7.5 Chapter 5 experimental- Protein and enzyme stabilized quantum dots

The synthesis of the OPAA-QD conjugate is the following. Cadmium nitrate, Na_2S, NaOH were purchased from Sigma Aldrich (Milwaukee, Wisconsin) at the highest purity available. The water used was purified with a Modulab 2020 water purification system from Continental Water Systems Corp (San Antonio, TX). The purified water had a specific resistance of 18 MΩ·cm and surface tension of 72.6 mN m^{-1} at 20 ± 1 °C.

Purified OPAA (EC 3.1.8.2, purity of 85-90 %, MW 58.5 kDa) was obtained from the U.S. Army Laboratory at Edgewood Chemical and Biological Center, APG, MD. The OPAA-CdS QDs were synthesized by first preparing a solution containing 0.43 mg/mL of OPAA and Cd^{2+} in Ar-flushed purified water. The pH of the solution was adjusted to 8.5 with concentrated NaOH. Then, S^{2-} was introduced into the solution with rapid stirring. The final concentration of Cd^{2+} and S^{2-} ions was $1x10^{-3}$ M each. Finally, the solution was continuously mixed for 1 h. The solution was purified by Sephadex G75 column.

Purification of OPAA-CdS QDs by Sephadex G75 column. The OPAA-CdS QDs and excess OPAA were eluted by the Borex/HCl (pH 8.5) buffer through a 2.22 x 22.25 cm (Diameter x Height) Sephadex G75 column. Each 3 mL fraction was collected and measured by UV-Vis spectroscopy. From 9-13 fractions, the absorption of OPAA-CdS can be clearly observed at 410 and 278 nm. In the 27-34 fractions, the OPAA absorption band was observed at 278 nm.

Chapter 8. References

1. MacRitchie, F. *Chemistry at Interfaces*, Academic Press, Inc, San Diego, **1990**.

Gaines, G. L. Jr. *Insoluble Monolayers at Liquid-Gas Interfaces*; Wiley-Interscience, New York, **1966**.

2. Schwartz, D. K., *Surf. Sci. Rep.* **1997**, *27*, 241.

3. Henon, S.; Meunier, J. *Rev. Sci. Instrum.* **1991**, *62*, 936.

4. Blodgett, K.B. *J. Am. Chem. Soc.* **1935**, *57*, 1007.

5. Blodgett, K.B.; Langmuir, I. *Phys. Rev.* **1937**, *51*, 964.

7. Merrifield, R.B. *J. Am. Chem. Soc.* **1963** 85, 2149.

8. Chang, C.-D.; Meienhofer, J. *Int. J. Peptide Protein Res.* **1978** 11, 246.

9. Atherton, E.; Fox, H.; Harkiss, D.; Shappard, R.C. *J. Chem. Soc. Chem. Commun.* **1978** 537.

10. Atherton, E.; Fox, H.; Harkiss, D.; Sheppard, R.C. *J. Chem. Soc. Chem. Commun.* **1978** 539.

11. Selkoe, D. J. *Nature* **1999**, 399, A23.

12. Terry, R. D. *Prog. Brain Res.* **1994**, 101, 383.

13. Selkoe, D. J. *Trends Cell Biol.* **1998**, 8, 447.

14. Masters, C. L.; Simms, G.; Weinman, N. A.; Multhaup, G.; Mcdonald, B. L.; Beyreuther, K. *Proc. Natl. Acad. Sci. U.S.A.* **1985**, 82, 4245.

15. Noda-Saita, K.; Yoneyama, A.; Shitaka, Y.; Hirai, Y.; Terai, K.; Wu, J.; Takeda, T.; Hyodo, K.; Osakabe, N.; Yamaguchi, T.; Okada, M. *Neuroscience*. **2006**, 138, 1205.

16. Iverson, L. L.; Mortishire-Smith, R. J.; Pollack, S. J.; Shearman, M. S. *Biochem. J.* **1995**, 311, 1.

17. Bateman, R.J.; Munsell L.Y.; Morris, J.C.; Swarm, R.; Yarasheski, K.E.; Holtzman, D. M. *Nat. Med.* **2006**, 12, 856.

18. Haglund, M.; Kalaria, R.; Slade, J. Y.; Englund, E. *Acta Neuropathol.* **2006**, 111, 430.

19. Benzinger, T. L. S.; Gregory, D. M.; Burkoth, T. S.; Miller-Auer, H.; Lynn, D. G.; Botto, R. E.; Meredith, S. C. *Biochemistry* **2000**, 39, 3491.

20. Terzi, E.; Hölzemann, G.; Seelig, J. *Biochemistry* **1994**, 33, 1345.

21. Cheng, G.; Whitehead, S. N.; Hachinski, V.; Cechetto, D. *Neurobiol. Dis.* **2006**, 23, 140.

22. Pike, C. J.; Burdick, D.; Walencewicz, A. J.; Glabe, C. G.; Cotman, C. W. *J. Neurosci.* **1993**, 13, 1676.

23. Li, C.; Orbulescu, J.; Sui, G.; Leblanc, R. M. *Langmuir* **2004**, 20*,* 8641.

24. Hiramatsu, H.; Kitagawa, T. *Biochim. Biophys. Acta* **2005**, 1753, 100.

25. Martin, A. H.; Meinders, M. B. J.; Bos, M. A.; Cohen Stuart, M. A.; van Vliet, T. In *Food Colloids, Biopolymers & Materials*; Dickinson, E., van Vliet, T., Eds.; Royal Society of Chemistry: Cambridge, **2003**.

26. Walton, A. G.; Blackwell, J. *Biopolymers*; Chap. 6. Academic Press Inc.: New York, **1973**.

27. Fasman, G. D.; Potter, H. *Biochem. Biophys. Res. Commun*. **1967**, 27, 209.

28. Rippon, W. B.; Chen, H. H.; Walton, A. G. *J. Mol. Biol.* **1973**, 75, 369.

29. Goodman, M.; Toniolo, C.; Naider, F. In *Peptides, Polypeptides and Proteins*; Blout, E. R., Bovey, F. A., Goodman, M., Lotan, N., Eds.; Wiley: New York, **1974**.

30. Goodman, M.; Verdini, A. S.; Toniolo, C.; Phillips, W. D.; Bovey, F. A. *Proc. Natl. Acad. Sci. U.S.A.* **1969**, 64, 444.

31. Takano, K.; Endo, S.; Mukaiyama, A.; Chon, H.; Matsumura, H.; Koga, Y.; Kanaya, S. *FEBS J.* **2006**, 273, 150.

32. Noda-Saita, K.; Yoneyama, A.; Shitaka, Y.; Hirai, Y.; Terai, K.; Wu, J.; Takeda, T.; Hyodo, K.; Osakabe, N.; Yamaguchi, T.; Okada, M. *Neuroscience* **2006**, 138, 1205.

33. Selkoe, D.J. *Nature* **1999**, 399, A23.

34. Iverson, L.; Mortishire-Smith, R. J.; Pollack, S. J.; Shearman, M. S. *Biochem. J*. **1995**, 311, 1.

35. Bateman, R. J.; Munsell, L. Y.; Morris, J. C.; Swarm, R.; Yarasheski. K. E.; Holtzman, D. M. *Nat. Med.* 2006, 12, 856.

36. Haglund, M.; Kalaria, R.; Slade, J. Y.; Englund, E. *Acta Neuropathol.* **2006**, 111, 430.

37. Benzinger, T. L. S.; Gregory, D. M.; Burkoth, T. S.; Miller-Auer, H.; Lynn, D. G.; Botto, R. E.; Meredith, S. C. *Biochemistry* **2000,** 39, 3491.

38. Estrada, L. D. ; Soto, C. *Curr. Pharm. Des.* **2006**, 12, 2557.

39. Soto, C.; Estrada, L. D. *Subcell. Biochem*. **2005**, 38, 351.

40. Bieln, S. ; Soto, C. *Curr. Drug Targ*. **2004**, 5, 553.

41. Adessi, C.; Frossard, M.; Banks, W. A.; Soto, C. *J. Biol. Chem*. **2003**, 278, 13905.

42. Adessi, C.; Soto, C. *Drug Develop. Res*. **2002**, 56, 184.

43. Thanh, N. T. K.; Rosenzweig, Z. *Anal. Chem*. **2002**, 74, 1624.

44. Kerker, M. (Ed.), *The Scattering of Light and Other Electromagnetic Radiation*, Academic, New York, **1969**.

45. Bohren, C. F.; Huffman, D. R. (Eds.), *Absorption and Scattering of Light by Small Particles*, Wiley, New York, **1983**.

46. Kreibig, U.; Vollmer, M. (Eds.), *Optical Properties of Metal Clusters*, Springer, Berlin, **1995**.

47. Faulhaber, A. E.; Smith, B. A.; Andersen, J. K.; Zhang, J. Z. *Mol. Cryst. Liq. Cryst. Sci. Technol*. **1996**, Sect. A 283, 25.

48. Ahmadi, T. S.; Logunov, S. L.; El-Sayed, M. A.; Khoury, J. T.; Whetten, R. L. *J. Phys. Chem B* **1997**, 101, 3713.

49. Perner, M.; Bost, P.; Plessen, G. V.; Feldmann, J.; Becker, U.; Mennig, M.; and Schmidt, H. *Phys. Rev. Lett*. **1997**, 78, 2192.

50. Ahmadi, T. S.; Logunov, S. L.; El-Sayed, M. A. *J. Phys. Chem*. **1996**, 100, 8053.

51. Hodak, J. K.; Martini, I.; Hartland, G. V. *Chem. Phys. Lett*. **1998**, 284, 135.

52. Serafetinides, A. A.; Skordoulis, C. D.; Makropoulou, M. I.; Kar, A. K. *Appl. Surf. Sci*. **1998**, 135, 276.

53. Rogachefsky, A. S.; Silapunt, S.; Goldberg, D. J. *Dermatol. Surg*. **2002,** 28, 410.

54. Hirsch, L. R.; Stafford, R. J.; Bankson, J. A.; Sershen, S. R.; Rivera, B.; Price, R. E.; Hazle, J. D.; Halas, N. J.; West, J. L. *Proc. Nat. Acad. Sci*. **2003**, 10, 13549.

55. O'Neal, D. P.; Hirsch, L. R.; Halas, N. J.; Payne, J. D.; West, J. L. *Cancer Lett*. **2004** 209, 171.

56. El-Sayed, I. H.; Huang, X.; El-Sayed, M. A. *Cancer Lett*. **2006**, 239, 129.

57. Pomerai, D. I.; Smith, B.; Dawe, A.; North, K.; Smith, T.; Archer, D. B.; Duce, I. R.; Jones, D.; Candido, E. P. M. *FEBS Lett*. **2003,** 543, 93.

58. Bastus, N. G.; Kogan, M. J.; Amigo, R.; Grillo-Bosch, D.; Araya, E.; Turiel, A.; Labarta, A.; Giralt, E.; Puntes, V. F. *Mat. Sci. Eng. C*. doi:10.1016/j.msec.**2006**.08.003.

59. Kogan, M. J.; Bastus, N. G.; Amigo, R.; Grillo-Bosch, D.; Araya, E.; Turiel, A.; Labarta, A.; Giralt, E.; Puntes, V. F. *Nano Lett*. **2006**, 6, 110.

60. Worden, J. G.; Shaffer, A. W.; Huo, Q. *Chem Comm*. **2004**, 5, 518.

61. Worden, J. G.; Dai, Q.; Shaffer, A. W.; Huo, Q. *Chem. Mater*. **2004**, 16, 3746.

62. Liu, X.; Worden, J. G.; Dai, Q.; Zou, J.; Wang, J.; Huo, Q. *Small* **2006**, 2, 1126.

63. Worden, J. G.; Dai, Q.; Huo, Q. *Chem. Comm*. **2006**, 14, 1536.

64. Dai, Q.; Worden, J. G.; Trullinger, J.; Huo, Q. *J. Am. Chem. Soc*. **2005**, 127, 8008.

65. Zheng, M. ; Li, Z. ; Huang, X. *Langmuir* **2004**, 20, 4226.

66. Link, S.; Burda, C.; Mohamed, M. B.; Nikoobakht, B. El-Sayed, M. A. *J. Phys. Chem*. **1999**, A, 103, 1165.

67. Gao, X.; Yezhelyev, M.; Xing, Y.; O'Regan, R. M.; Nie, S. *Immuno. Bioanal. Tech*. **2007**, 465.

68. Byers, R.J.; Di Vizio, D.; O'Connell, F.; Tholouli, E.; Levenson, R.M.; Gossard, K.; Twomey, D.; Yang, Y.; Benedettini, E.; Rose, J.; Ligon, K.L.; Finn, S.P.; Golub, T.R.; Loda, M. *J. Mol. Diagn*. **2007**, 9, 20.

69. Eastman, P.S.; Ruan, W.; Doctolero, M.; Nuttall, R.; de Feo, G.; Park, J.S.; Chu, J.S.F.; Cooke, P.; Gray, J.W.; Li, S.; Chen, F.F. *Nano Lett*. **2006**, 6, 1059.

70. Han, M.; Gao, X.; Su, J.Z.; Nie, S. *Nat. Biotechnol*. **2001**, 19, 631.

71. Chan, W.C.W.; Maxwell, D. J.; Gao, X.; Bailey, R.E.; Han, M.; Nie, S. *Curr. Opin. Biotechnol*. **2002**, 13, 40.

72. Klostranec, J.M.; Chan, W.C.W. *Adv. Mat*. **2006**, 18, 1953.

73. Jain, K.K. *Clin. Chim. Acta*. **2005**, 358, 37.

74. Fortina, P.; Kricka, L.J.; Surrey, S.; Grodzinski, P. *Trends Biotechnol*. **2005**, 23, 168.

75. Jain, K.K. *Expert Rev. Mol. Diagn.* **2003**, 3, 153.

76. Michalet, X.; Pinaud, F.F.; Bentolila, L.A.; Tsay, J.M.; Doose, S.; Li, J.J.; Sundaresan, G.; Wu, A.M.; Gambhir, S.S.; Weiss, S. *Science*, **2005**, 307, 538.

77. Hahn, M.A.; Tabb, J.S.; Krauss, T.D. *Anal. Chem.* **2005**, 77, 4861.

78. Kuno, M.; Fromm, D.P.; Hamann, H.F.; Gallagher, A.; Nesbitt, D.J. *J. Chem. Phys.* **2001**, 115, 1028.

79. Seydack, M. *Biosens. Bioelectron.* **2005**, 20, 2454.

80. Zheng, J.; Petty, J.T.; Dickson, R.M. *J. Am. Chem. Soc.* **2003**, 125, 7780.

81. Zheng, J.; Zhang, C.; Dickson, R.M. *Phys. Rev. Lett.* **2004**, 93, 077402/1.

82. Thanh, N. T. K.; Rosenzweig, Z. *Anal. Chem.* **2002**, 74, 1624.

83. Tan, W.B.; Zhang, Y. *J. Biomed. Mat. Res*. **2005**, 75, 56.

84. Chaki, N.K.; Kakade, B.; Sharma, J.; Mahima, S.; Vijayamohanan, K.P.; Haram, S.K. *J. App. Phys*. **2004**, 96, 5032.

85. Triulzi, R.C.; Micic, M.; Giordani, S.; Serry, M.; Chiou, W.; Leblanc, R.M. *Chem.Comm*. **2006**, 48, 5068.

86. Choi, Y.; Thomas, T.; Kotlyar, A.; Islam, M.T.; Baker, J.R., Jr. *Chem. Biol*. **2005**, 12, 35.

87. Choi, Y.; Mecke, A.; Orr, B.G.; Holl, M.M.B.; Baker, J.R., Jr. *Nano Lett*. **2004**, 4, 391.

88. Kang, H.; DeLong, R.; Fisher, M.H.; Juliano, R.L. *Pharm. Res*. **2005**, 22, 2099.

89. Tsvetkov, D. E.; Cheshev, P. E.; Tuzikov, A. B.; Chinarev, A. A.; Pazynina, G. V.; Sablina, M. A.; Gambaryan, A. S.; Bovin, N. V.; Rieben, R.; Shashkov, A. S.; Nifant'ev, N. E. *Russ. J. Bioorg. Chem*. **2002**, 28, 470.

90. Wang, X.; Inapagolla, R.; Kannan, S.; Lieh-Lai, M.; Kannan, R.M. *Bioconj. Chem*. **2007**, 18, 791.

91. Lee, S. C.; Parthasarathy, R.; Botwin, K.; Kunneman, D.; Rowold, E.; Lange, G.; Klover, J.; Abegg, A.; Zobel, J.; Beck, T.; Miller, T.; Hood, W.; Monahan, J.; McKearn, J. P.; Jansson, R.; Voliva, C. F. *Biomed. Microdev*. **2004**, 6, 191.

92. Kim, J.; Choi, J.S.; Nam, K.; Lee, M.; Park, J.; Lee, J. *J. Control. Rel.* **2006**, 114, 110.

93. Wisher, A.C.; Bronstein, I.; Chechik, V. *Chem. Comm.* **2006**, 15, 1637-1639.

94. Yoo, H.; Sazani, P.; Juliano, R.L. *Pharm. Res.* **1999**, 16, 1799.

95. Khandare, J.; Kolhe, P.; Pillai, O.; Kannan, S.; Lieh-Lai, M.; Kannan, R.M. *Bioconjugate Chem.* **2005**, 16, 330.

96. Chauhan, A.S.; Jain, N.K.; Diwan, P.V.; Khopade, A.J. *J. Drug Targeting*. **2004**, 12, 575.

97. Wang, D.; Imae, I. *J. Am. Chem. Soc.* **2004**, 126, 13204.

98. Crooks, R.M.; Zhao, M.; Sun, L.; Chechik, V.; Yeung, L.K. *Acc. Chem. Res.* **2001**, 34, 181.

99.Esumi, K.; Suzuki, A.; Aihara, N.; Usui, K.; Torigoe, K. *Langmuir* **1998**, 14, 3157.

100. Zheng, J.; Dickson, R.M. *J. Am. Chem. Soc.* **2002**, 124, 13982.

101. Niemeyer, C. M. *Angew. Chem. Int. Ed.* **2001**, 40, 4128; Niemeyer, C. M. *Angew. Chem. Int. Ed.* **2003**, 42, 5796.

102. Chan, W. C. W.; Nie, S. *Science* **1998**, 281, 2016.

103. Storhoff, J. J.; Mirkin, C. A. *Chem. Rev.* **1999**, 99, 1849; Whaley, S. R.; English, D. S.; Hu, E. L.; Barbara, P. F.; Belcher, A. M. *Nature* **2000**, 405, 665; Meziani, M. J. Sun, Y. P. *J. Am. Chem. Soc*. **2003**, 125, 8015.

104. Niesz, K.; Grass, M.; Somorjai, G. A. *Nano. Lett.* **2005**, 5, 2238.

105. Mamedova, N. N.; Kusterbeck, A. W.; Rogach, A. *Nano Lett*. **2001**, 1, 281.

106. Meziani, M. J.; Pathak, P.; Harruff, B. A.; Hurezeanu, R.; Sun, Y. P. *Langmuir* **2005** , 21, 2008.

107. Cheng, T. C.; DeFrank, J. J.; Rastogi, V. P. *Chem. Biol. Int.*, **1999**, 119, 455.

108. Kim, J.; Grate, J. W. *Nano Lett.* **2003**, 3, 1219.

109. Simonian, A. L.; diSioudi, B. D.; Wild, J. R. *Anal. Chim. Acta*, **1999**, 388, 189.

110.Vossmeyer, T.; Katsikas, L.; Giersig, M.; Popovic, I. G.; Diesner, K.; Chemseddine, A.; Eychmüller, A.; Weller, H. *J. Phys. Chem.*, **1994**, 98, 7665.

VITA

Robert C. Triulzi Jr. was born in San Juan, Puerto Rico on October 20th, 1981 to Robert C. Triulzi and Peggy S. Triulzi. He received his elementary education at Brewster Elementary school, Rochester Hills, MI, Frankfurt International School, Frankfurt, Germany, and the American School of Madrid, Madrid, Spain. His secondary education was completed at St. Thomas Aquinas high school in Fort Lauderdale, Florida. He entered the University of Miami College of Arts and Sciences in the fall of 2000. This is where he completed the work for a B.S. in chemistry and a B.S. in biology with a minor in mathematics. In August 2004 he was admitted to the graduate program in chemistry at the University of Miami. He has published the following papers as a result of research conducted at the University of Miami:

Robert C. Triulzi**,** Miodrag Micic, Silvia Giordani, Michael Serry, Wen-An Chiou and Roger M. Leblanc "Immunoassay Based on the Antibody-Conjugated PAMAM-Dendrimer-Gold Quantum Dot Complex" Chemical Communications, 2006, 48, 5068-5070.

Robert C. Triulzi, Changqing Li, David Naistat, Jhony Orbulescu, and Roger M. Leblanc "A Two Dimensional Approach to Study Amyloid β-Peptide Fragment (25-35)" Journal of Physical Chemistry C, 2007, 111(12), 4661-4666.

Robert C. Triulzi, Jhony Orbulescu, Qiu Dai, Allen Gu, Qun Huo, and Roger M. Leblanc "Photothermal Ablation of Amyloid Aggregates by Gold Nanoparticles" Colloids and Surfaces B (COLSUB) COLSUB-D-07-00442 (Accepted 12/07, In press), doi:10.1016/j.colsurfb.2007.12.006

Robert C. Triulzi**,** Miodrag Micic, Jhony Orbulescu, Silvia Giordani, Bill Mueller and Roger M. Leblanc "Antibody-Gold Quantum Dot-PAMAM Dendrimer Complex as an Immunoglobulin Immunoassay" The Analyst manuscript ID B718730K (Accepted 2/08, In press DOI: 10.1039/b718730k).

Liang Zhao, Robert C. Triulzi, Kerim M. Gattás-Asfura, Jianmin Xu, Jinhai Wang, Qun Huo, Vipin K. Rastogi, Saumil S. Shah, Joseph J. DeFrank and Roger M. Leblanc **"**Direct Conjugation of Organophosphorus Acid Anhydrolase with CdS Quantum Dots for Detection of Diisopropylfluorophosphate" Submitted Angewandte Chemie Int. Ed. (4/08).

Research highlighted in Biophotonics International, January 2007, p.24.